

# Double pion photoproduction off the proton at threshold and in the second resonance region

PhD Thesis

Fabien Zehr

Universität Basel  
February 2008



# Abstract

The nucleon, as we know it today, is a complex system made of three valence quarks, gluons and quark-antiquark pairs from the sea. This picture has been firmly established in the framework of deep inelastic scattering. At lower energies, where the perturbative expansion is not valid any more, the behavior of the nucleon and its resonances is however a much more complex issue. An exact treatment of the problem is today out of reach and the main part of our current theoretical knowledge on the resonances is based on constituent quark models which subsume the complex internal structure of the nucleon in three massive constituent quarks. The discrepancies between the predictions of such models and the experimental resonance spectrum, such as the problem of missing resonances (the number of resonances predicted by the models is higher than what is actually observed) or the mass of the lowest lying resonance -the  $P_{11}(1440)$  or Roper resonance- which most models overestimate, calls for a more detailed investigation of this field.

On the experimental side, meson photoproduction off nucleons is the ideal complement to pion induced reactions which have been studied for more than 40 years and forms our main source of knowledge on nucleon resonances. The reaction studied in this work, double pion photoproduction  $\gamma N \rightarrow \pi\pi N$ , is especially worthwhile since it gives access to decay properties that can't be observed with single meson photoproduction: the sequential decay of the resonance via an intermediate  $\Delta$  resonance  $\gamma p \rightarrow N^* \rightarrow \Delta\pi \rightarrow N\pi\pi$  or the decay via emission of  $\rho$  or  $\sigma$  mesons which decay in two pions.

In this work, we measured the  $\gamma p \rightarrow p\pi^0\pi^0$  and  $\gamma p \rightarrow n\pi^+\pi^0$  reactions with a special emphasis on the energies close to threshold and on recently available polarization observables. The experiment was performed at MAMI in Mainz in the years 2004 and 2005 using a beam of linearly and circularly polarized tagged photons produced by bremsstrahlung of electrons on a thin diamond radiator with a maximal energy of 820 MeV. The reaction happened in a liquid hydrogen target. The decay particles were detected by the Crystal Ball detector in conjunction with the TAPS detector as forward wall, covering almost 100% of the total  $4\pi$  solid angle and thus ensuring a very high detecting efficiency.

This state-of-the art facility allowed the determination of total cross sections for

the double  $\pi^0$  and  $\pi^0 \pi^+$  channels with a very good precision. Especially interesting is the  $\gamma p \rightarrow p \pi^0 \pi^0$  cross section close to threshold since it provides a stringent test for chiral perturbation theory. The calculation of ChPT, which predicts a dominant contribution of pion loops, are very well reproduced by our data.

In addition, Dalitz plots and invariant mass distributions have also been produced. Their good precision confirms the important features of the double pion mechanisms such as the dominance of the  $D_{13}(1520)$  sequential decay, the small contribution of the  $P_{11}(1440) \rightarrow p(\pi^0 \pi^0)_{S\text{-wave}}^{I=0}$  decay, and for the  $n \pi^0 \pi^+$  channel, the crucial role of the  $D_{13}(1520) \rightarrow \rho n \rightarrow \pi^0 \pi^+ n$ .

Finally, polarization observables have been measured. Circular asymmetries have been precisely determined for all three isospin channels (with [Kra07]). Being very sensitive to small changes in the models, they represent a unique tool to precisely disentangle the contribution of the resonances in the second resonance region. At this time however, the important discrepancy between our results and the theoretical predictions doesn't allow such an extraction without further refinement in the theoretical models.

# Contents

<b>1</b>	<b>Introduction</b>	<b>1</b>
1.1	The structure of matter, 2500 years of interrogations . . . . .	1
1.2	Nucleon resonances . . . . .	10
<b>2</b>	<b>Theoretical models</b>	<b>15</b>
2.1	Studying resonances with meson photoproduction . . . . .	15
2.2	The double pion channel . . . . .	18
2.3	Theoretical models for the double pion photoproduction . . . . .	23
2.3.1	Saclay model . . . . .	23
2.3.2	Valencia model . . . . .	25
2.3.3	Mainz model . . . . .	25
2.3.4	Hiroshima model . . . . .	28
2.4	Bonn-Gatchina partial wave analysis . . . . .	29
2.5	Polarization observables . . . . .	29
2.5.1	Asymmetries . . . . .	31
2.6	Double pion photoproduction at threshold . . . . .	35
2.7	Some words on the magnetic moment of the $\Delta^+(1232)$ resonance	36
<b>3</b>	<b>Experimental setup</b>	<b>39</b>
3.1	MAMI, the electron accelerator . . . . .	39
3.2	Polarized photon production . . . . .	41
3.2.1	Linearly polarized photons . . . . .	42
3.2.2	Circularly polarized photons . . . . .	46
3.2.3	Collimation . . . . .	46
3.3	The tagger . . . . .	47
3.4	Liquid hydrogen target . . . . .	49
3.5	Detectors . . . . .	50
3.5.1	The Crystal Ball . . . . .	50
3.5.2	TAPS . . . . .	54
3.6	Electronics . . . . .	57
3.6.1	Crystal Ball electronics . . . . .	57

3.6.2	TAPS electronics . . . . .	58
3.6.3	Trigger . . . . .	59
3.7	Data taking . . . . .	61
<b>4</b>	<b>Data processing</b>	<b>63</b>
4.1	AcquRoot analysis framework . . . . .	63
4.2	Time calibration . . . . .	65
4.2.1	Tagger time calibration . . . . .	65
4.2.2	TAPS time calibration . . . . .	66
4.2.3	Crystal ball time calibration . . . . .	68
4.3	Energy calibration . . . . .	69
4.3.1	Tagger energy calibration . . . . .	69
4.3.2	TAPS energy calibration . . . . .	69
4.3.3	Crystal ball energy calibration . . . . .	70
4.4	Particle identification . . . . .	71
4.4.1	Clusterization . . . . .	71
4.4.2	TAPS particle identification . . . . .	73
4.4.3	Crystal ball particle identification . . . . .	76
4.5	Random subtraction . . . . .	79
4.6	Tagging efficiency . . . . .	80
4.7	Credits . . . . .	83
<b>5</b>	<b>Simulations</b>	<b>85</b>
5.1	Detector simulation . . . . .	85
5.2	Event generation . . . . .	86
5.3	Efficiency determination . . . . .	87
5.3.1	$\gamma p \rightarrow p\pi^0\pi^0$ efficiency . . . . .	88
5.3.2	$\gamma p \rightarrow n\pi^+\pi^0$ efficiency . . . . .	89
<b>6</b>	<b>Data analysis</b>	<b>91</b>
6.1	Cross sections . . . . .	91
6.1.1	Identification of double $\pi^0$ events . . . . .	92
6.1.2	$\gamma p \rightarrow p\pi^0\pi^0$ Cross Section . . . . .	93
6.1.3	Identification of $\pi^0 \pi^+$ events . . . . .	95
6.1.4	$\gamma p \rightarrow n\pi^+\pi^0$ cross section . . . . .	97
6.2	Asymmetry . . . . .	97
6.2.1	Circular asymmetry . . . . .	100
6.2.2	Linear asymmetry . . . . .	101
6.3	Dalitz plots . . . . .	102
6.3.1	$\gamma p \rightarrow p\pi^0\pi^0$ Dalitz plots . . . . .	104
6.3.2	$\gamma p \rightarrow n\pi^+\pi^0$ Dalitz plots . . . . .	105

<b>7</b>	<b>Results</b>	<b>109</b>
7.1	$\gamma p \rightarrow p\pi^0\pi^0$ cross section . . . . .	109
7.1.1	$\gamma p \rightarrow p\pi^0\pi^0$ Cross section at threshold . . . . .	111
7.2	$\gamma p \rightarrow n\pi^+\pi^0$ cross section . . . . .	112
7.2.1	$\gamma p \rightarrow n\pi^+\pi^0$ cross section at threshold . . . . .	114
7.3	Circular asymmetries . . . . .	115
7.4	Linear asymmetries . . . . .	118
7.5	Dalitz plots and invariant masses distributions . . . . .	119
7.5.1	$\gamma p \rightarrow p\pi^0\pi^0$ invariant masses . . . . .	119
7.5.2	$\gamma p \rightarrow n\pi^+\pi^0$ invariant masses . . . . .	121
7.5.3	Invariant masses close to threshold . . . . .	123
<b>8</b>	<b>Conclusion and outlook</b>	<b>127</b>
<b>9</b>	<b>Acknowledgments</b>	<b>131</b>
<b>A</b>	<b>Specific problems in the analysis</b>	<b>133</b>
A.1	Tagger 4x4 structure . . . . .	133
A.2	Ice deposition on the target window . . . . .	135
<b>B</b>	<b>Tables</b>	<b>139</b>

# 1 Introduction

*The title of this thesis, 'Double pion photoproduction off the proton at threshold and in the second resonance region', might seem a little gibberish for the reader who's not familiar with meson photoproduction. The goal of this first chapter is to put our research in some context by giving background information on the physics we're working with. We will first give an historical glimpse of the long physicist's quest towards an understanding of the nature of matter. This overview has been voluntarily kept on a basic level and no equation has been used for a better emphasis on the important milestones in the timeline of important discoveries. The reader who is already familiar with this subject might directly switch to the second section of this chapter in which our contribution to the understanding of matter -the study of nucleon resonances- is explicated.*

## 1.1 The structure of matter, 2500 years of interrogations

### Early concepts

Understanding the fundamental structure of matter has since a very long time been a major concern for humanity. The first interrogations on this subject appeared more than 2500 years ago in ancient Greece. At this time, in the absence of experimental testing grounds, the nature of matter was more closely related to philosophy than to physics. The mainstream concept was formulated by Empedocles in the 5<sup>th</sup> century b.c. and is usually referred to as the Aristotelian description of nature. In this point of view, the nature consists of four basis elements - water, earth, wind, fire - and every being, every natural phenomenon consists of a combination of those four basis elements. This theory, sometimes completed with a fifth element (the ether, which fills the empty regions beyond the sky) remained the dominant dogma through the antiquity, the middle ages and the renaissance<sup>1</sup>. Over the centuries, it strongly influenced our views about

---

<sup>1</sup>Similar concepts were also developed early in Asian philosophy. The Wu Xing concept in ancient China described for example the nature with 5 elements: metal, wood, water, fire, and

the nature. The last famous example persisted as long as until the second half of the 19<sup>th</sup> century. At this time, the existence of the 'luminiferous aether' -the fluid into which the light waves propagate- postulated by I. Newton in 1704 was ruled out by the famous Michelson-Morley experiment. In the meanwhile, an alternative description of nature was thought of by Leucippus and Democritus. It described the nature as made of tiny, variously shaped, unbreakable elements called *atoms*. This philosophical concept, although much less developed and at this time accepted by very few people, is the closest to the scientific reality as we know it today.

### The atom

Twenty centuries later, the new philosophical concepts of rationalism and empiricism developed among others by R. Descartes and I. Kant brought discussions on the nature of matter into the field of science. As already stated much earlier by R. Bacon, each theory had to be verified with dedicated experiments to be acceptable. In 1803, J. Dalton, triggered by the pioneering chemical work of A. Lavoisier and the least known modern atomic theory by R. Boscovitch in 1763, formulated the first scientific atomic theory in his 'law of multiple proportions'. In this theory, each chemical element is made of tiny, unbreakable, identical particles, each element has its own kind of atom and atoms of two elements can combine to form compound elements. He deduced again that the mass of each atom is a multiple of the mass of the lightest atom, the hydrogen atom. In 1811, the main flaws in this theory were corrected by A. Avogadro, in particular by making the distinction between atoms and molecules. This theory forms a firm basis for the classification of the elements as we know it today. At this time however, the use of atoms was considered by many to be an artifact and last doubts about the existence of atoms were lifted in 1896 only with the discovery of radioactivity by H. Becquerel.

### The Bohr model of the atom

In the second half of the 19<sup>th</sup> century, some phenomena such as the existence of regular patterns in D. Mendeleev periodical table of elements (1869) or the regular spacing in the hydrogen light spectrum observed by J. J. Balmer in 1885 were difficult to conciliate with the hypothesis of a point-like, elementary atom. The discovery of the electron by J. J. Thompson in 1897 definitely ruled out atoms as the ultimate *atoms*<sup>2</sup>. In 1909, the famous Rutherford experiment, in which the number of  $\alpha$  particles reflected backwards when directed to a thin golden foil was much larger than expected, was used to show that most of the mass of the atom

---

earth

<sup>2</sup>From greek *ατομος*, meaning *unsecable*.

## 1.1. THE STRUCTURE OF MATTER, 2500 YEARS OF INTERROGATIONS<sup>3</sup>

is concentrated in its center in a so-called atomic nucleus made of elementary, positively charged particles, the protons.

These two discoveries led to the atomic model formulated by N. Bohr in 1913. In this model, the atom is made of a tiny, positive nucleus, made of protons around which electrons are orbiting. These electrons are only allowed to move on certain orbits, corresponding to discrete values of the orbital momentum  $L = n\hbar$  with  $n = 1, 2, 3, \dots$ . The emission of light by the atom corresponds to the emission of photons during the transition of an electron between two orbits. As the orbits are quantized, only discrete values can be obtained for the photon energy and thin lines will be observed in the light emission spectrum.

This representation was a good illustration to grasp the general behaviour of the atom, but it was rapidly abandoned as it was not possible to describe it in a mathematically coherent way. In particular, the fact that the orbiting electron, bound to the nucleus by an electromagnetic field did not radiate and thus lose its energy was in contradiction with the Maxwell equations. A few years later, the advent of quantum theory provided a suitable mathematical framework to describe the atom. In this theory, a description of the atom (that still forms the basis of our present knowledge) has been given by Schrödinger in 1925. When applying the Schrödinger wave equation to the specific case of electrons in a three dimensional  $1/r$  Coulomb potential, one obtains the well-known hydrogen atom with electron orbitals defined by the quantum numbers of the electrons.

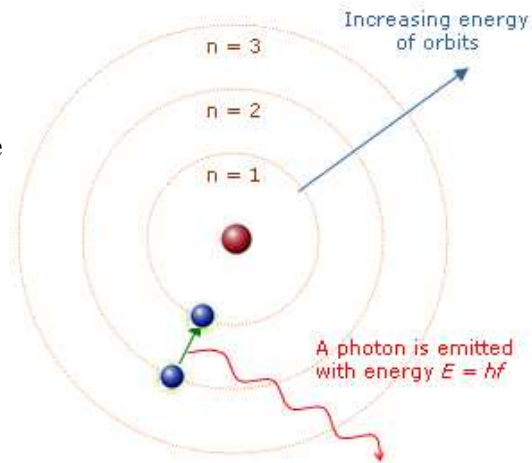


Figure 1.1: *Bohr model of the atom. A massive nucleus is surrounded by light electrons on discrete orbits.*

### More and more particles

In the first half of the 20<sup>th</sup> century, huge steps were made in both theory and experiment towards a deeper understanding of the sub-atomic world. On the theoretical side, the rapid development of quantum theory and its application to the recently discovered particles lead to the prediction of various new particles. On the experimental side, new tools were rapidly developed and improved to observe these new predicted particles, and sometimes to discover unknown particles with unexpected properties. Cloud chambers (C. T. R. Wilson, 1911) were commonly sent high in the atmosphere with balloons or used high in mountains in the 1930s

to observe and study the nature of cosmic rays. On the earth, particle accelerators are used since the creation of the cyclotron by E. Lawrence in 1930. This, together with the bubble chamber, invented by D. A. Glaser in 1952 were very successful tools that led to the discovery of many new particles.

The neutron, already suspected by E. Rutherford in 1920, was discovered by J. Chadwick in 1934, thus definitely settling our actual view of the atom composed of a small massive nucleus (more than 99% of the atomic total mass) made of positive protons and neutral neutrons surrounded by negative electrons. In this simple picture, a problem arose. If the nucleus was only made of positive and neutral particles, it would rapidly disaggregate under the influence of electromagnetic repulsion. A new force, stronger than the electromagnetic force (whence the name *strong force*) had to be introduced to explain the stability of the nucleus. In 1934, H. Yukawa made the hypothesis that a new particle he called *pion* was the mediator of such an interaction, by analogy with the photon being the particle exchanged in an electromagnetic interaction. In order to explain the short range of the strong force, the pion had to be a massive particle, of the order of 100 MeV. Similarly to the photon, the pion was also supposed to exist not only virtually during strong interactions, but also to be observable as a free particle and was intensively looked for. In 1937, a new particle discovered by S. H. Neddermayer and C. D. Anderson with a mass of  $\sim 130$  MeV was a good candidate for the Yukawa meson. However, its properties in the interaction with matter were in contradiction with its expected behaviour and it was rapidly ruled out to be the Yukawa pion. The particles discovered in this experiment were in fact muons. The pions were discovered in 1936 by D. H. Perkins in cosmic rays. Two charge states, the positive  $\pi^+$  and negative  $\pi^-$  were revealed by the traces left in a photographic emulsion. A third pion with a neutral charge, the  $\pi^0$  was also required for this description to be complete. It was firmly established by W. K. H. Panofsky, R. L. Aamodt and J. Hadley in 1951 in the analysis of photon pairs (detected by a pair spectrometer) issuing from the collision of charged pions produced with the Berkeley synchrotron and an hydrogen target. In other words, this was the first  $\pi^- p \rightarrow \pi^0 n \rightarrow \gamma\gamma n$  reaction ever produced in an accelerator.

During this period, two other particles loosely related to our field were detected. The first antiparticle, the positron, was discovered by C. D. Anderson in 1932. This was a striking confirmation of the Dirac equation (written in 1920 to describe the behaviour of spin 1/2 elementary particles) which predicted the existence of such antiparticles. The neutrino, introduced by W. Pauli in 1930 to give a correct interpretation of the neutron  $\beta$  decay was discovered in 1959 by C. Cowan and F. Reines in the study of the  $\bar{\nu} p \rightarrow n + e^+$  reaction in a large volume of liquid scintillator.

In the second half of the 20<sup>th</sup> century the list of new particles increased very fast. The first strange particles discovered in the 1940s (kaon in 1943,  $\Lambda$  in 1947) were the last new particles to be detected in cosmic rays. These unexpected particles were decaying with the strong interaction, but had a much longer lifetime than

other particles decaying that way. For this reason, they were difficult to include in the existing theory and were named *strange* particles. In 1954, M. Gell-Mann put some organization in these new particles by introducing a new quantum number, the strangeness, to characterize them. The next particles were observed in accelerators: in 1953, a new particle was discovered at the Chicago Cyclotron by H. L. Anderson, E. Fermi and collaborators. It is today known as the  $\Delta(1232)$  and was the first nucleon resonance to be discovered. The  $\Sigma(1385)$  was discovered in 1960, the  $\rho$ ,  $\omega$  and  $\eta$  mesons and the  $K^*$  -the first meson resonance- in 1961, the  $\phi$  meson in 1963 and so on . . .

### Quark models

With the rapid discovery of new particles - more than 200 in the 1960 - it was desirable to find some organizational principle to put some order in this zoo (as did D. Mendeleev with atoms a century earlier). The most successful classification system was proposed by M. Gell-Mann and independently by Y. Ne'eman in 1961. It is based on group theory (SU(3)) and classifies hadrons with same spin and parity as a function of the third component of their isospin and their hypercharge<sup>3</sup>. According to the rules of group theory, the particles are classified in multiplets: the baryons with  $J^P = \frac{1}{2}^+$  are contained in an octet (fig. 1.2), the baryons with  $J^P = \frac{3}{2}^+$  in a decuplet (fig. 1.3), the vector mesons ( $J^P = 1^-$ ) in a singlet and an octet (usually represented as a nonet, fig. 1.4 ) as well as the pseudoscalar mesons ( $J^P = 0^-$ , fig. 1.5). At the time, not all particles forming the multiplets had yet been discovered. The prediction of new particles and their detection in the following years was a huge success of this model. The discovery of the pseudoscalar  $\eta$  in 1961 with all its properties in good agreement with the ones predicted by the model was a first good confirmation. In the baryon decuplet, the existence of a  $J^P = \frac{3}{2}^+$  baryon with a strangeness  $S = -3$  and a mass of around 1680 MeV was also predicted by the model and had never been observed. In 1964, this  $\Omega^-(1672)$  baryon was discovered at Brookhaven in a triumphal confirmation of the SU(3) model.

Naturally, it was expected that these patterns in the hadron classification were not fortuitous and would eventually reveal an internal structure of the hadrons. An interpretation of these structures was given by M. Gell-Mann and independently by G. Zweig in 1964. According to their work, the SU(3) structure appearing in the classification of hadrons can be easily explained if the hadrons are not treated as fundamental particles but composed of three smaller particles that Gell-Mann named *quarks*. The three kinds of quarks are named *up* (u), *down* (d) and *strange* (s) and some of their properties are summarized in table 1.1. In this point of view, each baryon is made of three quarks and each meson of a

---

<sup>3</sup>Y = B+S, the sum of the baryon number (B = 1 for baryons and 0 for mesons) and the strangeness. (Sometimes, as in the figures on next page, the strangeness alone is used instead of the hypercharge).

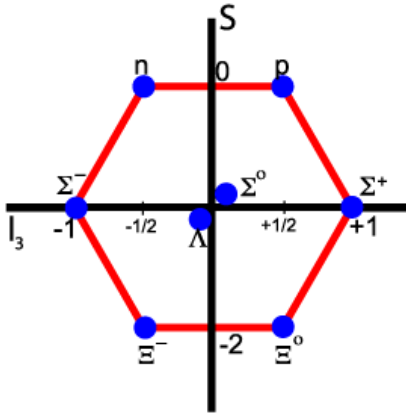


Figure 1.2: Classification of  $J^P = \frac{1}{2}^+$  baryons in an octet as a function of the the third component of the isospin and the strangeness.

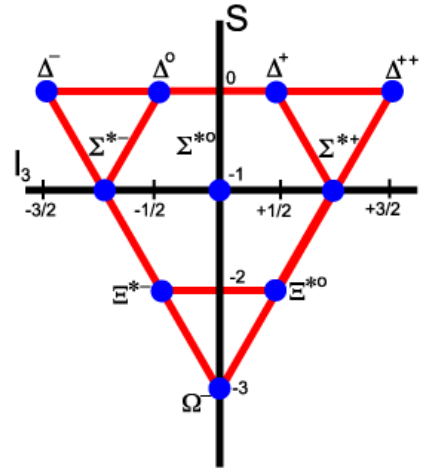


Figure 1.3:  $J^P = \frac{1}{2}^+$  baryons decuplet.

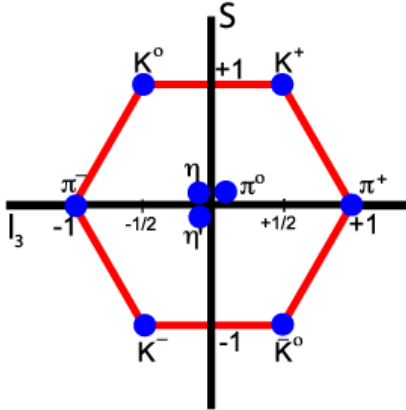


Figure 1.4: Pseudoscalar mesons nonet (octet+singlet).

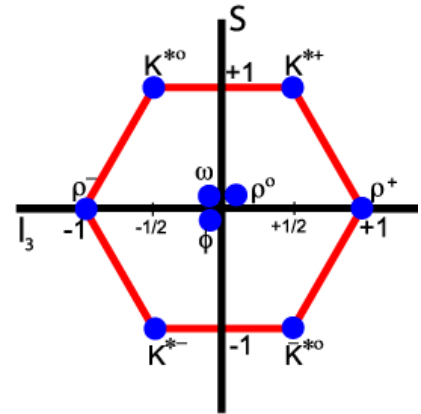


Figure 1.5: Vector mesons nonet.

quark and an antiquark. Using the combination rules of SU(3), one reproduces the multiplet structure of fig. 1.4 and 1.5 ( $3 \otimes 3 = 1 \oplus 8$ ). In a similar way, all existing baryons can be constructed, and the octet and decuplet structure explained, when forming all possible combinations of three quarks according to SU(3) ( $3 \otimes 3 \otimes 3 = 1 \oplus 8 \oplus 8 \oplus 10$ ).

This representation is a very elegant explanation for the multiplet structure of the hadrons but poses a problem. In the baryon decuplet (fig. 1.3) the quark content of the three particles situated at the corners are  $\Delta^{++} = uuu$ ,  $\Delta^- = ddd$  and  $\Omega^- = sss$ . As the spin of these baryons is  $3/2$ , the three spin  $1/2$  quarks must have their spins aligned and are therefore in the same quantum state. Since the quarks are fermions, they must obey the Fermi statistics and the baryon wave function should be antisymmetric under the exchange of two quarks, which is obviously

not the case, thus being in contradiction with the Pauli exclusion principle. In order to overcome this problem, each quark is assigned a new quantum number, the *color* which can take three values: *red*, *green* and *blue*. In order to restore compatibility with the Pauli exclusion principle, the color part of the wave function is organized to be antisymmetric under the exchange of two quarks so that - with the rest of the wave function being symmetric - the total wave function of the baryon is symmetric.

### The structure of the nucleon

The quark model is an elegant way to explain the classification of hadrons in multiplets but was thought - as it was the case for atoms some 150 years earlier - by many, including Gell-Mann, to be a mathematical artifact and have no physical justification. Indeed, quarks had never been observed though, as massive, charged particles, they would be easy to detect. In order to test the quark model assumptions and probe the structure of hadrons, new experiments that didn't rely on hadron spectroscopy had to be thought of. One of the most prominent was *deep inelastic scattering* (DIS) of leptons by nucleons. In this kind of experiments, high energy electrons (and later muons and neutrinos) were sent to nucleon targets and interacted with a large energy transfer  $Q$  so that the final state consists of more particles than the initial lepton and nucleon. In 1969, an important DIS experiment in which 15 GeV electrons were scattered by protons was performed at SLAC and showed that the structure functions of the proton (roughly, the functions describing the internal structure of the protons) did not depend<sup>4</sup> on the energy transfer  $Q$ . This fact was the evidence for point like partons<sup>5</sup>, but could not be fully explained with the simple assumption that the protons are made of three point like quarks. A more comprehensive interpretation of this experiment and subsequent ones was given (among others) by R. Feynman and led to the following description of the proton, illustrated in fig. 1.6.

The proton (and other baryons) are made of three valence quarks, as stated by the Gell-Mann model. In addition, quark-antiquark pairs from the *sea* are also present within the proton, as revealed by DIS. Such pairs only exist for a short time and don't have an influence on the quantum numbers of the proton. Moreover, some neutral, spin 1 partons -nowadays known as gluons- are also present inside the nucleon. These conclusions were put in a more formal context some years later with the rapid development of *quantum chromodynamics* (QCD), the theory describing the strong interaction between quarks. In a similar way to the electromagnetic interaction which is described by the exchange of photons

---

<sup>4</sup>A detailed explanation of this so called 'Bjorken scaling' would not fit here. More informations can be found in the references cited at the end of this section.

<sup>5</sup>This is how Feynman called the different constituents of the hadrons

between two charged particles, QCD describes the strong interaction with the exchange of particles called gluons between the quarks. In QCD however, the force between two quarks has different properties than the electromagnetic force, leading to a dramatically different behaviour of the strong force. First, the force between two quarks doesn't diminish with distance as does the electromagnetic force. On the contrary, with an increase in the distance, the force tends to a constant value. In order to separate two quarks one would therefore need to provide an infinite energy. For this reason, the quarks will never be observed as free particles. This property is called *confinement*. At the other side, the force between two quarks diminishes with the distance, so that it is approximately possible to treat the quarks inside the hadrons as free, non-interacting particles. This is called *asymptotic freedom*.

Today, our description of the proton is still based on three valence quarks and numerous quark-antiquark pairs bound by gluons as in fig. 1.6<sup>6</sup> in the firmly established quantum field theory of QCD. In a technical point of view, QCD is a very complex theory and is still nowadays a major research field in theoretical physics. Physicists currently try to predict the behaviour of strongly interacting particles with different methods. They can use discrete formulations of QCD and perform simulations on the lattice with powerful computers (*Lattice QCD*). They also work with versions of QCD restricted to certain conditions (Effective field theories such as *chiral perturbation theory*) or even try to work with QCD without any simplification using Yang-Mills theories.

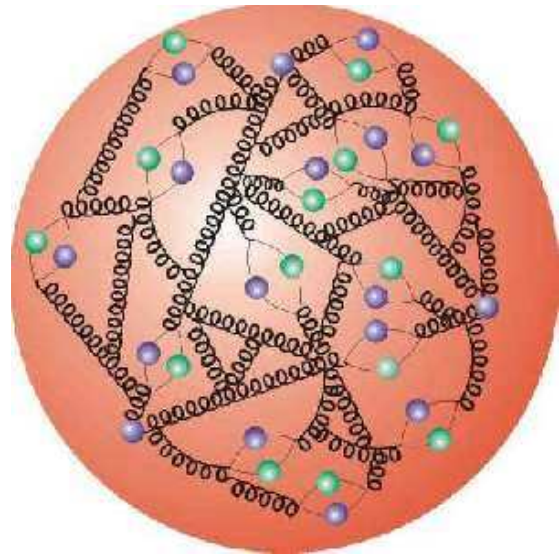


Figure 1.6: *Artist view of the interior of a proton. The three valence quarks are surrounded by quark-antiquark pairs and gluons that forms the main fraction of the mass of the proton.*

### Today and tomorrow

In the last thirty years of the 20<sup>th</sup> century, the discovery of new particles led to the formulation of the current description of the sub-atomic world, the *standard model*. A new quark, the charm quark predicted in 1970, was found in 1974 with the detection of the  $J/\psi$  meson. Two more quarks, the bottom and top quarks predicted by M. Kobayashi and T. Maskawa in 1973 were discovered in 1977 and 1995 respectively. In 1960, S. Glashow, A. Salam and S. Weinberg unified the

<sup>6</sup>This representation helps to understand why the mass of the nucleon is of the order of one GeV, while the mass of the individual quarks is only some MeVs. Most of the mass is made of sea quarks and gluons.

## 1.1. THE STRUCTURE OF MATTER, 2500 YEARS OF INTERROGATIONS<sup>9</sup>

weak and electromagnetic forces in a same formalism. This theory, usually referred to as the electroweak interaction, predicted the existence of three massive bosons ( $W^+$ ,  $W^-$  and  $Z^0$ ) as mediating particles of the weak force. These particles were observed for the first time at CERN in 1983. The electroweak theory had also to introduce a new particle in order to be consistent and explain the spontaneous breaking of the symmetry. This particle is called the Higgs boson and is the only one predicted by the standard model that hasn't be discovered so far.

The standard model, as it is known today consists of 25 particles and their antiparticles<sup>7</sup> and is summarized in table 1.1. The building blocks of matter are the 6 quarks from which all hadrons are formed and the 6 leptons. The interactions between these particles is mediated by 8 gluons, three massive vector bosons ( $W^+$ ,  $W^-$  and  $Z^0$ ) and the photon responsible for the strong, weak and electromagnetic forces respectively. This is completed with one (or several) Higgs bosons.

FORCES				MATTER: leptons		
Strong force	8 gluons			$e^-$	$\mu^-$	$\tau^-$
Weak force	$W^+$ , $W^-$ , $Z^0$			$\nu_{e^-}$	$\nu_{\mu^-}$	$\nu_{\tau^-}$
Electromagnetic force	$\gamma$					
MATTER: quarks						
	charge	mass	$J^\pi$	strangeness	isospin	$I_3$
u	2/3	1.5 to 3.0 MeV	1/2 <sup>+</sup>	0	1/2	1/2
d	-1/3	3 to 7 MeV	1/2 <sup>+</sup>	0	1/2	-1/2
c	2/3	1.25 ± 0.09 GeV	1/2 <sup>+</sup>	0 (charm = -1)	1/2	1/2
s	-1/3	95 ± 25 MeV	1/2 <sup>+</sup>	-1	1/2	-1/2
t	2/3	174.2 ± 3.3 GeV	1/2 <sup>+</sup>	0 ('bottomness' = -1)	1/2	1/2
b	-1/3	4.20 ± 0.07 GeV	1/2 <sup>+</sup>	0 ('topness' = -1)	1/2	-1/2

Table 1.1: *The particles of the standard model (without Higgs boson) with some properties of the quarks. For more details, see [PDG06].*

Every particle, every phenomenon in the sub-atomic world can be explained with these particles in the underlying framework of quantum field theories, QCD and QED: even the most tricky features discovered in particle physics so far, such as CP violation (1964) and neutrino oscillation (late 1960s) found an explanation within the standard model.

Today, the state-of-the-art experiments are designed to test the standard model. For example, an intensive research program is performed with large scale detec-

<sup>7</sup>For the particles that aren't their own antiparticles, such as the  $\gamma$ , the  $Z^0$  and maybe the neutrinos

tors to determine the absolute value of the neutrino mass. The most famous experiment however is the LHC at CERN which will in the near future try to detect the mediatic Higgs boson, to produce quark-gluon plasmas in which quarks are supposed to behave as free particles and to study CP violation in B meson systems (already observed by BaBar and Belle) for a better understanding of the matter-antimatter asymmetry. Eventually, the ultimate challenge of the 21<sup>th</sup> century physicist will be to find some new physics that can't be described by the standard model. Some experiments such as the search for new unknown *weakly interacting massive particles* in cosmic rays are under way, but up to now, no hint for physics beyond the standard model has been observed yet.

### Sources

This historical overview is mostly based on the lectures given by professors A. Bay and O. Schneider in the years 1998 to 2001 at the university of Lausanne (today EPFL), on [Cah89], a collection of historically important publications with vivid introductory text and the very didactic [Wil91] textbook. Some various minor sources from the internet have also been used.

## 1.2 Nucleon resonances

As a contribution to a deeper understanding of the nature of matter, the goal of our experiment is to shed more light on the field of nucleon resonances. In this section, we will introduce this large field by giving a short definition of what resonances are and of the main challenges associated to their study. Some resonances such as the  $\Delta(1232)$  or the  $\Omega^-(1672)$  have already been mentioned for their historical importance. In the last 30 years, much more have been discovered and today, the study of resonances is a very active field in current research. There are two reasons for this. First, the field of nucleon resonances is a very complex one and lots of its secrets are still to be understood properly as we will give an account in this section. Secondly, -and more pragmatically- the study of resonances happens at relatively low energies, the standard energy of the probes used to excite nucleons ranges between 100 MeV and 10 GeV. Such energies are easily obtained in quite a lot of reasonably scaled facilities such as MAMI (see section 3.1).

Admittedly, the energy scale is not a mere problem of money and accelerator size. On the contrary, it plays the key role in the theoretical description of resonances. At very high energies, we have seen in the last section that deep inelastic scattering experiments give an easy access to the inner structure of the nucleons which can be described as made of three valence quarks surrounded by numerous quark-antiquark pairs from the sea bound together by gluons (as shown in fig. 1.6). This well established picture is obtained in the framework of QCD which

is treated in a perturbative way, expanded in powers of  $\alpha_s$ , the strong coupling constant, which, at such high energies is very small. At lower energies, at which the nucleon resonances can be observed, this is not possible anymore. The strong coupling constant becomes large ( $\alpha_s \approx 1$  at 1 GeV) and the perturbative expansion of QCD doesn't make any sense anymore. A perfect description of the hadrons would be provided by a non-perturbative treatment of QCD. Due to the nature of QCD, this is an immensely difficult task which is today out of reach. In order to overcome this problem, simplified solutions for QCD have to be developed. Lattice QCD and effective field theories have already been mentioned but both approaches are limited: lattice QCD by the available power of computers used to perform simulations and effective field theories by the scope of physics they try to describe, thus lacking a global description.

The models that were the most successful in making predictions on hadron properties are *constituent quark models*. The principle of such models is quite simple. Instead of giving a description of the hadrons based on their full internal structure (which was anyway unknown in 1964 when the first version of this kind of models was proposed following Gell-Mann's quark hypothesis), one postulates that the hadrons are made of so-called *constituent quarks* only, with no further internal component. As an example, the proton is made of two u and one d constituent quarks. In this point of view, the quarks are not point like any more and, since they are the only subcomponents of the proton, they share its total mass. As a consequence, the constituent quark masses are much heavier -between 220 and 330 MeV for the u and d quarks, depending on the models- than the bare quark masses given in table 1.1.

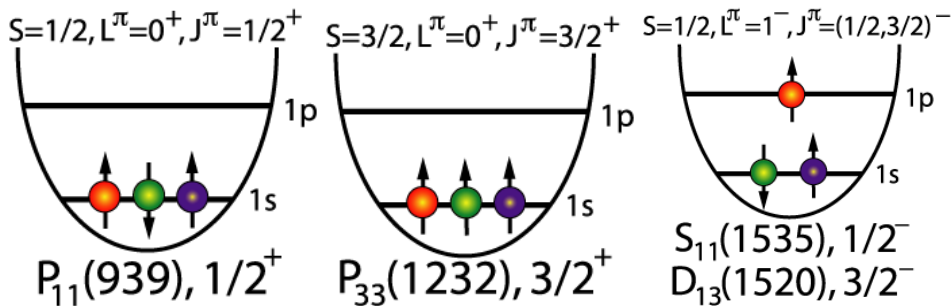


Figure 1.7: *The nucleon and the three lowest lying nucleon resonances in a simplified constituent quark model.*

In the simplest models, the three constituent quarks are placed in a confining potential in which the quarks interact via short range residual interaction described by one-gluon-exchange. As an illustration, fig. 1.7 shows how the lightest resonances in the nucleon spectrum can be constructed by placing three quarks in

a simple harmonic oscillator. In the nucleon ground state (fig. 1.7a<sup>8</sup>), the three quarks are arranged in the state requiring the lowest energy. All three quarks are placed on the 1s state with the spin of two quarks aligned and the third spin in the other direction. The first excited state is obtained by flipping the spin of the third quark, so that the three quarks remain on the 1s state but now with all their spins aligned. This is the well known  $P_{33}(1232)$  usually referred to as the  $\Delta$  resonance. The next resonances are obtained by moving one quark on the 1p state. (As  $L > 0$ , more than one resonance can be build in this configuration, see the quantum numbers at the top of fig. 1.7). The combination with the spins oriented such as in fig. 1.7c is the first available. It gives rise to two resonances, the  $S_{11}(1535)$  and the  $D_{13}(1520)$ , members of what's usually referred to as the *second resonance region*. At higher energies, an arbitrary number of resonances can be build using this procedure.

In this simple illustration, we have seen how the lowest lying resonances are build from the effective degrees of freedom of the model. Over the years, models based on this principle have been developed with more and more refinement and today are able to make accurate predictions about the properties of hadrons. However lacking a strong physical justification, (we *know* that the structure of baryons is much more complex that three constituent quarks only) they have provided large amounts of accurate predictions in hadronic spectra or in the electromagnetic and strong coupling of resonances and are still today our major source of theoretical data with which the results of our experiments are compared. For more information, see [Cap00], a very good review article on quark models.

Experimentally, our goal will be to produce resonances and measure their properties as precisely as possible to test quark models. The most common decay mode -higher than 99 % for all resonances- is via strong interaction and the emission of mesons. In fig. 1.8 we show the lowest lying nucleon resonances with their respective mesonic decay channels (the width of the arrow is proportional to the intensity of the coupling to the corresponding decay channel). At this point, an experimental difficulty arises: due to the strong nature of their decay, the resonances have a very short lifetime, and are therefore quite broad, with widths of the order of 100 MeV. This is represented in fig. 1.8 in which each resonance is drawn with a halo proportional to its width. Apart from the  $\Delta$  resonance wich appears isolated at 1232 MeV, resonances lay quite close to other resonances and thus strongly overlap as do the  $P_{11}(1440)$ , the  $D_{13}(1520)$  and the  $S_{11}(1535)$  in the *second resonance region*. For this reason, the study of excitation spectra alone will not be sufficient to provide an accurate description of individual resonances. Some methods used to disentangle resonances will be presented in the next chap-

---

<sup>8</sup>Fig. 1.7 uses the standard notation. A resonance is written in the form  $L_{2I}J(W)$  where L is the orbital momentum of the nucleon-pion pair from the resonance decay (in the spectroscopical notation: L=0,1,2,3,... corresponds to S,P,D,F,...). I is the isospin of the resonance, J its total angular momentum and W its mass.

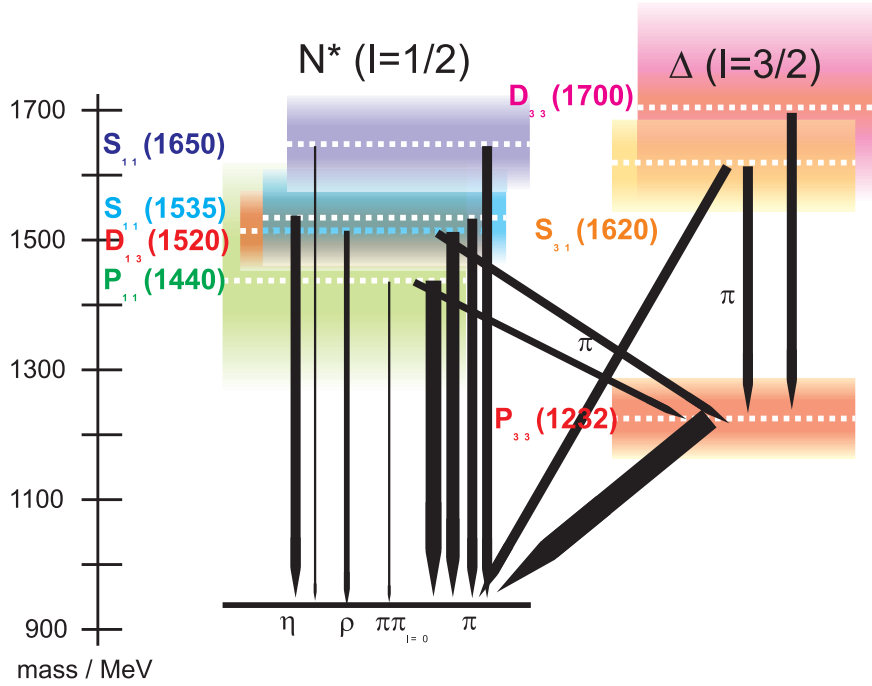


Figure 1.8: *Nucleon excitation spectrum showing the lowest lying resonances. The black arrows show the mesonic decay of this resonances with width proportional to the branching ratio. The shaded coloured areas represent the width of the resonances.*

ter.

Without going further into details at this point, let's mention the main interrogations arising in the study of nucleon resonances. The first one is the problem of *missing resonances*. In most models, the number of predicted resonances is higher than the number of observed resonances. Even in models with a smaller number of effective degrees of freedom (and therefore less predicted resonances) such as diquark-quark models in which the nucleon is made of two elements: a quark and a strongly bound quark pair, the number of predicted resonance is still too large. This discrepancy can have two origins. It can be that the models effectively predict too much resonances and have to be corrected with the addition of further constraints. Alternatively, it might be that much more resonances exist but couple very weakly to the particles commonly used to excite nucleons and, for this reason are very difficult to observe in our experiments.

Another major questioning is related to the nature of resonances. Along with the existence of three quark resonances, QCD predicts that exotic baryons can also exist. Such exotic states can be hybrid hadron, which are formed when one of the gluons inside the nucleus is excited instead of one of the quarks, as it is normally the case. Some other exotic states with different number of quarks, such

as tetra- and pentaquarks are also theoretically allowed<sup>9</sup>. As the decay channels for such exotic baryons are not a priori different from standard ones, the nature of resonances is not easily determinable and indeed, some resonances such as the  $P_{11}(1440)$  (or 'Roper resonance') have been proposed as candidates for hybrid baryons. In order to help us to provide a deeper understanding on these questions, more constraints to the models will be added by the precise measurement of the resonances properties and their comparison with the model predictions.

---

<sup>9</sup>Even the existence of states (that would anyhow be mesons) without any quarks, the glueballs, is not ruled out.

## 2 Theoretical models

*In the first chapter, we have introduced the field of nucleon resonances and presented the fundamental questions that show up in their study. In this chapter, we will delve more into details and present how nucleon resonances can be studied via meson photoproduction. We will first give an account on how the resonances are produced using high energy photons and the advantages (and drawbacks) of this method compared to other ones such as the well developed pion induced reactions. We will then present the decay of these resonances into mesons, its mechanism and the informations it can provide about the resonances with of course a strong emphasis on double pion photoproduction. Finally, we will go one step further into details and give a summary of the important features of the most important models used to describe double pion photoproduction in the second resonance region as well as the chiral perturbation theory model used to predict the double  $\pi^0$  cross section close to threshold.*

### 2.1 Studying resonances with meson photoproduction

In the last chapter, we have seen that the most prominent decay of nucleon resonances is via the emission of mesons. This is illustrated in fig. 1.8 for the lightest resonances. Knowing this, the most obvious method to produce resonances is to excite nucleons with beams of long-lived mesons ( $\pi^+$ ,  $\pi^-$ ,  $K^+$ ,  $K^-$ ). Such methods are easy to carry out experimentally and have been widely used with ever increasing refinements so that they form today a large part of our knowledge on nuclear resonances. In particular, rich information has been gathered with elastic and inelastic scattering of charged pions by nucleons. This approach, though very successful, is limited in its scope. Only mesons whose lifetime is long enough for them to be produced, collimated in secondary beams and sent to a nucleon target can be used as probes. As a consequence, resonances that couple weakly to charged pion channels won't be produced in a significant amount, making their investigation impossible.

In order to overcome this limitation, alternative ways with different probes have

to be thought of for the investigation of resonances. The use of high energy real<sup>1</sup> photons -as in this work-, meson photoproduction, has been a very active field over the past fifteen years. With the advent of continuous electron accelerators providing high quality tagged photon beams (such as MAMI, see section 3.1) a precise survey of the nucleon resonances with this technique was made possible.

The principle of resonance excitation in meson photoproduction is sketched in fig. 2.1. A high energy photon interacts with a nucleon, forming a resonance which decays back into the nucleon ground state via emission of a meson, in this case an  $\eta$  meson. The main advantage of this process compared to pion induced reactions is the presence of an electromagnetic vertex (at formation) and a strong vertex (at decay), allowing the study of both couplings in a single experiment. At the electromagnetic vertex, very different informations are provided since the photon only couples to the spin and flavor degrees of freedom of the quarks, thus revealing their spin flavor configurations which are related to configuration mixing predicted by the models. On the downside, the cross sections are much smaller for electromagnetic than for hadronic excitations. In addition, the contribution of background processes (such as Born terms or vector meson exchanges) plays a significant role and thus blurs our identification of resonances. This will be treated with more details in the next section for the case of double pion production. This, together with the practical unfeasibility of 'complete'<sup>2</sup> experiments, makes the determination of hadron properties (mass, width, ...) from the results of our experiments (cross sections, angular distributions, asymmetries, ...) quite difficult. For this purpose, sophisticated *reaction models* have to be developed as a link between experimental results and resonances.

In spite of these difficulties, meson photoproduction has been widely used to excite nucleons in experiments on free protons and on light and heavy nuclei and has brought more light on our understanding of resonances. Today, the easiest available excited state, the  $\Delta(1232)$  resonance is a very well known state due to the thorough investigation of the  $\gamma N \rightarrow \Delta \rightarrow \pi N$  reaction. Its basic characteristics such as mass, width and electromagnetic couplings have been measured up to a great accuracy. In addition, the ever increasing precision of experiments has allowed the investigation of more complex features of this state such as the helic-

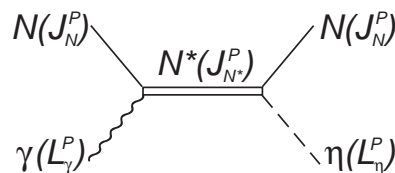


Figure 2.1: *Principle of meson photoproduction with an intermediate nucleon resonance.*

<sup>1</sup>Virtual photons can also be used in so-called electroproduction, by scattering electrons off nucleons. Protons and light nuclei beams are also commonly used as probes to form resonances in baryon-baryon interactions

<sup>2</sup>In a 'complete' experiment the number of measured observables is sufficient to determine the cross sections and other properties of the resonances without ambiguity.

ity dependence of its cross section, the isospin dependence of its excitation or its magnetic moment (For this latter, some introductory words are given in section 2.7), providing stringent tests of the quark models used to describe this resonance.

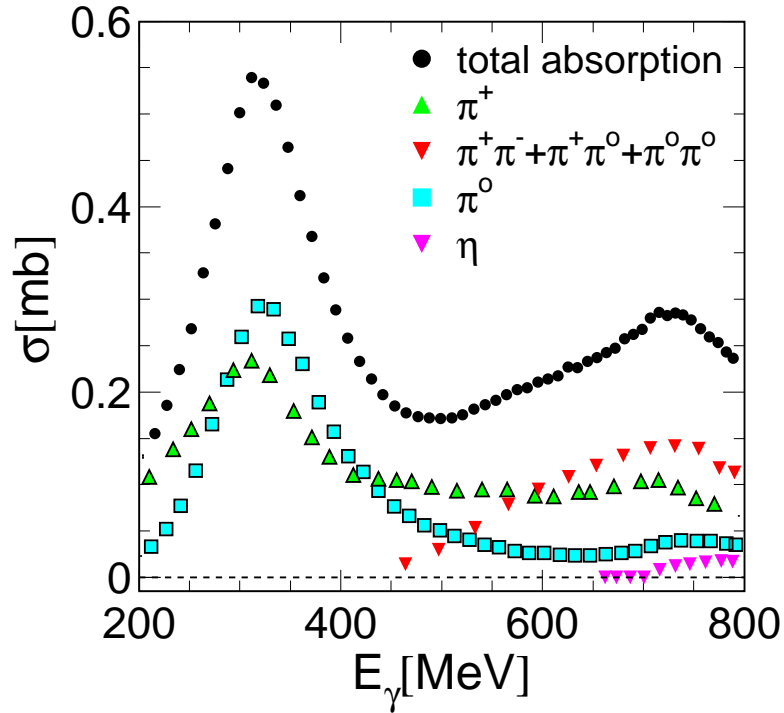


Figure 2.2: Total cross section for meson photoproduction with contribution of individual channels ([Kru03] and subsequent references).

In the second resonance region, the situation is made more complicated by the presence of three strongly overlapping resonances, the  $P_{11}(1440)$ ,  $D_{13}(1520)$  and  $S_{11}(1535)$ . Moreover, as an opposite to the  $\Delta$ , these resonances decay into various mesons, giving  $N\pi$ ,  $N\eta$  and  $N\pi\pi$  final states as represented in fig. 2.2. In this region, the first challenge is therefore to find methods to disentangle these resonances and understand their individual contributions. This has been precisely done for single pion photoproduction in which detailed partial wave analysis have provided a good separation of the three resonances for this channel.  $\eta$  photoproduction is a favourite of experimentalists and theorists as it allows a precise study of the  $S_{11}(1535)$  resonance. This resonance has the unique advantage to have a much larger branching ( $> 50\%$ ) into  $N\eta$  than any other resonance. This fact is difficult to explain within the framework of quark models and has triggered many interrogations and many publications about the nature of the  $S_{11}(1535)$ . Finally, and this is the purpose of this work, our understanding of the second resonance region wouldn't be complete without an accurate description of the

double pion channel which contributes to more than half of the cross section in this energy region. Double pion photoproduction will be extensively discussed in the next chapters.

The field of meson photoproduction is very active and much more is done than what was mentioned in this introductory section. In particular, targets heavier than free protons are also commonly used. Light nuclei targets, and especially deuterium targets, are very useful to study meson photoproduction off the neutron in quasifree kinematics, whereas photoproduction on heavy nuclei is used to investigate in-medium modifications of resonances and mesons. For extensive review articles on the subject, see [Kru03] for photoproduction off free protons and light nuclei and [Kru05] off heavy nuclei.

## 2.2 The double pion channel

So far, the first chapters have introduced the physical context in which this work is performed. The title, 'Double pion photoproduction off the proton at threshold and in the second resonance region' should now make more sense for the reader. Starting from here, we will focus on double pion photoproduction alone and give as much detailed as possible a description of this channel. The theoretical work outlined here will be detailed in the next section.

Double pion photoproduction is a generic term that includes all processes in which a high energy photon interacts with a nucleon and produces a final state with two pions. In our work, in which a free proton target is used, the three following isospin channels are obtained.

$$\gamma p \rightarrow \pi^0 \pi^0 p \quad \gamma p \rightarrow \pi^+ \pi^0 n \quad \gamma p \rightarrow \pi^+ \pi^- p \quad (2.1)$$

As stated, our goal is to provide a better understanding of nucleon resonances. Accordingly, we will classify the large number of processes leading to double pion final states in two families: the *good* events, suited for this study, in which an intermediate resonance from the second energy region is produced and the *background* events in which it is not the case.

Good events happen when an excited state forms during the  $\gamma$  - p interaction. The two pions come from the decay of the resonance back into the nucleon ground state. In fig. 1.8 we have shown the possible decays of the resonances into  $\pi$ ,  $\eta$  and  $\rho$  mesons. Based on this, three different decay schemes involving two pion final states are possible. Fig. 2.3 shows these three possibilities with examples involving resonances from the second resonance region.

According to a majority of the models, the mechanism that contributes mostly to double pion production is the *sequential decay* of the resonance. In this case,

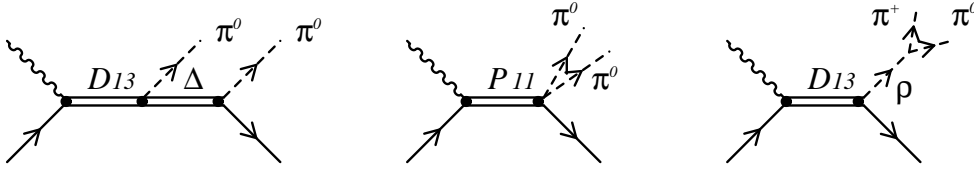


Figure 2.3: *Feynman diagrams of resonant contributions to double pion final states.* Left: *sequential decay of the  $D_{13}(1520)$ .* Middle: *Direct decay of the  $P_{11}(1440)$  into a correlated pair of  $\pi^0$ .* Right:  *$\rho$  decay of the  $D_{13}(1520)$ .*

the excited state decays in a first step into an intermediate  $\Delta$  resonance via the emission of a first pion. The  $\Delta$  resonance then decays back into the nucleon ground state via the emission of a second pion. As an illustration, fig. 2.3a shows the  $\gamma p \rightarrow D_{13}(1520) \rightarrow \Delta \pi^0 \rightarrow p \pi^0 \pi^0$  process. This process is allowed for all resonances in the second resonance region and all three isospin channels and is especially worthwhile since it allows the study of resonance-resonance transitions. Together with sequential decay, two other process contribute. The first one is the *direct decay* of the resonance into two pions. In this case, the two final state pions are correlated in a relative s-wave<sup>3</sup>. This is illustrated by the  $\gamma p \rightarrow P_{11}(1440) \rightarrow p(\pi^0 \pi^0)_{S=0}^{I=0}$  reaction which is the only one of this kind allowed for resonances in the second energy region. Finally, the resonance can also decay into a  $\rho$  meson which then decays into two pions. This is shown in fig. 2.3c for the  $\gamma p \rightarrow D_{13}(1520) \rightarrow \rho^+ n \rightarrow \pi^+ \pi^0 n$ . Since the  $\rho^0$  meson doesn't decay into two  $\pi^0$ , this mechanism only contributes to  $\pi^+ \pi^- p$  and  $\pi^+ \pi^0 n$  final states. These last two decay mechanisms are less frequent than sequential decays, but their correct handling has been the key for a correct description of all three double pion isospin channels as we shall see later in the presentation of the individual models.

Double pion photoproduction is not a 'clean' signal for the study of resonances and lots of background terms involving non-resonant mechanisms contribute to the total cross section. The most important part of this background is due to Born terms.

In fig. 2.4, we show some examples of N-Born terms and in fig. 2.5 two important  $\Delta$ -Born terms, the  $\Delta$ -Kroll-Rudermann contact term and the pion pole term. These graphs arising in the lowest orders of the perturbative treatment of the scattering are not tricky to handle but involve many calculations due to the large number of possible mechanisms. In the most recent models, up to 25 Born diagrams can be included. Concerning this, there is however a significant difference between the channels with charged pions and the double  $\pi^0$  channel. For this latter, since the  $\pi^0$  doesn't couple to the photon, the number of allowed

<sup>3</sup>Such a correlated pair is sometimes seen as a very broad particle, the  $\sigma$  meson as in [PDG06]. For our work, this distinction is not important.



Figure 2.4: *Some examples of N-Born terms contributing to double pion cross section. The dashed lines represent all kind of pions. Only the first graph is allowed in the double  $\pi^0$  channel (see text).*



Figure 2.5: *Two examples of  $\Delta$ -Born terms. The  $\Delta$ -Kroll-Rudermann term (left) and the pion-pole term (right) contribute to the  $\pi^0\pi^+n$  and  $\pi^+\pi^-p$  channels.*

diagrams is strongly reduced, making this channel more suited for a clean study of the resonances. In our example, the diagrams 2.4b, 2.4c, 2.5a and 2.5b are forbidden and only 2.4a will contribute to the double  $\pi^0$  cross section.



Figure 2.6: *Background channels contributing to double pion production besides born terms. Left:  $\rho$  meson production. Right: Pion loop.*

Two other mechanisms also contribute to the total double pion cross section. The first one is the production of  $\rho(770)$  mesons whose branching ratio into two pions is close to 100%. (fig. 2.6a). At MAMI, this should however be largely suppressed since the available photon energy is below the kinematical threshold for this reaction. Therefore, the only  $\rho$  production should come from the low energy tail of this meson, adding only a small contribution to the cross section. In the following, we will see that this picture is only partially true and that a non-negligible contribution to the  $\gamma p \rightarrow n\pi^+\pi^0$  reaction is due to off-shell  $\rho$  mesons. Finally, so-called *pion loop* diagrams (fig. 2.6b) might also be added in the de-

scription of this channel. In the second energy region, they would only add a tiny contribution, and are therefore not included in the models. This is different at lower energies where they play a very important role in the description of cross sections at threshold. This will be developed in section 2.6.

## Experiments

On the experimental side, double pion photoproduction was first measured in the late 1960s. At that time, experiments were performed with untagged photon beams and bubble chambers as detectors. In these conditions, only charged particles could be clearly identified. The  $\gamma p \rightarrow p\pi^+\pi^-$  reaction was therefore the only experimentally available isospin channel. Its total cross section as well as invariant mass distributions were measured. An early model was developed for the interpretation of these results [Lük71]. It predicted that the reaction was dominated by background channels, notably the  $\Delta$ -Kroll-Rudermann and the pion-pole terms (fig. 2.5). More recent data and experimental models have confirmed this view of a background dominated channel in which the resonant processes -the  $D_{13} \rightarrow \Delta\pi \rightarrow \pi\pi N$  being by far the most important- only play a minor role. The total contribution of all resonances accounts for less than one third of the total cross section (see e.g. fig. 2.10).

The achievement of MAMI B in 1990 used with DAPHNE and TAPS detectors opened the way to the precise measurement of various reactions involving more than one neutral particle in their final state. In our case, the  $\gamma p \rightarrow p\pi^0\pi^0$  and  $\gamma p \rightarrow n\pi^+\pi^0$  reactions became available. With the first determinations of the double  $\pi^0$  cross section [Bra95], [Här97], a controversy in the nature of the reaction appeared. Two models, the Saclay and the Valencia model (see sections 2.3.1 and 2.3.2) had been designed to interpret these results. Both gave a reasonable description of the total cross section but were based on very different assumptions about the dominant underlying mechanism leading to double  $\pi^0$  final states. The Saclay model predicted a dominance of the  $P_{11}(1440) \rightarrow p(\pi^0\pi^0)_{S=0}^{I=0}$  decay while the Valencia model stated that the contribution of this diagram was very small, the main contribution being due to the  $D_{13}(1520) \rightarrow \Delta\pi^0 \rightarrow p\pi^0\pi^0$ . These doubts were lifted some years later in [Wol00] in which precise measurements of  $\pi^0\pi^0$  and  $\pi^0$  proton invariant mass distributions were in much better agreement with the Valencia model calculations. This confirmed the dominance of the  $D_{13} \rightarrow \Delta\pi$  decay<sup>4</sup>. Very recently, new data from the CB-ELSA collaboration [Tho08], [Sar08] have been published and show a good agreement with the previous results.

In the case of the  $\gamma p \rightarrow n\pi^+\pi^0$  reaction, the first cross section measurement

---

<sup>4</sup>However, a recent article [Aja07] uses again the Saclay model with a dominance of the  $P_{11}(1440)$  direct decay to reproduce new GRAAL results on double  $\pi^0$  photoproduction off the neutron.

[Bra95] was puzzling. The qualitative predictions of both Saclay and Valencia models were the same as in the case of the  $\gamma p \rightarrow p\pi^+\pi^-$  channel: the cross section was dominated by the  $\Delta$ -Kroll-Rudermann and the pion pole terms. Yet, both models underestimated the total cross section by  $\sim 50\%$ . The first explanation for this behaviour came with the Hiroshima model [Och97]. K. Ochi and collaborators investigated the contribution of diagrams involving  $\rho$  mesons and especially the  $D_{13} \rightarrow \rho n \rightarrow \pi^+\pi^0 n$  decay (fig. 2.3). The a priori expected contribution of these kind of diagrams in the studied energy region was small since the  $\rho$  meson threshold lies at 1086 MeV. With the energy available at MAMI, only a small contribution of the low energy tail of the  $\rho$  should have played a role. In their article, they showed however that a significative contribution due to off-shell  $\rho$  mesons was added to the total cross section, even at low energies. With this assumption, they achieved a reasonable reproduction of the  $\gamma p \rightarrow n\pi^+\pi^0$  cross section. This behaviour was then confirmed at MAMI [Lan01] in a precise study of the  $\pi^0 \pi^+$ ,  $\pi^0 n$  and  $\pi^+ n$  invariant mass distributions for this channel.

These results have all been performed with unpolarized photons and unpolarized targets. In the recent years, much work has been performed in measuring polarization observables which are much more sensitive to the details of the models and thus offer opportunities to study the individual contributions of resonances in a very precise way. This will be treated in section 2.5.

On the unpolarized side, this work is intended as a very high statistic measurement of the  $\gamma p \rightarrow p\pi^0\pi^0$  and  $\gamma p \rightarrow n\pi^+\pi^0$  reactions. Since the cross sections and the invariant masses distributions [Wol00], [Kot01], [Lan01] have already been measured with an accuracy sufficient to give a fairly good understanding of the underlying physics, no surprising new phenomenon is expected. Nevertheless, our precise data will provide very stringent conditions to further constraint the models and give a clearer view of the different processes contributing to the reaction. It will also give a clearer view of these observables in energy regions in which fewer data is available from previous experiments. Especially important will be the precise determination of the cross section of the double  $\pi^0$  channel close to threshold, a very important test for chiral perturbation theory (see section 2.6). Before going further, let's briefly mention that double pion photoproduction is also widely used on targets heavier than free protons. On light nuclei, and especially on the deuteron, the three other isospin channels,  $\gamma n \rightarrow \pi\pi N$ , are studied in quasifree kinematics. The comparison between cross sections on the proton and on the neutron is a valuable tool to disentangle the resonances. See for example the results of the analysis recently performed at ELSA in [Jaé07]. Double pion production is also a very important probe to study the behaviour of resonances inside the nuclear medium. A long standing quest in this field is the understanding of why the second resonance bump (see fig. 2.2) disappears when the reaction is performed on heavy nuclei. For more details on this subject, see e.g. [Blo07]. In this field new data on various heavy nuclei targets has also been taken during the same round of experiment as this work. The results will be

published soon. See [Lug07] and [Gre07].

## 2.3 Theoretical models for the double pion photoproduction

The principle on which most models are based was introduced in an early work by Lüke and Söding in 1971 [Lük71], an isobar model developed for the interpretation of  $\gamma p \rightarrow \pi^+ \pi^- p$  bubble chamber experiments. In these models, an effective Lagrangian density is build from a set of tree diagrams<sup>5</sup>. All type of diagrams presented in the previous section (resonant processes, N and  $\Delta$ -Born terms and other background processes) can be included. The difference between the models lies in the number of processes deemed by the author to play a significant role in the model and the couplings of the chosen diagrams to the double pion channels. This choice of diagrams is not a trivial task since the models are very sensitive to their internal details. [Lük71] was made of only 5 diagrams while the most recent models include up to 25 diagrams. As we will see, two relatively close models can lead to dramatically different predictions. Individual processes have to be treated carefully since they not only contribute to the models by themselves but also -and even processes having very small contributions by themselves- from interference with other diagrams. In the following, we will present four models that played an important role in the understanding of the double pion photoproduction channel. For each model, we will show the exhaustive list of diagrams used to build the effective Lagrangian density and we will emphasis on the innovations brought with respect with the previous ones. The previsions of the models -cross sections, invariant masses distributions, asymmetries, . . . - won't be explicitly shown here but will appear throughout chapter 7 in which they will be compared with our results.

### 2.3.1 Saclay model

When MAMI B started operation with the DAPHNE detector in the early 1990s (see section 3.1), it opened the way to precisely measure the  $\gamma p \rightarrow p\pi^0\pi^0$  and  $\gamma p \rightarrow n\pi^+\pi^0$  reactions. In order to give a correct interpretation of these newly available results, two models extending the work of Lüke and Söding to the two other isospin channels were developed: the Saclay and the Valencia models.

The Saclay model from L. Y. Murphy and J-M. Laget [Mur96] involved contributions from the  $P_{11}(1440)$ ,  $D_{13}(1535)$  and  $D_{33}(1700)$  resonances only. The other ones were said to have neglectable couplings to the double pion decay channel.

---

<sup>5</sup>Feynman diagrams without internal loops

The model also included some background  $\Delta$ -Born terms. Altogether, 12 diagrams have been used and are shown in fig. 2.7.

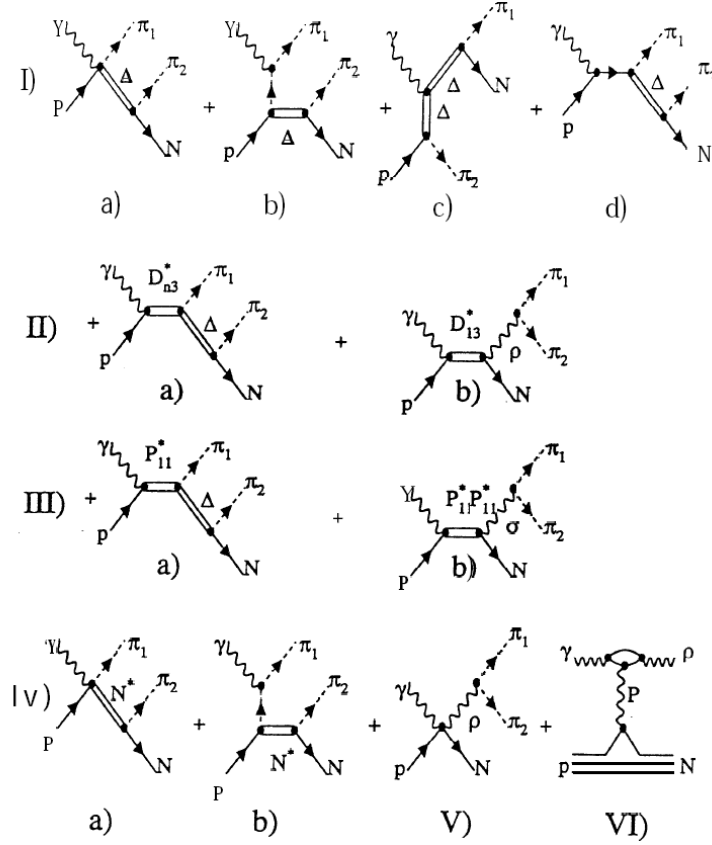


Figure 2.7: *Feynman diagrams used in [Mur96]. For the double  $\pi^0$  reaction, only diagrams Ic, Id, II, III and VI contribute.*

The main feature of this model was the strong contribution of the  $P_{11}(1440) \rightarrow p(\pi^0\pi^0)_{S=0}^{I=0}$  decay. This process was responsible for more than 75% of the total double  $\pi^0$  cross section. This model predicted the  $\gamma p \rightarrow p\pi^0\pi^0$  and  $\gamma p \rightarrow \pi^+\pi^-p$  cross sections with a reasonable accuracy but failed to reproduce the  $\gamma p \rightarrow n\pi^+\pi^0$  one. More important, the domination of the  $P_{11}$  direct decay into two  $\pi^0$  was in contradiction with  $\pi^0\pi^0$  invariant mass measurements performed later. This ruled out this model as a correct description for this double pion channels. Still, a recent article [Aja07] used this article to reproduce new GRAAL results for the  $\gamma n \rightarrow \pi^0\pi^0n$  reaction with a reasonable accuracy.

### 2.3.2 Valencia model

The Valencia model is another effective Lagrangian model. A first version of this model was published by J. A. Gómez-Tejedor and E. Oset in 1994 [Gom94]. Its purpose was to describe the  $\gamma p \rightarrow \pi^+ \pi^- p$  reaction and contained some 60 Feynman diagrams. A second version of this model with a slightly different scope was written in 1996 [Gom96]. Here, all six isospin channels of the  $\gamma N \rightarrow \pi \pi N$  reaction were accounted for, but with energies limited to the range available in Mainz ( $E_\gamma < 800$  MeV). It included 20 diagrams with contributions from the  $P_{11}(1440)$  and  $D_{13}(1520)$  as well as N and  $\Delta$ -Born and  $\rho$  background terms. At the time, this model was in competition with the Saclay model. Both gave an acceptable description of the  $\gamma p \rightarrow p \pi^0 \pi^0$  and  $\gamma p \rightarrow \pi^+ \pi^- p$  reactions while failing to describe the  $\gamma p \rightarrow n \pi^+ \pi^0$  channel. There was however a strong contradiction between the two models. In the Valencia model, the main contribution to the cross sections was due to the  $D_{13}(1520) \rightarrow \Delta \pi \rightarrow N \pi \pi$  sequential decay. As already stated, this behaviour was confirmed by  $\pi^0 \pi^0$  invariant mass analysis to the detriment of the Saclay model hypothesis of a  $P_{11}(1440) \rightarrow p(\pi^0 \pi^0)_{S=0}^{I=0}$  dominance.

In 2001, this model was improved to give a better interpretation of the  $\gamma p \rightarrow n \pi^+ \pi^0$  reaction [Nac01]. Diagrams of the  $\rho$  decay of the  $D_{13}(1520)$  resonance that were shown to play a crucial role in this channel ([Och97], see below) were included as well as contributions from the  $D_{33}(1700)$  resonance which adds a sizeable contribution to this channel via interference with the dominant processes. Fig. 2.8 shows the Feynman diagrams used in the latest version of this model.

Recently, this model has been extended to polarization observables. In [Nac02], the cross sections for spin-1/2 and spin -3/2 used to test the GDH sum rule (see e.g. [Ahr05] for more explanations). In [Roc05], the angular dependence of the helicity asymmetries of double pion photoproduction with polarized photons was studied. This last point will be discussed extensively in section 2.5.

### 2.3.3 Mainz model

Recently, a new model based on an effective Lagrangian approach was developed by A. Fix and H. Ahrenhövel within the so called Mainz MAID model [Fix05]. For the reader in the need of a deeper understanding, this article is worth reading since it provides a good discussion of the different models, of their achievements and of their challenges. This model is also a good illustration of the technical difficulties arising in the theoretical handling of double pion photoproduction. Although very close to the Valencia model -the main differences are the inclusion of more higher lying resonances ( $S_{11}(1535)$ ,  $S_{31}(1620)$ ,  $D_{15}(1570)$ ,  $F_{15}(1680)$  and  $P_{13}(1770)$ ) thought to play a small role in the second resonance region and a different spin structure of the  $D_{13} \rightarrow \pi \Delta$  transition- the prediction on the simplest

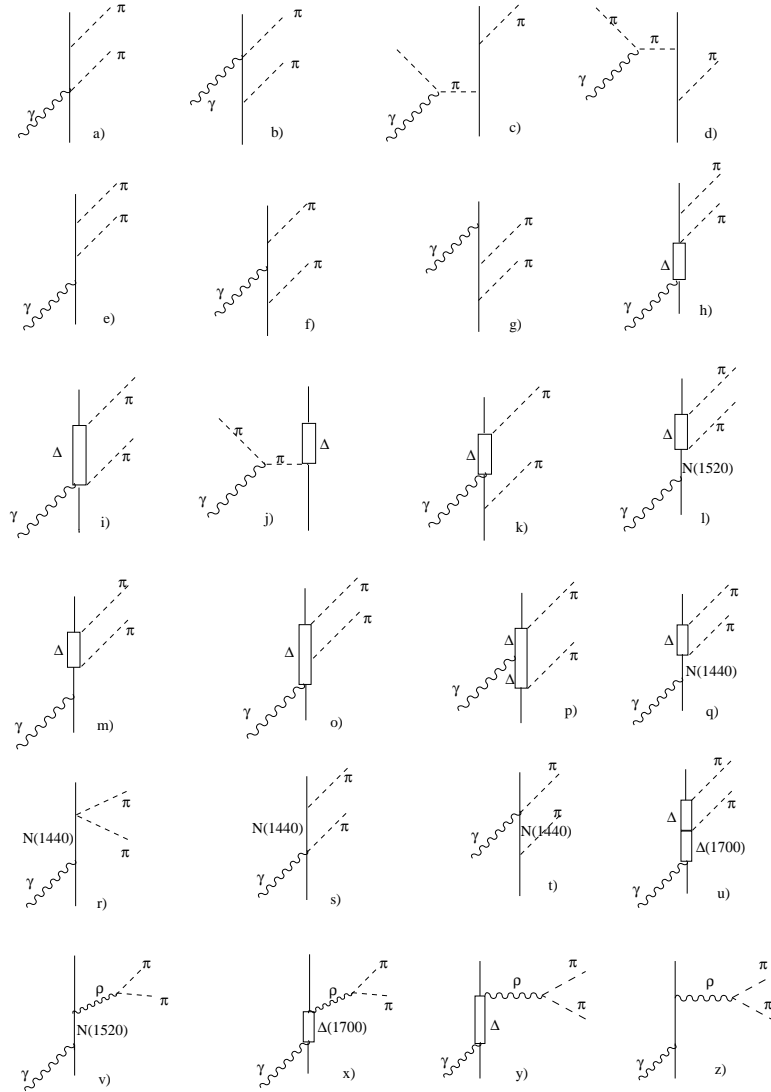


Figure 2.8: *Feynman diagrams used in the latest version of the Valencia model. For the double  $\pi^0$  reaction, only diagrams e-h, k-m, o-r and u contribute.*

observables such as total cross sections can vary up to 20% between both models.

In fig. 2.9, we show the Feynman diagrams used to build this model and in figures 2.10 to 2.12 the cross sections of the three isospin channels predicted by this model with individual contributions of the most important processes. These pictures illustrate the three main features of the latest models: In the second resonance region, the main resonant contribution to the cross section is due to the  $D_{13}$  resonance. Secondly, the total cross section is dominated by resonance decays for the  $\gamma p \rightarrow p \pi^0 \pi^0$  channel and by background terms for the two channels with charged pions. Finally, these plots show the difficulties of these models to

### 2.3. THEORETICAL MODELS FOR THE DOUBLE PION PHOTOPRODUCTION 27

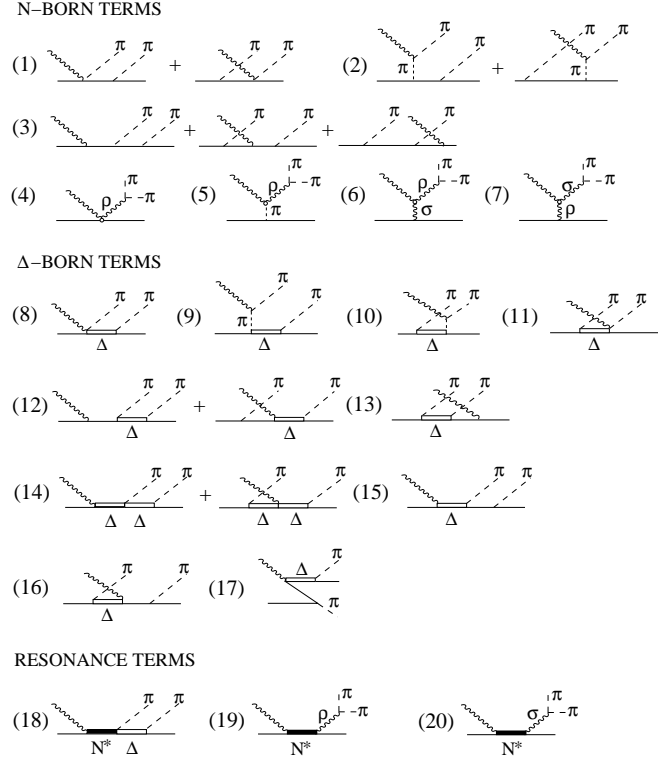


Figure 2.9: *Feynman diagrams used in the Mainz model. For the double  $\pi^0$  reaction, only diagrams 3, 12-18 and 20 contribute.*

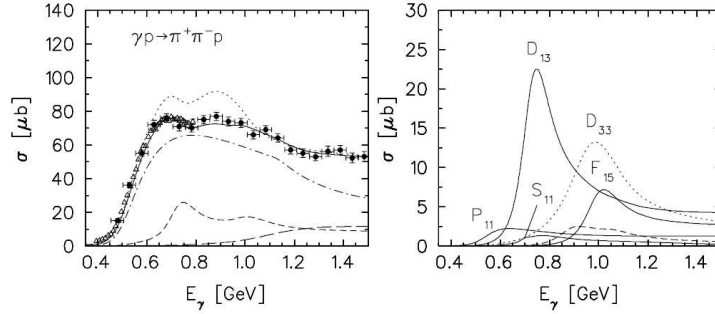


Figure 2.10: *Total cross section for the  $\gamma p \rightarrow \pi^+ \pi^- p$  reaction. Left: Black: total cross section. Dash-dotted:  $\Delta$  Kroll-Rudermann and pion pole terms (8) and (9) from fig. 2.9. Short-dashed: all resonances. Long dashed: diagrams (5) and (6). Dotted: total with inclusion of the  $D_{33}(1700)$ . Right: Individual contributions of the resonances. [Fix05] and subsequent references for the data points.*

provide a very accurate reproduction of the experimental data. On this account, a more thorough theoretical investigation on double pion photoproduction will have to be performed.

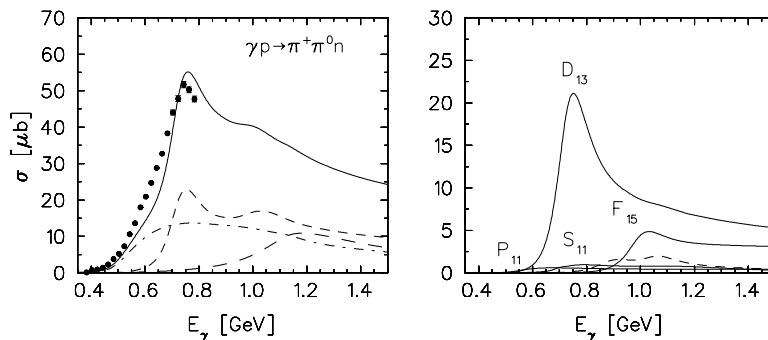


Figure 2.11: Total cross section for the  $\gamma p \rightarrow n\pi^+\pi^0$  reaction. Long-Dashed: diagrams (4) and (5).

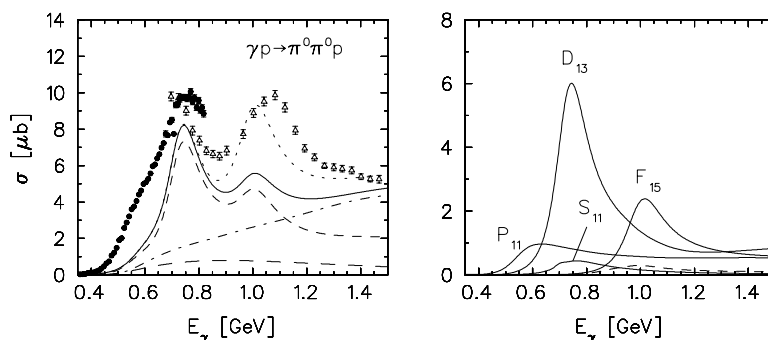


Figure 2.12: Total cross section for the  $\gamma p \rightarrow p\pi^0\pi^0$  reaction. Dash-dotted: diagram (12). Long-dashed: diagram (17). Dotted: Alternative sum with opposite sign of the  $F_{15}(1680) \rightarrow \pi\Delta$  amplitude.

### 2.3.4 Hiroshima model

The first version of the Hiroshima model was published by K. Ochi, M. Hirata and T. Takaki in 1997 [Och97]. This model is simpler than the ones presented so far. Here, a dynamical approach is used in which vertex functions are created and modified by form factors of the involved intermediate mesons and resonances. This model was the first to stress out the importance of the  $D_{13} \rightarrow \rho N$  decay and the  $\rho$ -Kroll-Rudermann term. (see e.g. diagrams v and z in fig. 2.8) in the  $\gamma p \rightarrow n\pi^+\pi^0$  reaction. At the time, this model was the first to give a reasonable description of the  $\gamma p \rightarrow n\pi^+\pi^0$  cross section though failing to describe the  $\gamma p \rightarrow p\pi^0\pi^0$  reaction.

More recently, a new version of this model [Hir03] proposed to replace the pseudovector nature of the  $\pi N$  coupling that is commonly used by a pseudoscalar coupling. With this assumption, they didn't need to introduce the  $\rho$  Kroll-Rudermann diagram any more and achieved calculations of the cross sections for all three isospin channels reproducing the data with a good accuracy. Once again, the strong model dependence of the predictions calls for a more stringent theoretical description of the double pion photoproduction channel.

## 2.4 Bonn-Gatchina partial wave analysis

The Bonn-Gatchina partial wave analysis attacks the problem by the other end. As an opposite to the models presented in the last section which try to use as few experimental input as possible, this approach uses the data of many experiments, fits them and uses the results of the fits to extract information on the resonances. In two very recent articles, a broad survey of resonances from the second and third resonance regions [Tho08] with a special focus on the Roper resonance [Sar08] has been performed with this method. In these two articles, newly published data on  $\gamma p \rightarrow p\pi^0\pi^0$  from the CB-ELSA collaboration as well as  $\gamma p \rightarrow p\pi^0$ ,  $\gamma p \rightarrow p\eta$ ,  $\gamma p \rightarrow K\Lambda$ ,  $\gamma p \rightarrow K\Sigma$  and older  $\gamma p \rightarrow p\pi^0\pi^0$  data were fitted and the individual contribution of the resonances were extracted. Altogether, the good quality of the fits allows a precise determination of the parameters of the ten lowest lying resonances. As an illustration related to our work, they found a value of  $0.212 \pm 0.030$  for the  $P_{11}(1440) \rightarrow p(\pi^0\pi^0)_{S\text{-wave}}^{I=0}$  decay branching ratio whereas [PDG06] gives only 5-10%.

In this work, we will only mention the results of this partial wave analysis for the double  $\pi^0$  channel. Fig. 2.13 shows the experimental cross section for this reaction as well as the result of the fit and the individual contribution of the  $D_{13}(1520)$ ,  $P_{11}(1440)$  and  $D_{33}(1700)$  resonances.

The main new feature of this result is the role of the  $D_{33}(1700)$  resonance. As an opposite to the Valencia and Mainz models which predict a negligible contribution of this resonance in the second resonance region, the  $D_{33}(1700)$  gives here the main contribution to the total cross section. As a consequence, the  $D_{13}(1520)$  which accounts for about 80% of the resonant contribution to the double  $\pi^0$  channel in fig 2.12 is only responsible here for less than one half of the total cross section. (Let's note that in this model, the second resonance bump is explained by the interference between the  $D_{33}(1700)$  and  $D_{13}(1520)$  which is constructive at 1500 MeV and destructive at 1600 MeV.)

As already mentioned many times, the discrepancy between the interpretation of the different models calls for a more thorough theoretical treatment of the double pion photoproduction. In that sense, the high precision data presented in this work, and especially the new polarization observables, will add further constraints to such fits and thus allow a more precise determination of the resonance properties.

## 2.5 Polarization observables

All the results presented so far have been performed using unpolarized particles. In the recent years, much effort has been put on the measurement of polariza-

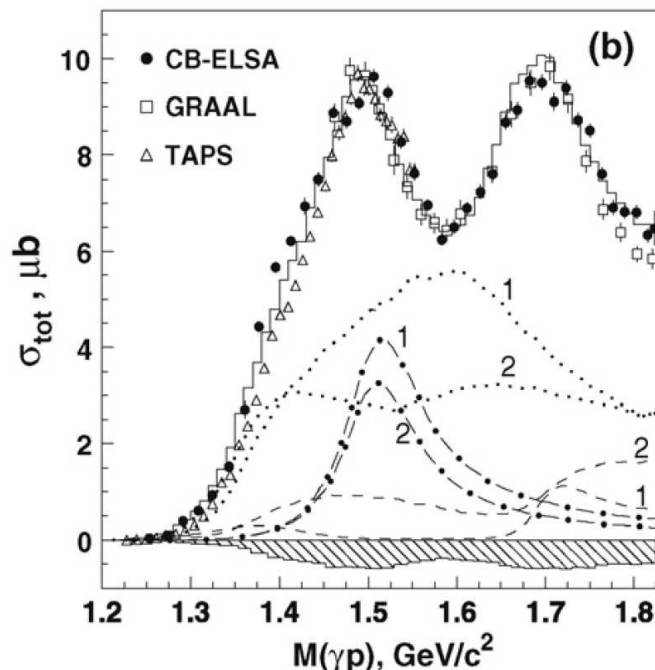


Figure 2.13: *Total cross section for the  $\gamma p \rightarrow p\pi^0\pi^0$  reaction. Solid: Partial wave analysis fit. Dotted: Contribution from the  $D_{33}(1700)$ . Dash-dotted:  $D_{13}(1520)$ . Dashed:  $P_{11}(1440)$ . Two sets of solutions are represented: (1)  $D_{33}(1700) \rightarrow \Delta\pi$  via  $S$ -wave. (2)  $D_{33}(1700) \rightarrow \Delta\pi$  via  $D$ -wave. The shaded area represents the systematic error of the CB-ELSA data. (Taken from [Sar08]).*

tion observables. As we shall see in the example of the angular distribution of the asymmetry, polarization observables are very sensitive to small changes in internal details of the models, making them a very precious tool for the individual study of resonances. A precise determination of polarization observables will add very stringent constraints to the models, giving a much clearer view of the underlying processes present in double pion photoproduction.

Experiments involving polarized photons or polarized targets are tricky to carry out (see section 3.2) and are only available since a few years. For this reason, not much results in this field have been published yet. A measurement of the  $\sigma_{\frac{1}{2}}$  and  $\sigma_{\frac{3}{2}}$  cross sections<sup>6</sup> for the double  $\pi^0$  channel was performed in the context of the GDH sum rule experiments in Mainz. (See [Ahr05]). Beam asymmetries have also been measured at GRAAL [Ass05].

In the past years, angular distributions of the beam helicity asymmetry has received much attention. It was measured for the first time by the CLAS collaboration at CEBAF [Str05] for the  $\gamma p \rightarrow p\pi^+\pi^-$  reaction. This measurement was

<sup>6</sup> $\sigma_{\frac{1}{2}}/\sigma_{\frac{3}{2}}$  is the total cross section for left/right handed circularly polarized photons on a longitudinally polarized proton target.

repeated in this work (in parallel with [Kra07]) and extended to the  $\gamma p \rightarrow p\pi^0\pi^0$  and  $\gamma p \rightarrow n\pi^+\pi^0$  channels. Moreover, all three isospin channels have also been investigated here with linearly polarized photons and linear asymmetries distributions have been produced. See next section for a detailed account of the important features of these observables.

In the coming years, there are prospects to perform double polarization experiments for the double  $\pi^0$  channel at ELSA and MAMI (see e.g. [Tho05]). More details are given in the outlook in chapter 8.

### 2.5.1 Asymmetries

In the most general case, three different polarizations have to be considered when dealing with meson photoproduction. The incoming photon (circularly or linearly) and the target nucleon can be polarized. In the case of the nucleon, two polarizations have to be taken into account: the polarization before (target polarization) and after interaction (recoil polarization). Experimentally, depending on the number of polarizations observed, single, double and triple polarization experiments can be performed. A theoretical description of the general triple polarization case, involving 64 polarization observables and very long formulas, has been given by W. Roberts and T. Oed [Rob05].

Here, we will restrict our description to the conditions experimentally available at MAMI during our experiment. Namely, a single polarization experiment in which linearly or circularly polarized photons impinged on an unpolarized target. In this case, the cross section for double pion photoproduction is given by

$$\frac{d\sigma}{dx_i} = \left(\frac{d\sigma}{dx_i}\right)_{unpolarized} (1 + P_\gamma^{circ} I^\odot - P_\gamma^{lin} (I^S \sin 2\varphi + \Sigma \cos 2\varphi)) \quad (2.2)$$

where  $P_\gamma^{circ}$  and  $P_\gamma^{lin}$  represent the degrees of circular and linear polarization,  $\varphi$  the direction of the linear polarization vector and  $I^\odot$ ,  $I^S$  and  $\Sigma$  the linear and circular asymmetry observables that are to be measured in this work.

In double pion production, the information provided by this kind of experiments is much richer than in the single pion case. In single meson production, the corresponding polarized cross section is given by

$$\frac{d\sigma}{dx_i} = \left(\frac{d\sigma}{dx_i}\right)_{unpolarized} (1 - P_\gamma^{lin} \Sigma \cos 2\varphi). \quad (2.3)$$

This expression is much simpler than for the double pion channel and only the polarization observable  $\Sigma$  can be determined that way. The reason for this lies in the fact that, in single meson photoproduction, the whole reaction can be put in a single plane containing the incoming photon, the recoil nucleon and the produced meson. This is not the case any more in double pion production. Here, two planes have to be defined to describe the reaction (see fig. 2.14). This makes the reaction richer and additional polarization observables occur ( $I^\odot$ ,  $I^S$ ).

A very convenient way to extract the physics contained in eq. 2.3 is to look at the difference between the cross sections for each of the two polarization states of the incoming photon. For this, we define the asymmetry as

$$A(\sqrt{s}, \phi) = \frac{d\sigma^+/d\phi - d\sigma^-/d\phi}{d\sigma^+/d\phi + d\sigma^-/d\phi} \quad (2.4)$$

where  $d\sigma^{+/-}/d\phi$  is the differential cross section for right/left handed photons (circular polarization) or parallel/perpendicular photons (linear polarization). In section 6.2, we will see how this definition gets simplified when adapted to our experimental conditions. The relevant kinematical and angular definitions are shown in fig. 2.14

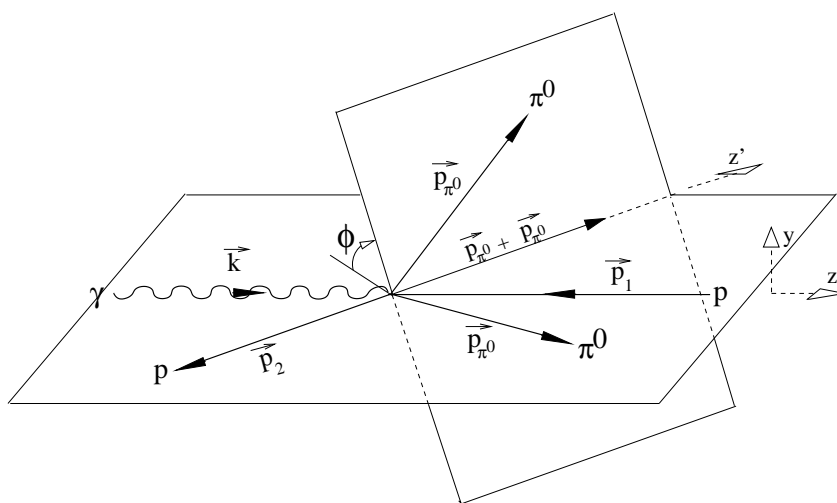


Figure 2.14: *Definitions of the angles, vectors and axis frame used to determine the asymmetry for double pion photoproduction.*

The  $\phi$  angle is defined as the angle between the reaction plane (the plane containing the incoming photon and the recoil nucleon) and the plane containing the two pions. Fig. 2.14 also fixes the axis frame used in this work. For this work, the so-called *helicity frame* has been used, in agreement with most of the recent articles on the subject<sup>7</sup>. Technically, the  $\phi$  angle can be uniquely determined with the following relations.

$$\cos \phi = \frac{(\vec{k} \times \vec{q}) \cdot (\vec{q} \times \vec{p}_{\pi_1^0})}{|\vec{k} \times \vec{q}| |\vec{q} \times \vec{p}_{\pi_1^0}|} \quad \sin \phi = -\frac{((\vec{k} \times \vec{q}) \times \vec{q}) \cdot (\vec{q} \times \vec{p}_{\pi_1^0})}{|(\vec{k} \times \vec{q}) \times \vec{q}| |\vec{q} \times \vec{p}_{\pi_1^0}|} \quad (2.5)$$

In the recent years, polarization has been introduced in the Valencia model [Nac02], [Roc05] and predictions for the asymmetry were calculated. Polarization

<sup>7</sup>This choice is arbitrary and in the past, other frames differing in the direction of  $z'$  have been commonly used.

is also included in the Mainz model. It is briefly mentioned in [Fix05] and is currently under development [FixWWW]. These models calculate the asymmetries for all three isospin channels of double pion photoproduction as a function of the incoming photon energy. Some relevant results will be compared with our data in section 7.3

The inclusion of polarization in the models is quite straightforward, but it turns out that the predicted asymmetries are very sensitive to small internal details of the models. In order to illustrate this and show the benefits provided by a survey of the asymmetry to our understanding of the resonances, fig. 2.15 shows the  $\phi$  distribution of the helicity asymmetry for the  $\gamma p \rightarrow p\pi^0\pi^0$  reaction for 730 MeV photons.

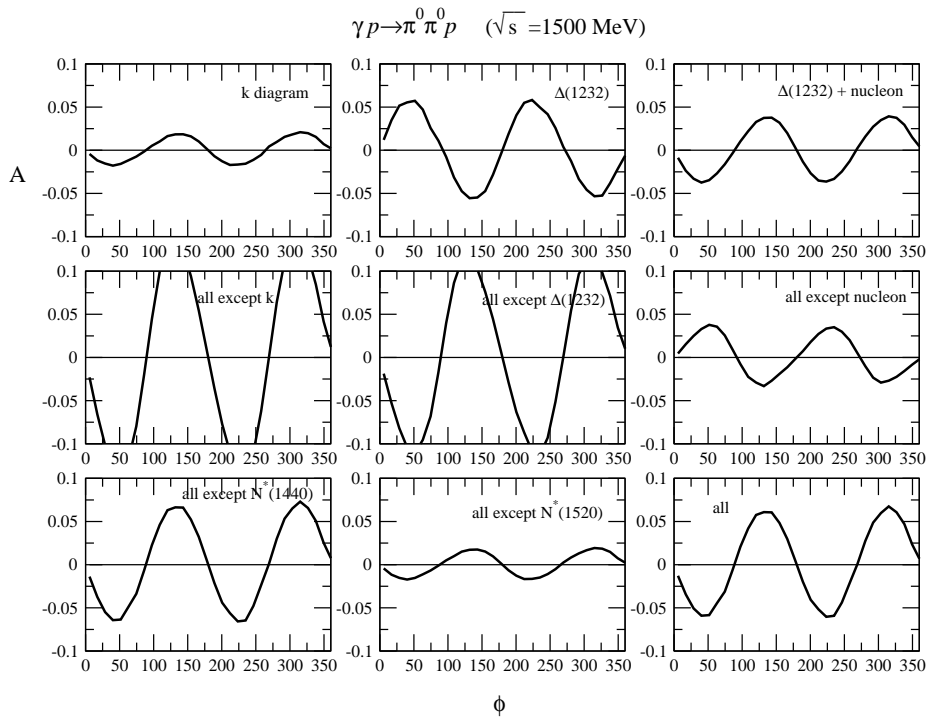


Figure 2.15: Angular distribution of the helicity asymmetry in the  $\gamma p \rightarrow p\pi^0\pi^0$  channel for different diagrams with an incoming photon energy of 730 MeV.

The bottom right plot shows the total asymmetry for which all diagrams from fig. 2.8 are taken in account, while the other ones show the contributions of individual or group of mechanisms. As an example of the very high sensitivity of this observable, the removal of a single resonance, the  $D_{13}(1520)$  (bottom middle) reduces the asymmetry by a factor 3. Alternatively, the removal of a single  $\Delta$ -Born term (middle left) dramatically enhances the asymmetry.

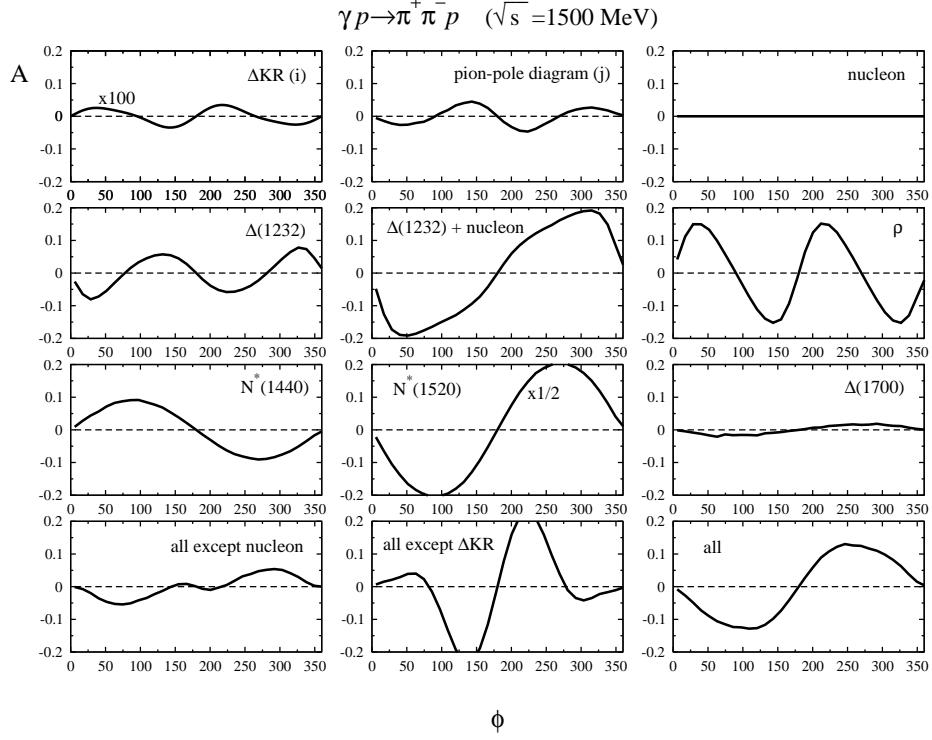


Figure 2.16: Angular distribution of the helicity asymmetry in the  $\gamma p \rightarrow p\pi^+\pi^-$  channel for different diagrams with an incoming photon energy of  $730$  MeV. ( $\sqrt{s} = 1500$  MeV)

Even more striking is the variety of shapes for the  $\gamma p \rightarrow p\pi^+\pi^-$  reaction presented in fig. 2.16. In the double  $\pi^0$  channel, the fact that both  $\pi^0$  are undistinguishable imposes the condition  $A(\phi) = A(\phi + \pi)$ . This is not the case for the  $\pi^+\pi^-p$  channel. Here, the behaviour of the  $\Delta$ -Kroll-Rudermann term is very explicit. Even though it adds only a tiny contribution by itself (top left), it completely changes the shape of the total asymmetry when removed (bottom middle). Those remarks are only here to give some flavour of the very high sensitivity of the asymmetry to small details of the models. As we shall see more clearly in section 7.3, a much clearer understanding of the behaviour of resonances and of their couplings to the double pion channel in the second resonance region will eventually be achieved with a fit of our data to such models.

## 2.6 Double pion photoproduction at threshold

Another crucial feature of the  $\gamma p \rightarrow p\pi^0\pi^0$  reaction is the description of the cross section close to threshold ( $E_\gamma^{thresh} = 308.8$  MeV). This cross section is calculated in the framework of chiral perturbation theory (ChPT), more precisely in its extension to the nucleon sector (Heavy Baryon ChPT). As we will show, ChPT makes unexpected predictions for the cross section of this channel at threshold. A precise measurement will therefore provide a crucial test for chiral perturbation theory. In the following, the physical arguments used to derive the double  $\pi^0$  cross section will be presented in a qualitative way. The complete calculations have been performed by V. Bernard and co-workers in [Ber96]. Background information on ChPT can be found e.g. in [Sch03].

In QCD, the Lagrangian density owns a symmetry, the *chiral symmetry*, in the limit of vanishing quark masses. This symmetry is not perfect since the quark masses are not exactly zero<sup>8</sup>. Yet, the quark masses are very small compared to the typical nucleon masses. ChPT takes advantage from this and treats the quark masses in a perturbative way. Hence, it is constructed as an expansion of the QCD Lagrangian density in terms of momenta and masses of physical particles with small masses compared to the nucleon mass scale (power counting).

In our case, the method used in [Ber96] consists in an expansion in terms of the pion mass up to the order  $\mathcal{O}(M_\pi^2)$ . In practice, all Feynman diagrams up to this order have to be systematically constructed and included in the expansion. When doing this, it turns out that the role of pion loops (fig. 2.17) is crucial. In the case of single pion photoproduction, such loops only add a small contribution to the cross section close to threshold. This is also the case in double pion photoproduction for the  $\pi^+\pi^-p$  and  $\pi^+\pi^0n$  channels. On the contrary, for the double  $\pi^0$  production, pion loops not only add a significative contribution to the cross section, but are the dominant process. As a consequence, we have

$$\sigma^{thresh}(\pi^0\pi^0) > \sigma^{thresh}(\pi^+\pi^-) \quad \text{or} \quad \sigma^{thresh}(\pi^+\pi^0). \quad (2.6)$$

This came as a surprise since, at higher energies, the double  $\pi^0$  cross section is lower than the charged pions channels due to the smaller number of allowed production mechanisms (see section 2.3). As a consequence, the precise determination of the  $\gamma p \rightarrow p\pi^0\pi^0$  cross section close to threshold is an ideal tool to investigate the pion loop mechanism and provides thus a crucial test for chiral

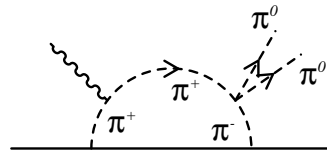


Figure 2.17: *Feynman diagram of a pion loop. This mechanism plays a crucial role in the description of the double  $\pi^0$  cross section close to threshold.*

<sup>8</sup>Let's note that in addition to this small *explicit* breaking of symmetry, a *spontaneous* breaking is also present: the ground state corresponding to QCD vacuum doesn't have the symmetry of the Lagrangian.

perturbation theory. In [Ber96], the cross section close to threshold is given by

$$\sigma_{tot}(E_\gamma) = 0.63 \left( \frac{E_\gamma - E_\gamma^{thresh}}{10 \text{ MeV}} \right)^2 \text{ nb.} \quad (2.7)$$

Due to the uncertainty in the coupling of the  $P_{11}(1440)$  to the double  $\pi^0$  channel, this cross section is not precisely determined and eq. 2.7 only represents the average value of the model. An upper limit is obtained when increasing the factor from 0.63 to 0.91. Due to the intrinsic nature of ChPT, this calculation is only valid at energies close to threshold:  $E_\gamma^{thresh} = 308.8$  to  $\sim 350$  MeV.

This cross section has been measured at MAMI. [Wol00] and [Kot03]. The results are compatible with eq. 2.7 but with large error bars. In this work, we have repeated this measurement with a very large improvement in the statistical quality of the data. The results are presented in section 7.1.1.

## 2.7 Some words on the magnetic moment of the $\Delta^+(1232)$ resonance

To conclude this chapter in a recreative way, we will say some words about the magnetic moment of the  $\Delta^+(1232)$  resonance. This subject is only loosely related to our field since it doesn't imply double pion final states nor even resonances from the second energy region. For this reason, the hurried reader can skip this section and go directly to chapter 3. Experimentally however, the determination of this magnetic moment had some influence on our work. Since the experimental conditions required to perform this experiment were similar to the ones needed for double pion production (free proton target, similar number of particles in final states), it was decided that both experiments could be run in parallel. This choice was done to optimize time and manpower. On the experimental side, a few concessions had to be done. In chapter 3 and 4, some settings in the setup will appear not to completely suit our needs for a perfect survey of the double pion channels. The main reason for this is that these settings were optimized for the  $\Delta$  magnetic moment measurement. The short summary presented here will help understanding these choices.

The anomalous magnetic moment of baryons is an historically important observable. When measured for the proton and the neutron, it gave the first hint for a possible internal structure of the nucleon. For the  $\Delta^+(1232)$  resonance, a determination of the magnetic moment using the standard spin precession technique is not possible due to its very short lifetime. An alternative way to measure it was proposed by A. Konratyuk and L. A. Ponomarev [Kon68] and is sketched in fig. 2.18. A  $\Delta$  resonance is first produced by a photon. It then emits a photon

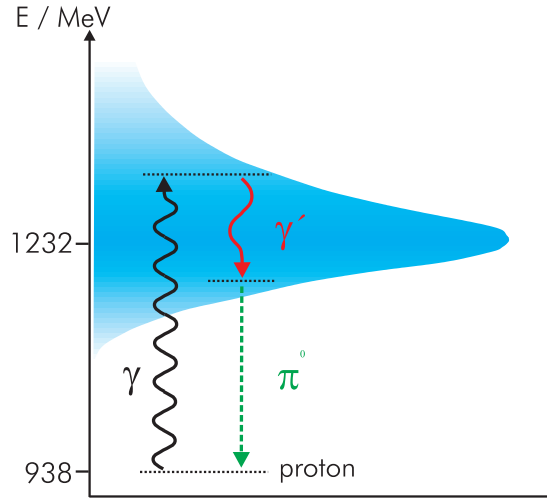


Figure 2.18: The reaction  $\gamma p \rightarrow \Delta \rightarrow \gamma' \Delta^+ \rightarrow \pi^0 \gamma' \Delta^+$  used to determine the magnetic moment of the  $\Delta^+$  resonance.

$\gamma'$  within its own width before decaying back to the proton ground state via the emission of a  $\pi^0$ . The amplitude of this process is directly proportional to  $\mu_{\Delta^+}$ . Though quite simple in its principle, this reaction is tricky to measure. First, a lot of background terms due to bremsstrahlung give  $\pi^0 \gamma' p$  final states. Altogether, they are responsible for more than one half of the total  $\gamma p \rightarrow \pi^0 \gamma' p$  cross section. Recent models such as [Dre01] include a large number of background processes to make predictions for the  $\gamma p \rightarrow \pi^0 \gamma' p$  cross section which can then be used to deduce the value of  $\mu_{\Delta^+}$ . A second difficulty of this channel is the very small cross section of this reaction (a few nb) compared to sources of experimental background such as  $\gamma p \rightarrow p \pi^0 \pi^0$  where one of the four final state photons gets lost. For these reasons,  $\mu_{\Delta^+}$  is not known with a great accuracy. A first experiment performed at MAMI in 1999 [Kot02] gave  $\mu_{\Delta^+} = (2.7^{+1.0}_{-1.3} \pm 1.5_{stat}) \mu_N$ . This experiment was repeated in parallel with our work during the 2004/2005 round of experiments. The  $4\pi$  detector used here is the ideal tool to gather a lot of statistics with a reduced experimental background. Moreover, the use of polarized photons allows the determination of asymmetries which have been predicted to be highly sensitive to the magnetic moment. (This point is responsible for the main drawback in running both experiments in parallel: the linearly polarized photon peak was set between 390 and 440 MeV (see section 3.2) corresponding to the maximum of the  $\gamma p \rightarrow \pi^0 \gamma' p$  cross section. As discussed in section 7.4, this energy is much too low to allow a good determination of the linear asymmetry in the double  $\pi^0$  channel.) This difficult analysis is currently under way [Boi08], [Sch07], [Dow07] and will require much effort to produce accurate results. As an example of this ongoing analysis, fig. 2.19 shows the angular differential cross section for this reaction for photons between 375 and 425 MeV. The angle theta is defined as the angle of the radiative photon  $\gamma'$  in the c.m. frame. This picture

is only shown here to illustrate the difference in the statistical quality of the data between [Kot02] and this new measurement that will eventually lead to a precise determination of  $\mu_{\Delta^+}$ . Further information on the physics behind this picture and the  $\Delta$  magnetic moment in general can be found in [Boi08].

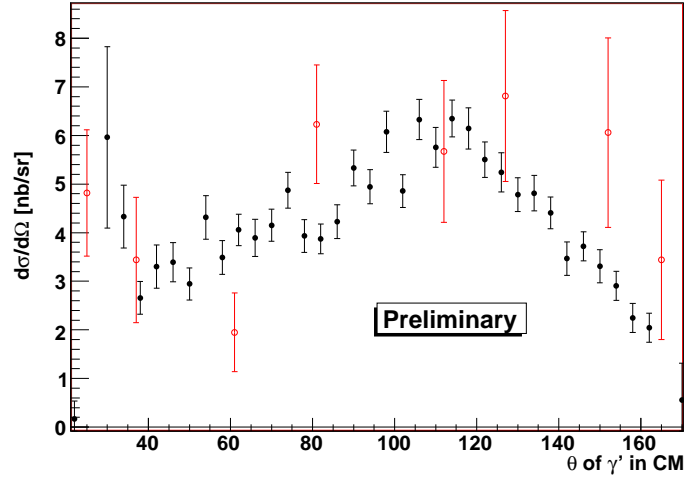


Figure 2.19: *Sample plot from the analysis of the  $\gamma p \rightarrow \pi^0 \gamma' p$  reaction: cross section as a function of  $\theta_{\gamma'}$ . Red: Previous work [Kot02]. Black: Analysis performed with the same data as this work [Boi08].*

Let's finally note that the same principle can be used to measure the magnetic moment of the  $S_{11}(1535)$  resonance using the  $\gamma p \rightarrow \eta \gamma' p$  reaction. This measurement is currently under way at MAMI C.

## 3 Experimental setup

*In the previous chapter, we have given an account of the models describing double pion photoproduction and of the main challenges associated with their study. The main body of this work, presented in the next three chapters, consists in the production of pion pair events, their detection and the reconstruction of the associated observables used to test the models. We start in this chapter with an overview of the data taking. We will first show how a nice beam of polarized tagged photons is produced using the MAMI accelerator, the Glasgow tagger and a thin diamond radiator. We will then briefly describe how the central point of our experiment, the liquid hydrogen target is constructed. We will then present the detectors used to observe the decay products of the reaction: the Crystal Ball, TAPS and their subsystems. In the end of this chapter, we will have a look at how the output signals of the detectors are put in a convenient way in a description of the electronics. Finally, we will show how the trigger gets rid of the bad events online.*

### 3.1 MAMI, the electron accelerator

The electron accelerator MAMI (MAInzer MIkrotron) [Jan05] project was initiated in the 70s to fulfill the need for continuous wave electron beams and is used in its present configuration since 1990 under the name of MAMI B. Over the years, it has proven itself to be an essential tool to produce very accurate results in a wide range of physics. MAMI consists of three cascade RTMs (RaceTrack Microtrons) accelerating electrons up to 14 MeV, 180 MeV and 883 MeV at each respective stage. The electrons from a polarized electron source [Aul97] are initially accelerated and injected into the first RTM by a 3.5 MeV linear accelerator (see the bottom left part of fig 3.1).

The principle of a racetrack microtron is sketched in fig. 3.2. It consists of a single linear accelerator (In MAMI, a 2.5 GHz radiofrequency non-superconducting linac) completed by a bending magnet at each of its ends. The magnetic fields provided by these magnets let the beam being recirculated in the linac a great

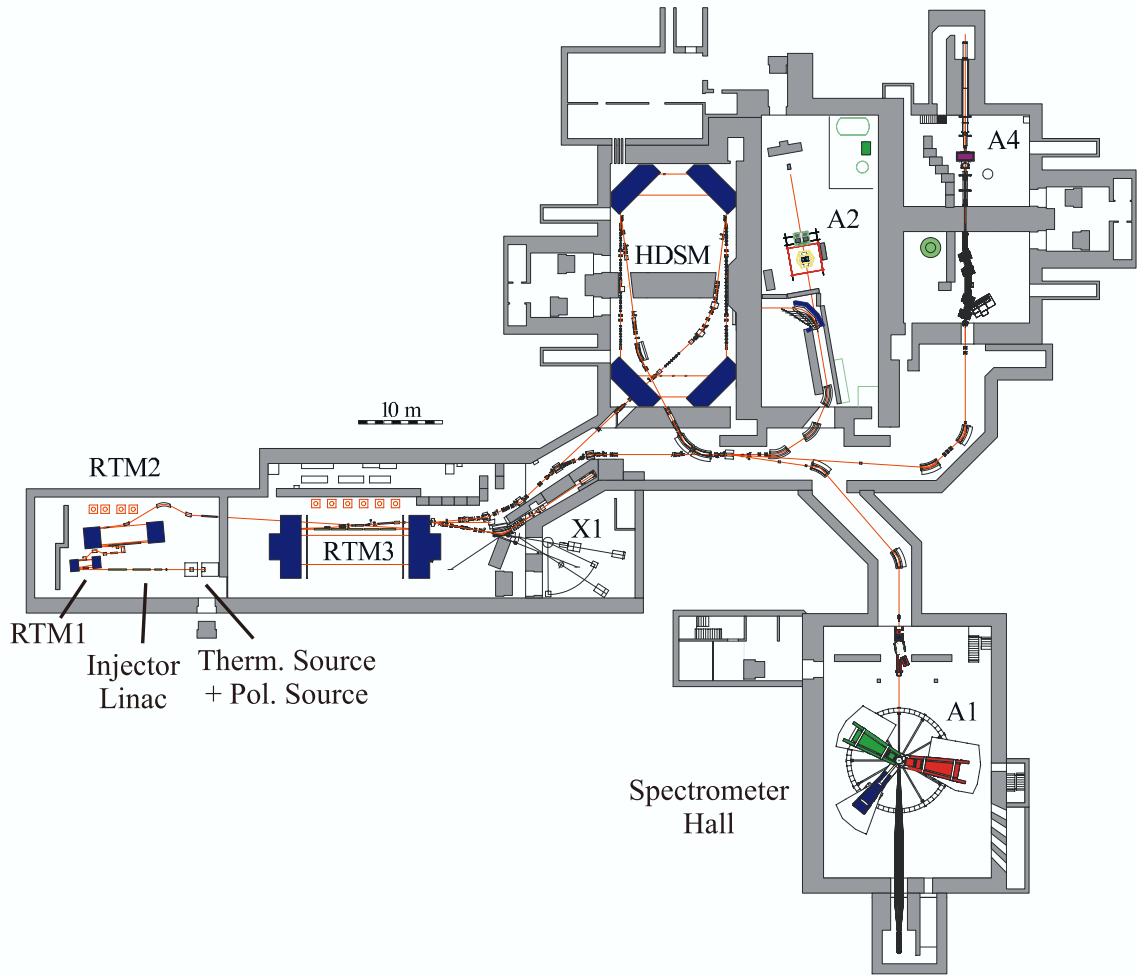


Figure 3.1: *Floorplan of MAMI. The three cascaded RTMs can be seen on the left. The A2 hall, where this work was performed, the A1, A4 and X1 and the HDSM of MAMI C<sup>2</sup> have also been represented*

number of times, increasing the energy of the beam and thus augmenting the radius of the trajectory with each loop. When the beam has reached the desired energy, it is extracted with a small bending magnet. One of the most valuable features of the microtron is the inherent phase correction which keeps the energy spread to a very small value, around 60 KeV.

The other important property of the accelerator is the duty factor of 100%. This ensures the delivering of a continuous, high intensity beam. This is essential to accurately perform random background subtraction and therefore precisely determine cross sections as presented in section 6.1.

Altogether, MAMI provides an excellent quality beam with small emittance and high stability for beam currents up to  $80 \mu\text{A}$ . In our experiment, the beam energy was measured to be  $883 \pm 0.16 \text{ MeV}$  and the current kept at  $\sim 10 \text{ nA}$  not to go

beyond the maximal counting rate in the Tagger.

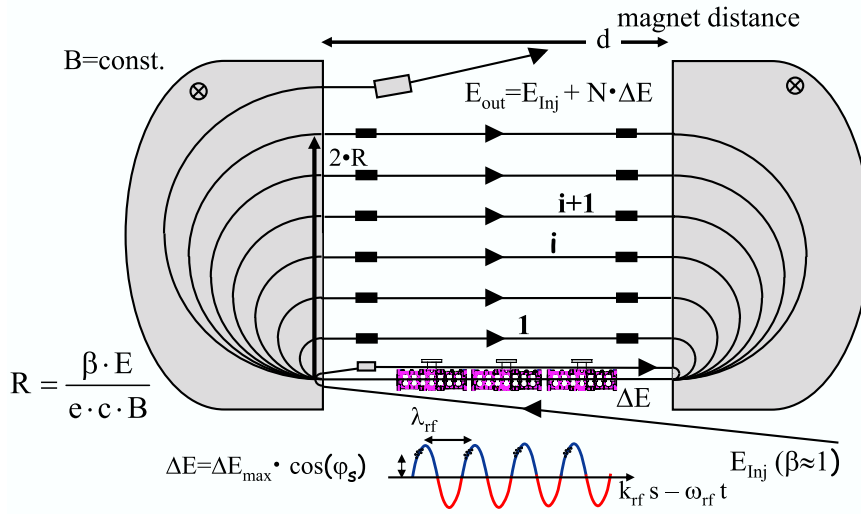


Figure 3.2: *Design of a racetrack microtron. With every loop, an energy  $\Delta E$  (related to the phase of the oscillation in the cavity, in our case  $\Delta E \approx 7.5 \text{ MeV}$ ) is added to the beam energy, increasing the radius of the trajectory.*

## 3.2 Polarized photon production

High energy photons were obtained from the MAMI accelerated electrons via bremsstrahlung on a thin radiator foil which is a popular technique<sup>3</sup> also used at ELSA<sup>4</sup> and CEBAF<sup>5</sup>. In this method, sketched in fig. 3.7, real photons are obtained by sending electrons on a  $100 \mu\text{m}$  diamond foil. In the medium, the electrons might be accelerated by the nucleus' electrical field thus emitting a bremsstrahlung photon which, if emitted in the forward direction, will eventually reach the target. The scattered electron, deprived of a fraction of its energy will see its trajectory bent by the tagger magnetic field onto the the focal plane detector where its energy will be measured (see section 3.3).

Due to the large mass of the nucleon compared to the electron's, the energy transfer to the nucleus can be neglected and the energy of the bremsstrahlung photon

<sup>2</sup>In order to increase the beam energy up to 1.5 GeV, an HDSM (Harmonic Double Sided Microtron) has been added to the cascade of accelerators. The whole system, usually referred to as MAMI C, has been developed over the past years and came recently online (spring 2007) for the first data taking

<sup>3</sup>The other common way to produce real photons is the Compton laser backscattering of laser light used e.g. at GRAAL in France, BNL in Brookhaven, USA and Spring8 in Japan

<sup>4</sup>ELSA: ELEktronen Stretcher Anlage in Bonn, Germany

<sup>5</sup>CEBAF: Continuous Electron Beam Accelerator Facility at JLab in Newport News, VA, USA

is determined by

$$E_\gamma = E_e - E_{e'} \quad (3.1)$$

where  $E_e$  and  $E_{e'}$  are the electron energy before and after the bremsstrahlung process respectively. In the simple, well known case of unpolarized photon production, the shape of the spectrum is a smooth  $1/E_\gamma$  shape and the angular distribution is given by

$$\frac{d\sigma}{dE_\gamma} \sim \frac{1}{E_\gamma} \quad \frac{d\sigma}{d\theta_\gamma} \sim \frac{\theta_\gamma}{(\theta_\gamma^2 + \theta_c^2)^2} \quad (3.2)$$

where  $\theta_c \sim \frac{1}{E_e}$  is the characteristic angle in which 50% of the photons are emitted.

### 3.2.1 Linearly polarized photons

In chapter 2, we have seen the many advantages of performing experiments with polarized photons. In this section, we will present how linearly and circularly polarized photons are produced at MAMI. Linearly polarized photons are obtained via coherent bremsstrahlung from a thin diamond radiator. When performed on a crystal radiator, the momentum transfer of the electron can either be done to an individual nucleus, in a usual incoherent bremsstrahlung process or on the crystal lattice, producing polarized photons, such as illustrated in fig 3.3. The resulting spectrum will then correspond to the sum of the two processes.

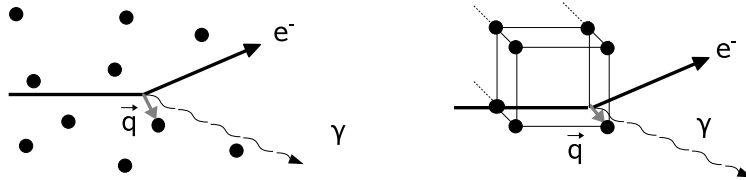


Figure 3.3: Left: *Incoherent bremsstrahlung*, the momentum is transferred to a single nucleon. Right: *Coherent Bremsstrahlung*, the momentum is transferred to the crystal lattice. (Adapted from [Sch01])

The treatment of coherent bremsstrahlung is somewhat tricky and will only be sketched here. More details can be found in [Nat03]. [Loh94] and [Ram98] provide detailed explanations on its use at MAMI.

The kinematics of bremsstrahlung are described by equation 3.1 and

$$\vec{p}_e = \vec{q} + \vec{p}_{e'} + \vec{p}_\gamma \quad (3.3)$$

where  $\vec{q}$  represents the momentum transfer to the nucleon. Taking advantage from the cylindrical symmetry of the system, it is customary to split  $\vec{q}$  into its

longitudinal  $q_l$  and transverse  $q_t$  components with respect to  $\vec{p}_e$ . The limits for  $q_l$  and  $q_t$  can be derived as

$$q_l^{max} \approx \frac{\delta}{x} \geq q_l \geq q_l^{min} = \delta + \frac{q_t}{2E_e} \quad 1 \gtrsim q_t \geq 0 \quad (3.4)$$

with

$$x = \frac{E_\gamma}{E_e} \quad \text{and} \quad \delta = \frac{1}{2E_e} \frac{x}{1-x} \quad (3.5)$$

These relations define an allowed kinematical region for the the momentum transfer usually referred to as the 'momentum pancake' due to the small extent of  $q_l$  with respect to  $q_t$ . This pancake is represented by the shaded areas in fig 3.4. The lower limit  $q_l^{min}$  is a sharp cut due to kinematics whereas the upper limit  $\delta/x$  is smoother, being due to the rapid decrease of the cross section with increasing  $q$ .

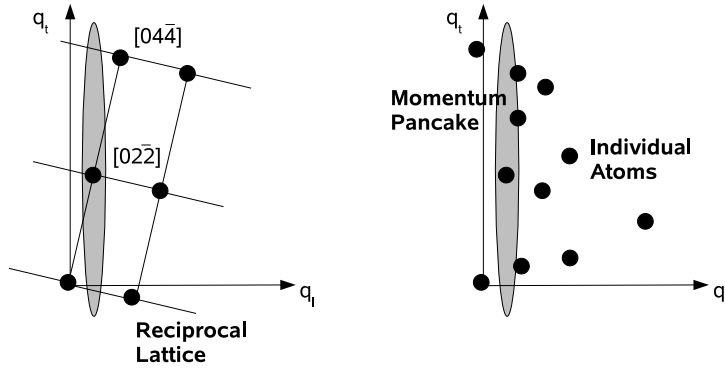


Figure 3.4: Left: *Reciprocal lattice vectors of the crystal diamond in the momentum space with the allowed kinematical region (momentum pancake). The crystal is oriented so that only the  $[02\bar{2}]$  vector can produce linearly polarized photons in the selected energy range.* Right: *Same for incoherent bremsstrahlung. The individual nuclei form a continuum in the momentum space leading to a smooth  $1/E_\gamma$  spectrum (adapted from [Loh94] and [Dow07]).*

Knowing this, we can describe the behaviour of the spectra for the incoherent and coherent bremsstrahlung. For the incoherent process, as illustrated in fig 3.4b, the momentum transfer is performed on the individual atoms of the crystal and can thus happen anywhere within the momentum pancake. An increase in  $x$ , or in other words the sweeping of the pancake through the momentum space, will lead to the usual, smooth  $1/E_\gamma$  spectrum. For incoherent bremsstrahlung, the situation is dramatically different. Here, the momentum is transferred to the lattice and  $\vec{q}$  has to be equal to one of the reciprocal lattice vectors.

$$\vec{q} = \vec{g} = \sum_{k=1}^3 h_k \vec{b}_k \quad (3.6)$$

where  $h_k$  are the Miller indices and  $\vec{b}_k$  the basis vectors of the reciprocal lattice. This is illustrated in fig 3.4a. The shape of the coherent bremsstrahlung spectrum is directly related to this discrete structure. When sweeping through the momentum space, the pancake will meet the different reciprocal lattice vectors. As soon as  $q_i^{max} = q_i^{[abc]}$  polarized photons will be produced on the reciprocal vector  $[abc]$ . The cross section will rapidly increase until  $q_i^{min} = q_i^{[abc]}$  is reached. At this point, the sharp kinematical limit will make the production drop sharply, creating a discontinuity which is referred to as the *coherent edge*. Fig. 3.5c shows the coherent contribution to the total bremsstrahlung spectrum. In our experiment, the crystal has been aligned to maximize production on the  $[02\bar{2}]$  reciprocal vector. An additional small contribution from the  $[04\bar{4}]$  can be seen at  $\sim 550$  MeV.

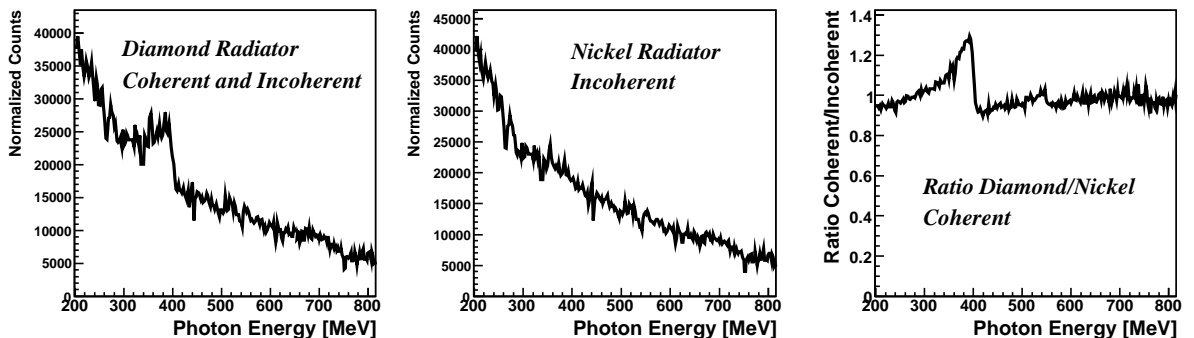


Figure 3.5: *Coherent and incoherent bremsstrahlung spectra for diamond and nickel radiators. The total diamond spectrum (left) shows a smooth  $1/E_\gamma$  incoherent part with an enhancement due to the coherent process. When divided by the incoherent Ni spectrum (center), one gets the contribution from coherent bremsstrahlung alone (right). The sharp edge at  $\sim 400$  MeV is due to the  $[02\bar{2}]$  reciprocal vector. A smaller  $[04\bar{4}]$  contribution can be seen at  $\sim 550$  MeV.*

The photons produced with coherent bremsstrahlung show a high degree of linear polarization. As explained with more details in [Nat03], the bremsstrahlung cross section calculated without summation over the photon polarization is given by

$$\frac{d\sigma}{dE_\gamma} \sim \frac{1}{E_\gamma} \cos^2 \xi \quad (3.7)$$

where  $\xi$  is the azimuthal angle of the polarization vector  $\vec{\epsilon}$  around  $\vec{p}_e$  with respect to the plane  $(\vec{p}_e, \vec{q})$ . In the case of coherent bremsstrahlung, we have seen in

eq. 3.6 that the momentum transfer  $\vec{q}$  is restricted to a set of discrete values corresponding to the reciprocal lattice vectors  $\vec{g}$ .  $\vec{q}$  being fixed, the photon polarization vector will tend to lie dominantly in a single plane, producing a photon beam with large polarization.

In our experiment, the polarized photons are obtained by performing coherent bremsstrahlung on a 100  $\mu\text{m}$  diamond radiator. The radiator is mounted on a 5-axis goniometer that allows a precise alignment of the crystal axis. The crystal was oriented as in fig 3.4a so that the  $[02\bar{2}]$  reciprocal vector was the only one contributing to the coherent bremsstrahlung process in the 300-450 MeV range. The coherent edge was set at  $E_\gamma = 400$  or 440 MeV depending on the data taking period. A precise alignment was obtained using an elaborate technique of energy scans known as the 'Stonehenge technique' [Liv05]. The goniometer was also used to periodically rotate the crystal by  $90^\circ$  in order to produce the same amount of data with parallel and perpendicular -in respect to the hall floor - polarized photons. Finally, it was possible to use the goniometer to move the radiator out of the beam line and to replace it by another radiator. In our experiment an amorphous 4  $\mu\text{m}$  nickel radiator was used to measure reference incoherent spectra (see fig 3.5b).

### Polarization degree

In the coherent bremsstrahlung process, not all the photons come out of the radiator with the desired linear polarization. In order to produce accurate asymmetries (see section 6.2) we will need a precise determination of the fraction of polarized photons. This is given by the polarization degree, which is defined as

$$P_\gamma = \frac{d\sigma^\perp - d\sigma^\parallel}{d\sigma^\perp + d\sigma^\parallel + d\sigma^{\text{incoherent}}} \quad (3.8)$$

where  $d\sigma^\perp$  and  $d\sigma^\parallel$  stand for the production of perpendicular and parallel orientations of the linearly polarized photons. As explained in [Sch01], the polarization degree can be related to the coherent and incoherent intensities  $I^{\text{coh}}$  and  $I^{\text{incoh}}$  as

$$P_\gamma(x, x(\text{edge})) \sim \frac{I^{\text{coh}}(x, x(\text{edge}))}{I^{\text{coh}}(x, x(\text{edge})) + I^{\text{incoh}}(x, x(\text{edge}))} \quad (3.9)$$

It is depending on the relative photon energy  $x$  and the position of the coherent edge. Using the method described in this reference, we could fit plots such as fig. 3.5c to get the polarization degree. Here, however, a more efficient method based on Monte-Carlo simulation was adopted. We used the ANB (ANalytic Bremsstrahlung) program described in [Nat03]. Using electron beam and radiator input parameters, this program simulates the coherent contribution to the

bremstrahlung cross section and uses it to determine the linear polarization degree. A typical result can be seen in fig. 3.6a. The calculations using ANB were carried out by E. Downie and more information can be found in her thesis [Dow07].

### 3.2.2 Circularly polarized photons

The physics to produce a beam of circularly polarized photons is much simpler than for the linear case. Here the accelerated electrons have to be spin polarized. Right and left handed photons are then simply obtained by helicity transfer during the bremsstrahlung process. Spin polarized electrons are obtained by exciting a semi-conductor cathode with a circularly polarized laser light. The orientation of the polarization is then selected by a Pockel cell [Aul97]. The difficulty resides here in the determination of the absolute orientation of the helicity. This was done by K. Aulenbacher and D. Krambrich using Mott-polarimetry<sup>6</sup>. More information on circularly polarized photons at MAMI can be found in D. Krambrich thesis [Kra07].

#### Polarization Degree

The polarization degree of circularly polarized photons obtained by helicity transfer of spin polarized electrons is given in terms of the relative photon energy  $x$  by the Olsen-Maximon function [Ols59]

$$P_\gamma = P_e \frac{4x - x^2}{4 - 4x + 3x^2} \quad (3.10)$$

where  $P_e$  is the electron polarization degree which was determined at  $(82 \pm 5)\%$ . This is represented in fig 3.6b.

### 3.2.3 Collimation

The photon beam, once produced by bremsstrahlung in the radiator has to go through one final step before reaching the target. The emission angle distribution of the photon beam (see eq. 3.2b) is already nicely forward peaked but a better resolution in the beam position is achieved with a further collimation of the beam before it reaches the target. With a 4 mm lead collimator placed 2.5 m downstream of the radiator, one ensures that the size of the beam spot on the target has a diameter of 1.7 cm, thus entirely contained within the target radius. An obvious consequence of this collimation is that not all produced photons will reach the target. In order to precisely calculate cross sections, the fraction

---

<sup>6</sup>For AcquRoot users, the Pockel cell readout (fADC[10]) is +1/-1 for a negative/positive electron helicity and therefore for a right/left handed photon. This behaviour is opposite for the January CP runs.

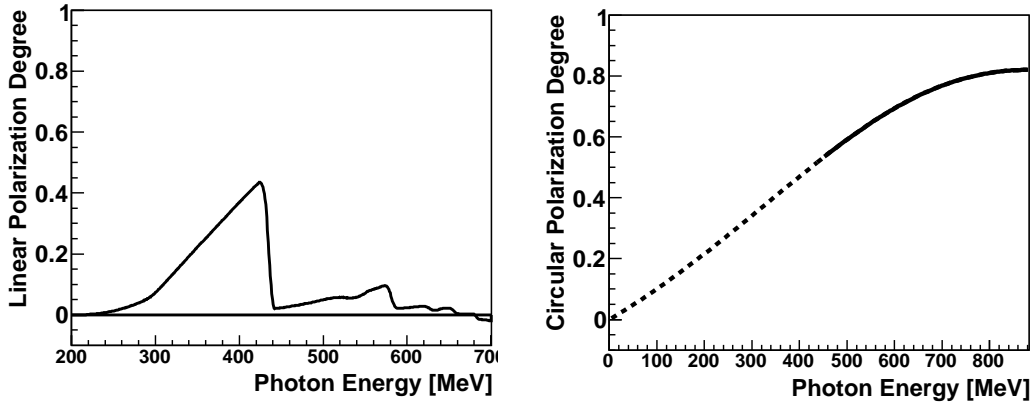


Figure 3.6: *Polarization degree for linearly (left) and circularly polarized photons (see text). In the energy range of the strongest linear polarization (300-450 MeV) the Olsen-Maximon function is not valid as a photon can't be simultaneously linearly and circularly polarized.*

of photons lost during collimation has to be precisely known. This is done in section 4.6 where tagging efficiency measurements are discussed in detail. As a bonus, it turns out that the angular distribution for linearly polarized photons is more forward peaked than for unpolarized photons. The collimation will therefore increase the proportion of linearly polarized photons in the total spectrum.

### 3.3 The tagger

The Glasgow photon tagger is a large magnet build in 1991 by the University of Glasgow [Ant91] to be used with the newly available 850 MeV electrons provided by MAMI B. Its two main roles are the determination of the energy of the electron scattered in the bremsstrahlung process which is used to determine the photon energy according to equation 3.1 and the determination of the total electron flux going through it, useful to determine the total number of photons impinging on the target via tagging efficiency measurements.

In fig. 3.7, the working principle of the tagger is shown. After interaction in the radiator, the electrons are deprived of a fraction of their energy, corresponding to the energy of the emitted photon (eq. 3.1). When going through the main body of the tagger -a 1.0 tesla, 70 tons bending magnet- the electrons will see their trajectory deflected with a curvature radius proportional to their energy. Hence, the position of the electron at the exit of the the magnet will then be directly related to its energy. Knowing this, the electron energy can be determined without ambiguity with a precision of  $\sim 2$  MeV. This matching is briefly explained in section 4.3.1. In order to measure this position, a set of 353 plastic scintillators

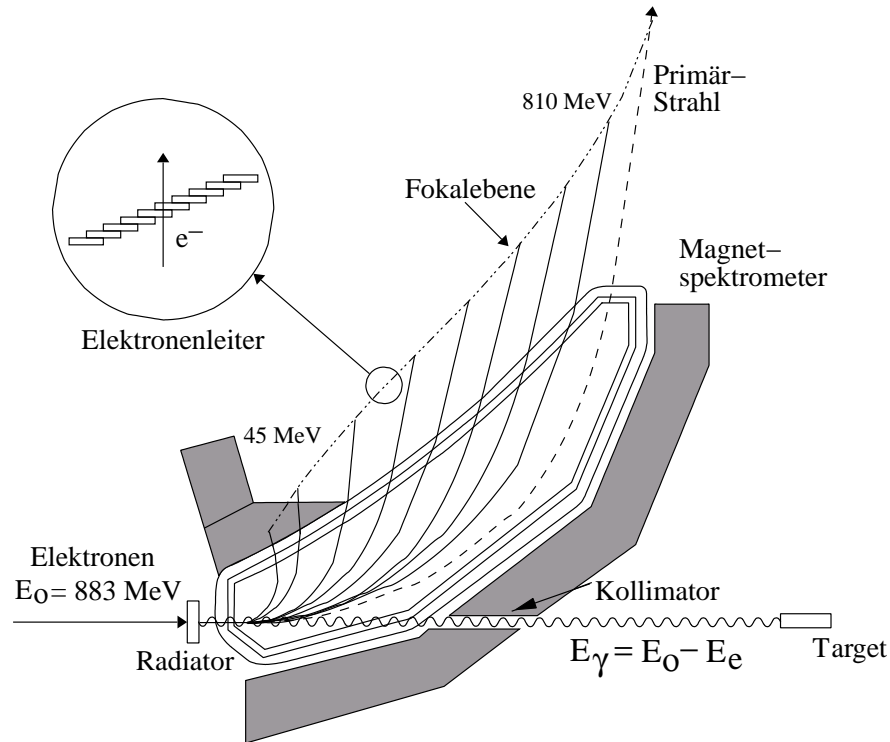


Figure 3.7: Schematic view of the tagger. After bremsstrahlung interaction in the radiator, the trajectory of the electrons is bent by the tagger magnet onto focal plane detectors.

is placed in the focal plane of the tagger. During our experiment, this so-called *focal plane detector* or *ladder* was set to cover an energy range between 69 and 820 MeV. However due to the  $1/E_\gamma$  nature of the bremsstrahlung energy distribution, the flux of electrons with a large energy is very important, so important that, with a beam current of 10 nA, the electron flux would saturate the corresponding ladder element. To avoid this, the first 69 channels, corresponding to photons up to 205 MeV (whose energy would anyway not have been sufficient to produce double pion events) have been switched off.

In order to reduce the background, the focal plane scintillators are overlapping (see excerpt in fig. 3.7). In this configuration, an electron has to cross at least two scintillators. Events that trigger only one element can be considered as background and are therefore rejected. Finally, let's note that only a minority of the electrons in the beam contribute to bremsstrahlung photon production. Most of the electrons don't undergo any interaction in the radiator and still have an energy of 883 MeV. These electrons ('beam dump') are deflected by the magnet onto a Faraday cup which records the total beam charge. Its readout is used to monitor the beam intensity.

Together with the ladder, a second focal plane detector with a higher resolution

was also build for the tagger [Rei96]. Similarly to the ladder, it consists of 96 overlapping scintillating elements with a photon energy coverage from 674 to 728 MeV and a resolution of  $\sim 400$  MeV. It is especially useful to study phenomena with large variations over small energy regions, such as  $\eta$  photoproduction close to threshold. For our work, it wasn't of much use and was therefore switched off. The second crucial task of the tagger is the determination of the total electron flux going through it. This flux is used in section 4.6 to compute the total number of photons impinging on the target, essential for a precise calculation of cross sections. For this purpose, the tagger signals are fed to live-time gated scalers that record the number of hits in each of the focal plane elements. They are read out once every 1000 events. Their output is used to produce plots such as the ones in fig. 3.5.

### 3.4 Liquid hydrogen target

The most convenient way to provide a dense free proton target is to use a liquid hydrogen target. In our experiment, a cylindrical (4.8 cm long, 4 cm diameter, 120  $\mu\text{m}$  thick) kapton cell was used. It was isolated with mylar and aluminum foils, and cooled to 21 K under a pressure of 1080 mBar so that it contained 57  $\text{cm}^3$  of liquid hydrogen. The target was developed at the Mainz University under the responsibility of A. Thomas.

In order to calculate cross sections (eq. 6.1), the density of protons in the target has to be known. This can be easily done using

$$N_p = \frac{N_A}{A_H} \rho_H L = 2.01 \cdot 10^{23} \text{cm}^{-2} \quad (3.11)$$

where  $N_A$  is the Avogadro number,  $A_H$  and  $\rho_H$  the hydrogen atomic number and density and  $L$  the target length.

While we were taking data, unwanted ice was steadily growing on the target exit window. This can't be neglected since, in addition to the hydrogen free protons, our photons can interact with the oxygen nuclei from the water molecules and contaminate our results. This problem is treated in appendix B. It was especially nasty during the July beamtime when the target was never re-heated to thaw the ice (the maximal ice thickness was 1.4 mm water equivalent [KasPr]) and no empty target measurement was performed.

## 3.5 Detectors

In the year 2002, the Crystal Ball detector was moved from its previous location at BNL<sup>7</sup> to MAMI. The possibility to use it in conjunction with TAPS as forward detector together with the excellent beam provided by MAMI opened the exciting prospect to measure a various range of photoproduction reactions up to a very good accuracy. The combined calorimeter made of the Crystal Ball, TAPS and their subsystems is an excellent tool, fulfilling all our detection needs with few limitations. It provides a very good time and energy resolution, an accurate determination of the nature of the particles and, above all, a  $\sim 4\pi$  solid angle coverage which is a prerequisite to measure reactions involving a large number of particles in the final state (typically,  $\eta \rightarrow 3\pi^0 \rightarrow 6\gamma$  or, for this work,  $\pi^0\pi^0 \rightarrow 4\gamma$ ) with a reasonable detecting efficiency.

### 3.5.1 The Crystal Ball

The Crystal Ball (CB) [Nef95] is a detector with a long and rich history. It dates back to the late 1970s when it was build at SLAC as a member of the first generation of large scale calorimeters. Once completed, it was used for several years at SLAC<sup>8</sup>, using the SPEAR<sup>9</sup> accelerator and at DESY<sup>10</sup> (1978 to 1986) before being put at rest at SLAC for a decade. It was then upgraded and used at BNL for some years (1995 to 2002) before being moved to MAMI in 2002. A summary of the majors achievements of the Crystal Ball at previous locations can be found in [Nef05]. The Crystal Ball is a highly segmented spectrometer made of 672 NaI(Tl) crystals arranged in a hollow 'sphere'. For practical reasons, the sphere is mimicked by an icosahedron whose triangular faces are divided in four smaller triangles which in their turn are divided into nine triangles such as represented in fig. 3.8. Due to this geometry, the crystals are not exactly identical but each of them is a 40.6 cm long truncated triangular pyramid. In order to leave space for the beam entry and exit and to give an easy access to the target, 48 crystal emplacements have been left empty. For practical reasons again, the CB is divided in two hemispheres,

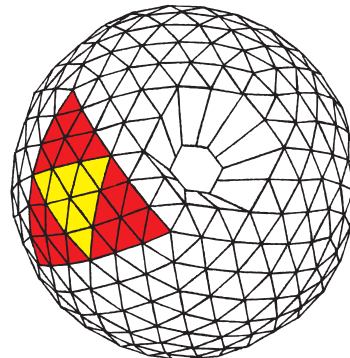


Figure 3.8: *Geometry of the crystal ball showing a major triangle (36 crystals) made of 4 minor triangles (9 crystals). The beam hole is also visible.*

<sup>7</sup>BNL: Brookhaven National Laboratory in Brookhaven, NY, USA

<sup>8</sup>SLAC: Stanford Linear Accelerator Collider in Stanford, CA, USA

<sup>9</sup>SPEAR: Stanford Positron Electron Accelerating Ring in Stanford, CA, USA

<sup>10</sup>DESY: Deutsches Elektron-Synchrotron in Hamburg, Germany

separated with two 0.8 mm stainless steel plates and a 8 mm air gap, perturbing slightly the detection efficiency in the equatorial region. Altogether, this geometry covers 94% of the total  $4\pi$  solid angle.

For the photon, the crystal ball has a good position resolution due to its high granularity and a good energy resolution. For the proton, the crystal length corresponds to approximatively one hadron interaction length. For the proton and charged pions, the position resolution is not optimal as the hadronic shower has a much smaller transverse extension than an electromagnetic shower. In most cases, the hadron energy will be deposited in one or two crystals only. A better position resolution for charged particles has to be provided by additional detectors: the wire chambers. Table 3.1 summarizes the most important characteristics of the Crystal Ball and fig. 3.9 shows a transverse cut of the overall arrangement of the complete CB system with the PID, the MWPC and the hydrogen target positions.

Crystal Length	40.6 cm = 15.7 radiation lengths
Inner triangular face side	5.1 cm
Outer triangular face side	12.7 cm
Angle coverage	$\theta = 2\pi, \quad 20^\circ < \theta < 160^\circ$
Energy resolution	$\frac{\sigma}{E} = \frac{2.7\%}{E(\text{GeV})^{\frac{1}{4}}}$
Minimum ionizing particle energy deposition	197 MeV

Table 3.1: *Some technical data about the Crystal Ball*

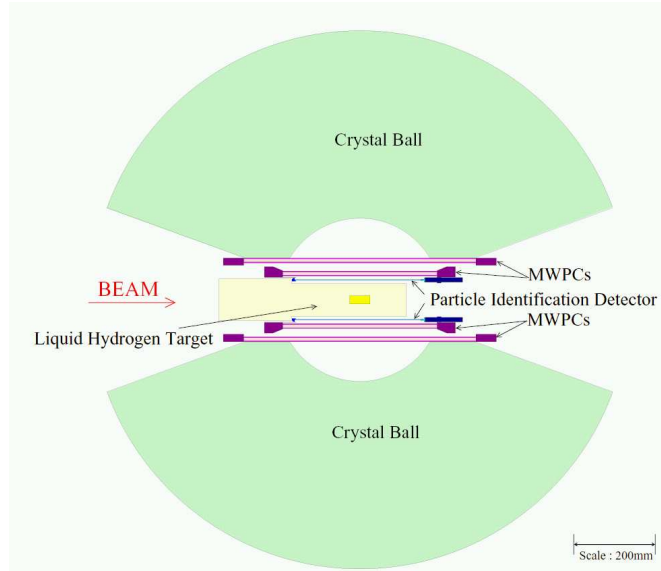


Figure 3.9: *Transverse view of the crystal ball showing the inner detectors (wire chambers and PID) and the hydrogen target.*

## Wire Chambers

A major imperfection in the Crystal Ball is the poor position resolution obtained when detecting charged particles. As explained previously, the energy deposition of charged particles in the CB occurs most of time in one or two crystals only. This makes the cluster reconstruction (section 4.4.1) inefficient to determine the impact point of the charged particle with a satisfactory accuracy. The two MWPCs (Multi Wire Proportional Chambers) were added to provide a much better angular resolution for charged particles. These detectors were recycled from the DAPHNE<sup>11</sup> detector [Aud91] used in the years 1990-2003 at MAMI.

Each MWPC consists of two concentric Rohacell cylinders. The outer cylinder is dressed with a set of cathode strips wound around it with a  $45^\circ$  angle in respect to its axis. The inner cylinder has a similar configuration, with strips wound in the other direction. In this configuration, each strip from one cylinder will cross every strip from the other cylinder twice. The anode wires are set parallel to the cylinder axis, in the gap between the two cylinders. This arrangement can be seen in fig. 3.11. When a charged particle crosses the gap, the filling gas will be ionized and, under the high voltage, the electrons will migrate to the anode wires and the gas ions to the cathode strips. This will in principle produce 3 signals, one in each cathode and one in the anode. These signals are then read out: a simple yes/no information is provided for the wires, whereas the strip signal amplitude will be amplified and recorded by an ADC. In section 4.4.3, we describe how the tracks of the charged particles can be reconstructed using the MWPC strips and wire signals and we determine the angular resolution. Table 3.2 gives some technical data about the MWPCs components. More information can be found in S. Schumann thesis [Sch07].

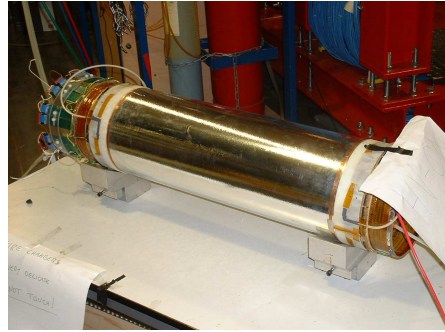


Figure 3.10: *One of the MWPCs before it was placed in the Crystal Ball. (P. Pedroni)*

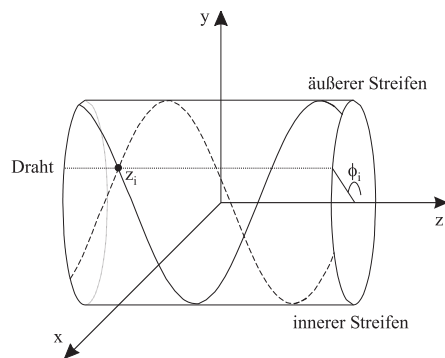


Figure 3.11: *Schematic view of a MWPC. A charged particle triggers three signals: one in a strip of each cathode and one in an anode wire. This allows the reconstruction of the hit position [Sch07].*

<sup>11</sup>Détecteur à grande Acceptance pour la Physique photo Nucléaire Expérimentale

Gas:	74.5% argon, 25% ethane, 0.5% freon
Anode wires:	Gold coated tungsten, diameter = $20\mu m$
Distance between wires:	2mm
Cathode strips:	Aluminum, thickness = $0.1\mu m$ , width = 4 mm
Distance between strips:	0.5 mm
Angle coverage:	$\phi = 2\pi$ , $21^\circ < \theta < 159^\circ$ ( $\approx$ CrystalBall)

	MWPC1	MWPC2
Length	36 cm	56 cm
Inner diameter	60 mm	92 mm
Outer diameter	68 mm	100 mm
Number of anode wires	192	288
Number of inner cathode strips	60	92
Number of outer cathode strips	68	100

Table 3.2: *Some technical data about the MWPCs*

## PID

As described in the previous sections, the Crystal Ball used with the wire chambers provides a precise determination of the the particle energy and position. However, no information on the nature of the particle can be obtained. Still, a precise particle identification is essential for a clean identification of the studied reaction. In order to identify the charged particles present in final states (protons, charged pions, electrons), the PID (Particle Identification Detector) was developed at the University of Glasgow for this round of experiment [Dow07]. It consists of a set of 24 plastic scintillators arranged cylindrically and placed as an inner detector between the target and the CB crystals. Some data about the PID can be found in table 3.3. As explained with more details in section 4.4.3, the particle identification is performed by comparing the total energy deposition in the Crystal Ball with the small energy  $\Delta E$  deposited in the PID scintillators by charged particles.

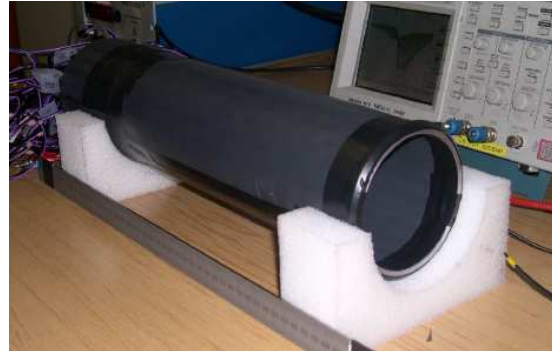


Figure 3.12: *The PID before it was placed in the Crystal Ball. (E. Downie)*

PID material	EJ204 plastic scintillator
Individual scintillator length	31 cm
Individual scintillator width	13 mm
Individual scintillator thickness	2 mm
Individual scintillator angle coverage	$\phi = 15^\circ$ $\theta = \theta^{CrystalBall}$
PID radius	100 mm
Minimum ionizing particle energy deposition	$\sim 400$ Mev
Proton Energy Deposition	1-3 MeV

Table 3.3: *Some technical data about the PID*

### 3.5.2 TAPS

The TAPS<sup>12</sup> detector has been developed at the end of the 1980s [Nov91] by an international collaboration to provide a state-of-the-art photon spectrometer allowing the measurement of photon energies and positions with a great accuracy. Its primary goal was the precise reconstruction of neutral mesons ( $\pi^0, \eta$ ) in their  $2\gamma$  decay channel. Over the last three decades, TAPS has been used at a large number of facilities<sup>13</sup>, performing a wide range of physics, mostly involving meson production. It was used at GANIL<sup>14</sup> and GSI<sup>15</sup> to study  $\pi^0$  and  $\eta$  production in heavy ion collisions and the two phonon resonances in peripheral reactions; at CERN to measure meson Dalitz decay and at KVI<sup>16</sup> to measure real and virtual bremsstrahlung in  $p + p \rightarrow p + p + e^+e^-$  and  $p + p \rightarrow p + p + \gamma$  reactions. In the meson photoproduction field, it has been used at MAMI and ELSA providing precise results on meson photoproduction off free protons, light and heavy nuclei, largely contributing to our present knowledge in this field. The range of physics studied with TAPS is so broad that an overview of its achievements wouldn't fit in a single paper. Over the years, all the publications on the physics done with TAPS and the technical knowledge about it have been collected in [TAPwww].

TAPS consists of a set of some hundreds of hexagonally shaped BaF2 crystals (nowadays  $\sim 600$ ) such as the one shown in fig. 3.13. This geometry allows the crystals to be arranged in a lot of different configurations, making TAPS a highly modulable detector. Indeed TAPS has never been used twice in the same configuration over the different experiments it was part of. In our experiment, 512 BaF2 crystals were arranged in an hexagonal forward wall at a distance of 173.4 cm from the target. This configuration, shown in fig 3.14, has been chosen

<sup>12</sup>TAPS: Two Arms Photon Spectrometer (in reference to its first configuration at GSI)

<sup>13</sup>For this reason, the more suitable acronym *Travel Around Photon Spectrometer* has been proposed

<sup>14</sup>GANIL: Grand Accélérateur National d'Ions Lourds, Caen, France

<sup>15</sup>GSI: Gesellschaft für Schwerionenforschung, Darmstadt, Germany

<sup>16</sup>KVI: Kernfysisch Versneller Instituut in Groningen, The Netherlands

to provide a full coverage of the solid angle. At this position, TAPS will detect particles that escape the Crystal Ball through its forward hole ( $\theta < 21^\circ$ ).



Figure 3.13: *Each TAPS element is made of a 25 cm BaF2 crystal corresponding to 12 radiation lengths. The main part of the crystal is hexagonal, with a 2.5 cm end cylinder connected directly to a photomultiplier for read-out.*

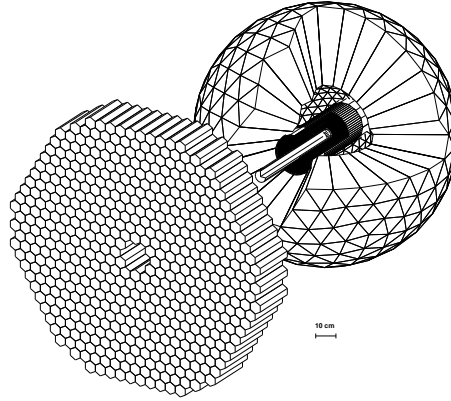


Figure 3.14: *Configuration of detectors. The 512 BaF2 crystals of the TAPS forward wall cover the hole of the Crystal Ball to provide a  $\sim 4\pi$  angle coverage.*

The BaF2 excellent characteristics make it a very good choice to build scintillating crystals. We will give here an overview of the main features that are also summarized in table 3.4.

- Due to the fast rise time of the scintillation pulse, the intrinsic time resolution of a single crystal is very good, about 200 ps. This is an essential feature for an accurate particle identification using the time of flight of the particle (section 4.4.2).
- The photon detecting efficiency and the energy resolution are high over a wide range of energies.
- The high granularity of TAPS provides a good resolution in the position determination
- A useful property of TAPS is the possibility to perform particle identification using pulse shape analysis (PSA). As shown in fig 3.15, the total BaF2 scintillation light output has 2 components. The decay constant of the short component is of the order of the nanosecond while for the long component it is of the order of the microsecond. PSA is done by integrating the signal over a short and a long time gate. As the short component relative intensity is higher for photons than for nucleons, calculating the

ratio of the two light components will provide a good tool to identify the particles (section 4.4.2).

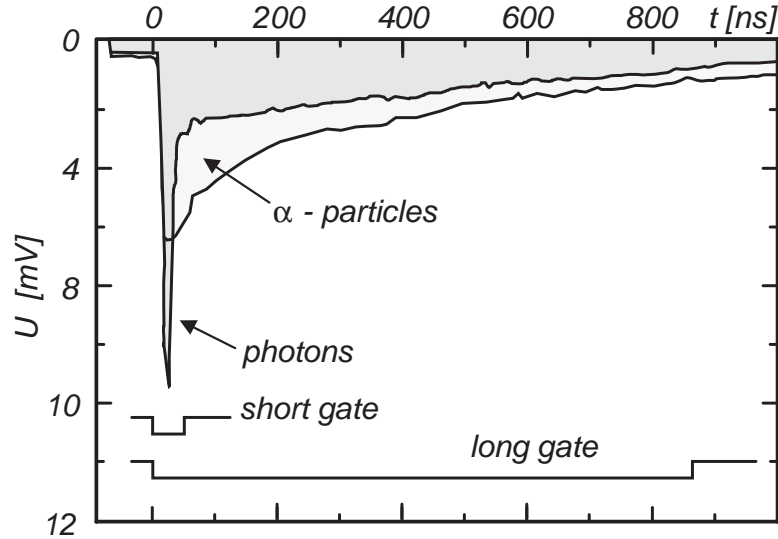


Figure 3.15: Typical pulse shape of a photon and an  $\alpha$ -particle. The light output measured over a short and a long time gate are used to determine the nature of the particle using PSA.

Crystal length:	25 cm (12 radiation lengths)
Hexagon inner radius:	5.9 cm
End cylinder diameter:	5.4 cm
Single crystal energy time resolution:	200 ps
Energy Resolution for photons < 800 MeV:	$\frac{\sigma}{E} = \frac{0.59\%}{E_\gamma + 1.9\%}$ ( $E_\gamma$ in GeV)
Angle coverage:	$\phi = 2\pi, 1^\circ < \theta < 21^\circ$
Long light component decay constant:	0.76 ns
Short light component decay constant:	620 ns

Table 3.4: Some technical data about TAPS

### TAPS Vetos

TAPS can't discriminate between charged and neutral particles. As the proton and the neutron signatures in PSA and in time of flight analysis is identical, it will be impossible to tell them apart using TAPS alone. The situation is the same for photons and electrons and an additional information has to be provided to identify charged particles. For this purpose, a set of 512 plastic scintillators [Jan00] were placed in front of the TAPS forward wall, one in front of each crys-

tal<sup>17</sup>. These vetos are made of 5 mm thick (0.025 radiation length) NE102A scintillating plastic. They are connected by lightguides to one of the 32 photomultipliers, a single photomultiplier is responsible for 16 vetos. This veto system is relatively basic and only provides a yes/no information about the passage of a charged particle with an efficiency of  $\sim 80\%$ . This information will be included in the particle identification process of TAPS in section 4.4.2. In order to improve the charged particle efficiency, a new set of vetos providing a readout of the energy deposited by the charged particle and a much higher detecting efficiency has been developed at the University of Giessen and is currently used at MAMI.

## 3.6 Electronics

The goal of the electronics is to collect the informations that come out of the photomultipliers and to treat them so that they can be stored on computers in a convenient form. The electronic system has to provide a digitization of the time and the amplitude of the output signal. It has to be fast enough to cope with the high rate from MAMI ( $\sim 1000$  events per second). It has to come with an efficient build-in trigger that avoids the overwhelming of the storage computers with useless data. Finally, it has to fulfill some practical needs: as the components of the electronics stay close to the detector in the A2-hall, they have to be radiation hard and, in order to optimize the available money and manpower, they will have to be based, as much as possible, on already existing electronic devices.

### 3.6.1 Crystal Ball electronics

The Crystal Ball electronics have been developed especially for the 2004/2005 round of experiments. They are, as much as possible, made of already existing electronic devices. For example, the TDCs are CATCH TDCs developed for the COMPASS experiment at CERN (some more details can be found in fig. 3.18). In this part, we will only give an overview of the tasks performed by these electronics. The interested reader can find exhaustive technical information in D. Krambrich thesis [Kra07], a large part of which being dedicated to the implementation of this new Crystal Ball electronics.

Fig 3.16 shows a simple, schematic view of the electronics between the Crystal Ball and the storage computer.

- 1 The analog output signals from the NaI crystals photomultipliers are transmitted to an active splitter where they are divided in groups of 16 crystals.

---

<sup>17</sup>plus two unused vetos

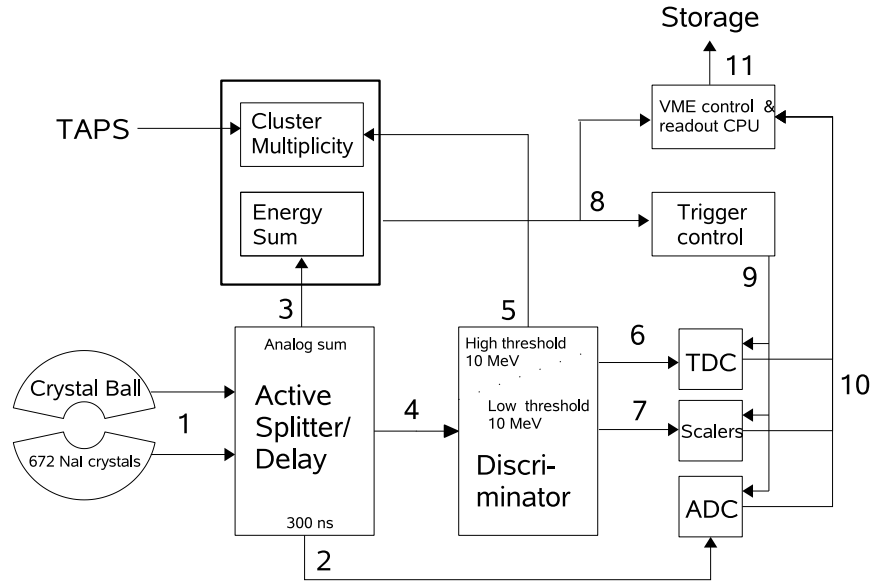


Figure 3.16: *Schematic representation of the Crystal Ball electronics*

- 2** The amplitude signal is delayed by 300 ns and fed to the ADCs
- 3** The amplitude of all 672 crystals is summed and sent to the energy sum trigger.
- 4** The summed amplitude of the 16-crystal groups is also calculated and sent to the discriminator. The discriminator provides a high and a low threshold of  $\sim 20$  and  $\sim 2$  MeV respectively.
- 5** The number of 16-crystals groups whose energy is above the high threshold is sent to the cluster multiplicity trigger (for points 3 and 5, the trigger is treated in more detail in section 3.6.3)
- 6,7** The signals above the low threshold are used to start the TDCs and the scalers.
- 8,9** The trigger decision is sent to the ADCs, TDCs and scalers via the trigger control system.
- 10,11** On a positive trigger decision, the information is digitized in the ADCs and TDCs and sent to the storage computer.

### 3.6.2 TAPS electronics

A new compact readout board has been developed for TAPS [Dre03] to replace the previous electronics. This new electronics provides high count rate capabilities, fast digitization, very good resolution, good compatibility to complex trigger

architecture and the possibility to be used close to the detector. The development of this electronics was the subject of P. Drexler thesis [Dre04]. All the relevant technical information can be found there.

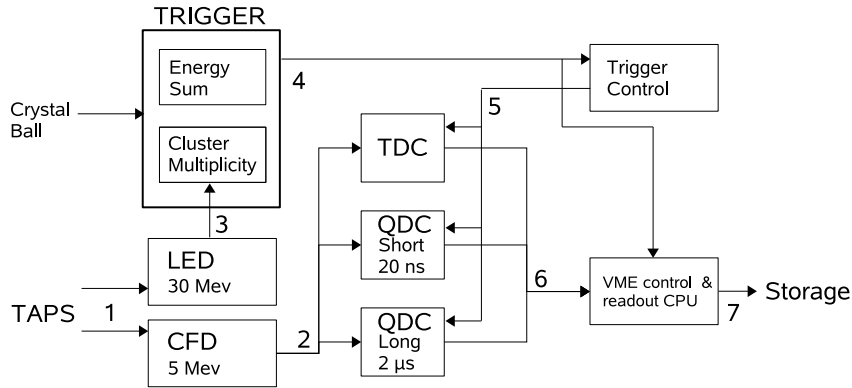


Figure 3.17: *Schematic representation of TAPS electronics*

Here again, only a schematic overview of the electronics will be given.

- 1 The analog output signal from a BaF2 crystal photomultiplier is transmitted to a CFD (Constant Fraction Discriminator) with a 5 MeV threshold and a LED (Low Edge Discriminator) with a 30 MeV threshold.
- 2 A signal higher than the CFD threshold is the signature of a hit in the crystal. It gives the start signal for energy integration in both long and short gate QCDs and for the time measurement in the TDC. The constant fraction technique with minimum walk enables us to determine the start signal very precisely and thus to perform time of flight and pulse shape analysis with a high resolution.
- 3 If the signal is higher than the LED threshold, it will be sent to participate to the trigger.
- 4,5 The trigger decision is sent to the QDCs and TDC. It stops the time measurement in the TDC.
- 6,7 On a positive trigger decision, the digitized energy and time informations are sent to the storage computer.

### 3.6.3 Trigger

When performing meson photoproduction off a proton target with photons up to 820 MeV as we do here, the dominant process to the total cross section is the

single pion photoproduction. Compared to the double pion production and the delta magnetic moment reaction, the cross section for single pion production is higher by one and three orders of magnitude respectively. In order not to overwhelm the storage computers with unwanted single pion data, one has to come with a good online filter - or *trigger* - implemented in the electronics.

As already mentioned in the last two sections, the trigger consists of two independent parts: the energy sum of the Crystal Ball and the cluster multiplicity trigger. The CB energy sum is simply carried out by summing the analog energies of all 672 NaI crystals. If the total energy deposition is below a definite threshold - 40 MeV in our experiment - the event will be rejected. This is not a very stringent condition and will keep a lot of single pion events, whose production threshold<sup>18</sup> is around 150 MeV. A higher energy condition could have been set in order to reject more low energetic background if the TAPS energy had been taken into account in the energy sum. However, for technical reasons - the TAPS electronic boards haven't been designed to provide a readout of the analog energies - this has not been implemented.

The cluster multiplicity is used to reject or keep events according to the number of final state particles. For this purpose, the active splitter in the Crystal Ball electronics divides the 672 NaI crystal readout in 45 logical segments made of 16 contiguous crystals and calculates the analog energy sum of each individual segment. The typical size of a single particle energy deposition is small enough to be contained within one logical segment so that we can assume that one firing segment corresponds to one particle<sup>19</sup>. The analog energy is then sent to the discriminator where, if the energy sum is above a 20 MeV threshold, a so-called multiplicity hit will be recorded. TAPS takes part in this trigger in a similar way: it has been split in 4 logical segments made of 128 BaF2 crystals. If any crystal in a segment has an energy deposition above the 20 MeV LED threshold, a multiplicity hit will be recorded. The main purpose of this trigger is to reject as much single  $\pi^0$  photoproduction ( $\gamma p \rightarrow \pi^0 p; 2\gamma$  in the final state) events as possible while conserving  $\Delta$  magnetic moment events ( $\gamma p \rightarrow \gamma' \pi^0 p; 3\gamma$  in the final state). The trigger condition was therefore set to keep events with three or more multiplicity hits (referred to as *M3 trigger*<sup>20</sup>) and to reject events with a lower multiplicity. As we shall see in chapter 5, the probability for the proton not to be detected is high at low energies. It was therefore not included in the multiplicity trigger. Fig 3.18 shows a technical scheme of the trigger implemen-

---

<sup>18</sup>150 for  $\gamma p \rightarrow \pi^+ n$  and 145 for  $\gamma p \rightarrow \pi^0 p$ .

<sup>19</sup>This approximation is not valid if the energy of a particle is deposited along the border between two logical segments. In this case, a single particle will produce two multiplicity hits. On the contrary, if two particles are detected in the same segment, only one hit will be recorded. To account for this features, a simulation of the trigger will have to be implemented when working with simulated data.

<sup>20</sup>For the needs of the  $\Delta$  magnetic moment experiment, a *downscaled M2 trigger* was also used. This means that 1 out of 50 events with two multiplicity hits was recorded.

tation in the electronics. Again, exhaustive technical information can be found in [Kra07].

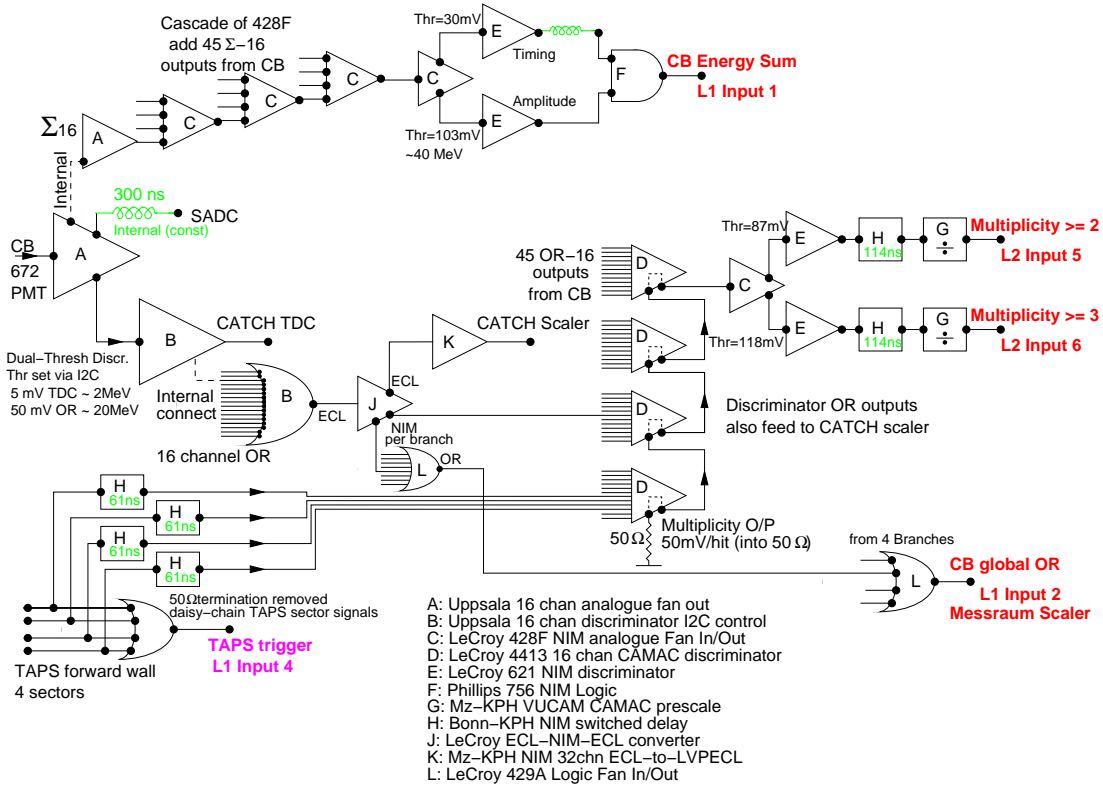


Figure 3.18: *Technical scheme of the trigger. The upper part shows the CB energy sum trigger, the middle part the CB multiplicity trigger and the lower part the TAPS multiplicity trigger. (J. Annand)*

### 3.7 Data taking

The data for our experiment was taken during the 2004/2005 round of experiments at MAMI and was run in parallel with the  $\Delta^+(1232)$  magnetic moment measurement (see section 2.7). Altogether, 710 hours of data have been taken, split in three parts. 305 hours were taken in July and August 2004, 180 in September 2004 and 120 in January 2005. (In January, 100 additional hours were taken with an amorphous iron radiator producing circularly polarized photons only and with a smaller energy (up to 570 MeV). They were needed to optimize the  $\Delta$  magnetic moment experiment and were not used in our work.) The main experimental conditions are summarized in table 3.5.

Period	July/August 2004	September 2004	January 2005
<b>Radiator</b>	Diamond	Diamond	Diamond
<b>Beam Energy</b>	883.25 MeV	883.25 MeV	883.25 MeV
<b>Beam Current</b>	8 nA	12 nA	12 nA
<b>Polarization Edge</b>	440 MeV	400 MeV	400 MeV
<b>Full Target</b>	305 hours	180 hours	120 hours
<b>Emty Target</b>	-	100 hours	16 hours
<b>Tagger Range</b>	205-820 MeV	205-820 MeV	205-820 MeV
<b>Trigger</b>	$M \geq 3$ (downscaled M2)	$M \geq 3$ (d. M2)	$M \geq 3$ (d. M2)

Table 3.5: *Summary of the most important experimental conditions. More technical information is available in the A2 logbooks and run sheets conserved at Mainz.*

During the same round of experiments, two important fields have also been investigated using the state-of-the-art accelerator and detectors available at MAMI. In November and December,  $\eta$ -mesons were produced (using a much higher beam intensity) to study their decay into three  $\pi^0$  [Unv08], rare  $\eta$  decays like  $\eta \rightarrow \pi^0 \gamma \gamma$  [Bru07] or to measure precisely the  $\eta$  mass [Nik08]. The other important group of data was taken in spring 2005 on several solid targets ( $^{12}\text{C}$ ,  $^{40}\text{Ca}$ ,  $^{210}\text{Pb}$ ,  $^7\text{Li}$ ,  $^{16}\text{O}$ ) to study in-medium properties of nucleon excitations with double  $\pi^0$  photoproduction [Lug07], [Gre07] or coherent  $\pi^0$  photoproduction off nuclei [Tar07]. About this last point a first article has been published recently, showing very good results [Tar08]. It will be followed by more publications on all of these subjects in 2008.

## 4 Data processing

*Once data taking is over, the fruit of our work consists of large data files made of nothing more than numbers. Numbers that correspond to the intensities of the signals measured and recorded by the different parts of the detector. In order to be able to interpret these numbers as physical values such as energies and times, a long time effort has to be done on the calibration of these data. This chapter presents the various techniques used to perform the calibration of every element of our detector.*

*Once this has been done, we stand at a point where we know the time at which a particle went through the detector, the energy it has deposited in it and its approximate position. But we don't have any clue about the nature of this particle. In the second part of this chapter, we will show how all basic informations are combined together in order to distinguish between protons, pions, electrons and neutrons.*

*In order to efficiently achieve all this sorting, recording, calibrating and analyzing operations, one needs a convenient common playground to work on. An analysis framework especially designed to fulfill our needs has been designed by the University of Glasgow and will be presented in the very beginning of this chapter.*

### 4.1 AcquRoot analysis framework

AcquRoot is a program that has been especially developed for the CB/TAPS round of experiments at MAMI. It is designed to readout and store the data coming out of the detectors and to provide an efficient framework for their analysis. AcquRoot is an upgrade of ACQU, the software formerly used at MAMI since the completion of MAMI B. It consists of an elaborate, multi-threaded program mainly written by J. R. M. Annand from the university of Glasgow. All relevant technical information can be found in [Ann05]. From a user point of view, AcquRoot might simply be seen as an extension of ROOT, the high energy physics data handling suite provided by CERN [ROOwww]. Written in C++, ROOT uses the modularity of this language and consists in a large number of classes, all of them performing a specific task. Using the same principle, AcquRoot can

be seen as a graft, enriching ROOT with classes performing the specific tasks needed to handle the data from our detectors.

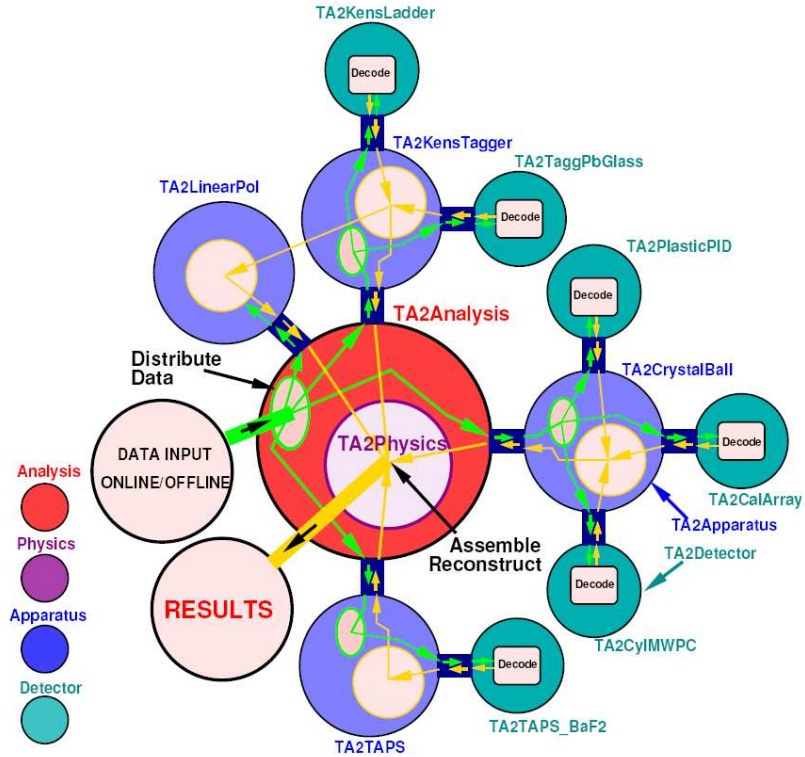


Figure 4.1: *Tree structure of AcquRoot. The path of the data is indicated by the arrows showing where each task is performed. Taken from [Ann05].*

The structure of AcquRoot (or at least the relevant part in everyday use) is shown in fig 4.1. Though somewhat intricate, this picture perfectly illustrates the advantages in using an object-oriented programming language: the basic operations such as energy and time calibration are performed locally (green): a dedicated class is written for each subsystem of each detector. For example, TA2TAPS\_BaF2 deals with the TAPS BaF2 crystals or TA2PlasticPID with the PID and so on. Going one step higher (blue), the data from each subsystem is grouped in three classes corresponding to each detector, TA2TAPS, TA2CrystalBall and TA2Tagger where more elaborate work, requiring information from more than one subsystem is performed. The typical example here is the particle identification, which, e.g. in the case of Crystal Ball combines informations from the NaI crystals, the wire chambers and the PID. Finally, all informations from the three detectors are merged into a central TA2Physics class in which the events are reconstructed and all the subsequent physics is performed. Let's note also that AcquRoot nicely takes advantage of the concept of

inheritance. Only four generic classes are written (TA2Detector, TA2Apparatus, TA2Physics and TA2Analysis, see left part in fig. 4.1) with features common to all subsystems such as time end energy calibration in the case of TA2Detector. All the individual classes are then simply derived (or *inherit*) from one of these base classes. This specification only requires small adaptations, making the work much more efficient in preventing from writing all classes from scratch.

## 4.2 Time calibration

The principle for both time and energy calibration is quite simple. We want to establish a matching between raw spectra produced by TDCs and ADCs and physical values. In other words, transforming TDC channels into nanoseconds and ADC channels into MeVs.

Let's first consider time calibration which is simpler as some simplifications can be done that are not valid for energy calibration. We will first assume that, for each detector the conversion value between TDC channels and nanoseconds can be kept constant. For the tagger, this conversion factor has been measured in a previous calibration performed by the Glasgow group at the time the tagger was installed. The value is 0.18 ns/channel. For the CB, the use of CATCH TDCs ensures the stability of the conversion factor for all crystals. The value is 117 ps/channel. For TAPS, the use of a CFD discriminator as a TDC start and of a common stop based on the trigger decision as well as some further tests make the use of a constant value for all TDCs reasonable. This makes the calibration work much simpler. Once this is set, the only remaining thing to do is the alignment of all TDCs of the detectors in order to optimize the overall time resolution. This will be done in the following for each element of the complete detector separately.

### 4.2.1 Tagger time calibration

The alignment of all tagger TDC spectra is presented in fig 4.2a. It is done by fitting each TDC spectrum with a Gaussian distribution, determining the mean position of this Gaussian and adding a corresponding offset to the TDC to correct for the misalignment of the peaks. Using this method, we can achieve an overall intrinsic tagger time resolution<sup>1</sup> of  $\sim 10$ ns. See fig. 4.2b. In the following, the time resolution for our experiment will be improved with the inclusion of CB and TAPS times.

---

<sup>1</sup>Resolutions mentioned in this work will always be FWHM resolutions.

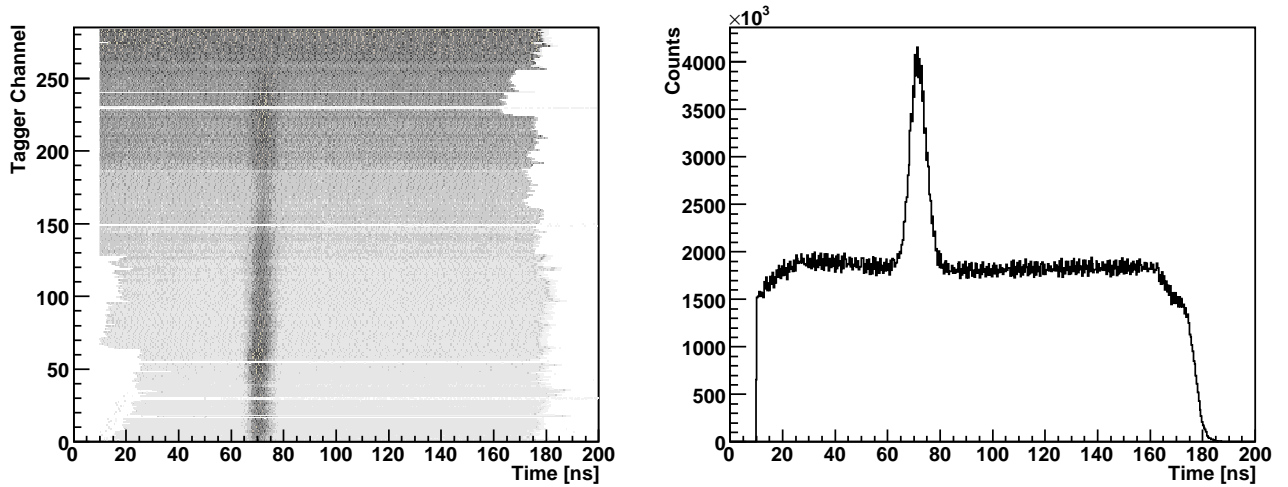


Figure 4.2: *Tagger Time Calibration*. Left: *Time alignment of all Tagger TDCs*. Right: *Tagger time for all channels (projection of the left side plot on the X-axis)*. A resolution of 10ns is achieved.

#### 4.2.2 TAPS time calibration

The time calibration of TAPS is performed in two steps. First, all TDCs are aligned with a Gaussian fit of their peaks in the same way as the tagger. Now, the relative alignment of the 510 TAPS TDCs isn't sufficient to perform tagger random background subtraction (see section 4.5), time of flight particle identification (section 4.4.2) and to get a good time resolution. Such tasks require to know the total duration of an event characterized by its 'beginning' and its 'end'. The time references chosen here are the tagger as the *start* signal and TAPS (or CB) as the *stop* signal. In practice, this means that we have to determine this coincidence time between the tagger and TAPS and to align all tagger and TAPS TDCs in order to minimize this time. Before doing this, let's first have a look at how the TDCs start and stop signal are defined for each detector. This will define the way how TAPS and the tagger will have to be combined in order to perform this calibration. Based on the discussion from section 3.6, we have

	START	STOP
Tagger	Tagger Element	Trigger
TAPS	CFD	Trigger
Crystal Ball	Trigger	NaI Element

Table 4.1: *Summary of start and stop signals*

For the tagger and TAPS, the start signal is given by individual elements. A

common stop is applied by the electronic trigger. Things are opposite for the crystal ball. Since this trigger time has a worse intrinsic resolution than the detectors, it is desirable to get rid of it. As shown in eq. 4.1 this is made possible by the subtraction of  $t_{tagger}$  from  $t_{TAPS}$

$$t_{TAPS-tagger} = (t_{trigger} - t_{CFD}) - (t_{trigger} - t_{tagger}) = t_{tagger} - t_{CFD} \quad (4.1)$$

Knowing this, each Tagger Element and each TAPS Crystal have now to be calibrated individually. In principle, all  $352_{Tagger} \times 512_{TAPS}$  differences between one tagger and one TAPS element should be computed, their peak fitted to determine their position and the corresponding offset applied to the TDCs. To avoid this time consuming task, we will proceed in an iterative way by first calculating all 512 differences between each individual TAPS TDC and all tagger TDCs. The 512 peaks will then be fitted by a Gaussian and aligned. In a second step, the same procedure will be applied in the opposite way, plotting all 352 differences between one tagger channel and all TAPS TDCs. These differences will be fitted the same way and the tagger TDCs shifted accordingly. This procedure will be repeated <sup>2</sup> until the resolution doesn't improve any more. The results are shown in fig. 4.3. The time resolution obtained with this method is smaller than 2ns.

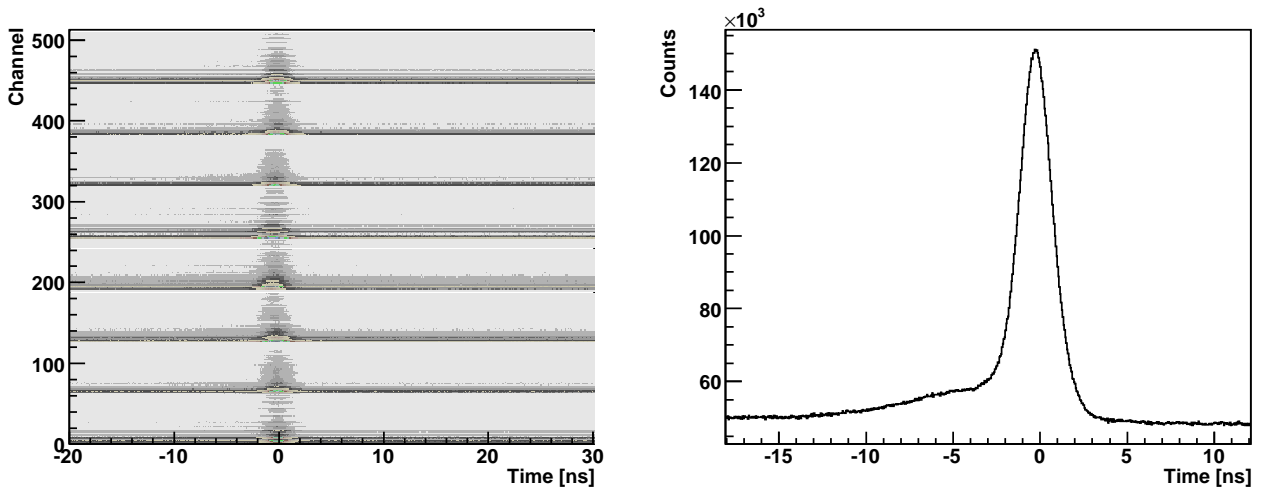


Figure 4.3: *TAPS Time Calibration.* Left: *Alignment of all 512 time differences between one TAPS crystal and all Tagger channels.* Right: *Time difference for all channels (projection of the left side plot on the X-axis).* A resolution of less than 2 ns is obtained.

<sup>2</sup>Usually, two iterations are sufficient to get an optimal resolution

### 4.2.3 Crystal ball time calibration

The Crystal Ball is calibrated using the same procedure. The only difference is the way tagger and Crystal Ball times are combined. According to table 4.1,  $t_{CB}$  and  $t_{tagger}$  have to be added to get rid of  $t_{trigger}$ .

$$t_{CB-tagger} = (t_{trigger} - t_{CB}) + (t_{tagger} - t_{trigger}) = t_{tagger} - t_{CB} \quad (4.2)$$

The iterative shifting of the tagger-Crystal Ball Time differences is then identical as what was performed for TAPS. The results are shown in figure 4.4. For the Crystal Ball, a resolution of  $\sim 4$  ns is achieved.

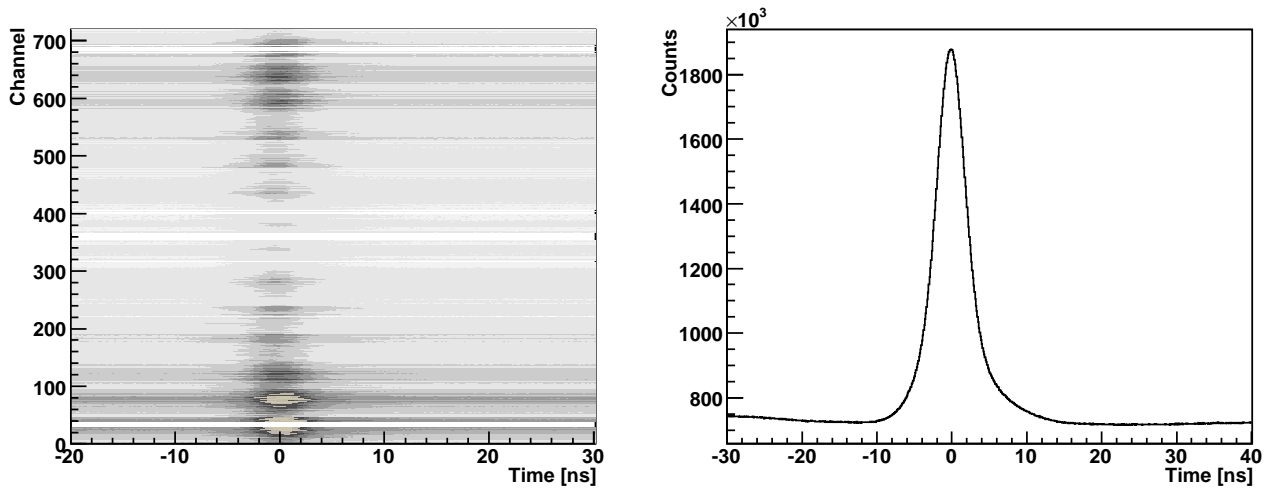


Figure 4.4: *Crystal Ball time calibration. Left: Alignment of all 720 time differences between one CB crystal and all tagger channels. Right: Time difference for all channels (projection of the left side plot on the X-axis). A resolution of  $\sim 4$  ns is obtained.*

Unlike TAPS and the tagger<sup>3</sup>, the Crystal Ball time depends on the energy of the measured particle. This is due to the design of the Crystal Ball electronics where the TDC start is defined by the external trigger. A particle with a small energy will need more time to activate the trigger low energy threshold that starts the measurement. A correction of this so-called *walk* was applied to the CB times to obtain the results shown in fig 4.4. For a complete treatment of the walk correction, see [Hor06]

<sup>3</sup>In TAPS, the use of CDFs make the time determination precise enough for the walk to be considered as neglectable. In the tagger, the electron in the tagger are minimum ionizing particles. There is no correlation between their energies and the time determination.

### PID time calibration

The time calibration of the PID doesn't bring any new technique forward. As for the Crystal Ball, times are measured by CATCH TDCs which have a constant conversion factor of 0.117 ns/channel. All 24 channels are fitted by Gaussian and aligned. This gives a resolution of 3ns for the PID. In that case, no relative timing of the PID to TAPS has been performed as it was thought that the improvement in the resolution would be very little.

## 4.3 Energy calibration

### 4.3.1 Tagger energy calibration

As seen in the description of the tagger (3.3), the electron having produced a photon via bremsstrahlung in the radiator is detected by one of the 353 scintillators in the focal plane detector. The deflection of the electron by the tagger magnetic field - and therefore the position at the exit of the tagger magnet - is proportional to its energy. Thus, the tagger energy calibration consists in the matching between the electron energy and the corresponding focal plane detector position. In order to avoid tedious, channel per channel calibration, a computer program, TagCal, has been written by the University of Glasgow [Tagwww]. It is based on the position of the scintillators in the focal plane detector and the field mapping along the main beam trajectory. When giving the beam energy and the NMR field value to TagCal, it returns the correspondence between the electron energy and the tagger channel as well as some other useful values such as photon energy, channel width, momentum or magnetic field.

### 4.3.2 TAPS energy calibration

We want to establish a correspondence between ADC channels and the actual energy deposited in the BaF2 crystals. For this purpose, so called *cosmic-data* have been taken before and after each beamtime period, sometimes also during breaks in the data taking. They consist of long time ( $\sim \frac{1}{2}$  day) beam off measurements for which most of the particles detected in the crystals are muons produced in cosmic rays interactions in the atmosphere.

Fig 4.5 shows the spectrum of such a cosmic measurement. These muons are minimum ionizing particles which deposit 6.45 MeV/cm in the BaF2 crystals. In our setup, with the crystals being arranged horizontally and the muons mostly coming from above, the most likely energy deposition in the crystals is 37.7 MeV

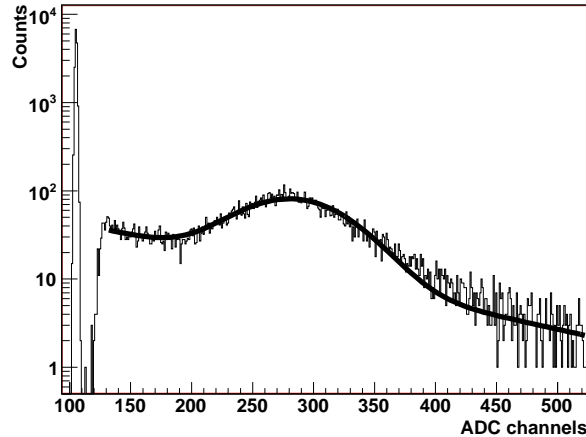


Figure 4.5: *TAPS energy calibration spectrum for a single crystal showing the pedestal peak at 0 MeV and the cosmic muons peak at 37.7 MeV.*

[Röb91]. This peak alone is not sufficient for an absolute calibration of the energy. A second reference in the ADC spectra is provided by the TAPS pedestal pulser. During cosmic data-taking, this electronic module forced a readout of all ADCs once per second, creating a large peak at zero energy. In order to carry out the calibrations, both peaks are fitted to determine their positions channel-wise. These two values are then used to establish the matching between ADC channels and MeVs for each crystal. This procedure is applied twice, once for the long and once for the short integration gate.

This first step in the energy calibration is however only valid in this low energy range and for minimum ionizing particles. At higher energies, the gain can vary up to a few percent: due to energy loss (energy deposition below the CFD threshold, electromagnetic shower bigger than the detecting volume, other energy losses in the crystals) the mass of the reconstructed  $\pi^0$  is somewhat smaller than the expected value of 135 MeV. To account for this, the output energy of the crystals has to be scaled with a correction factor. To determine this *TAPS fudge factor*, we plot the invariant mass of  $\pi^0$  for which one of the decay photons goes into TAPS, the other into the Crystal Ball. We then adjust the factor for this invariant mass to match 135 MeV. This gives a value of 1.147 for the TAPS factor that is applied to every TAPS crystal.

### 4.3.3 Crystal ball energy calibration

During the commissioning phase, a preliminary calibration of the Crystal Ball has been performed to set hardware thresholds at correct levels. NaI crystals were

irradiated with a  $^{241}\text{Am}/^9\text{Be}$  source. The response of the photomultipliers was adjusted for the peaks produced by the 4.438 MeV decay photons to be aligned for all 720 ADC spectra.

This low energetic gain matching is not precise enough for a satisfactory calibration of the much more energetic particles involved in this experiment. The fine-tuning of the calibration was done using the  $\gamma p \rightarrow \pi^0 p$  reaction. As this reaction is kinematically overdetermined, the  $\pi^0$  energy can be calculated theoretically as a function of the incoming photon energy as well as measured experimentally, reconstructing it from its two decay photons. The ratio between both energy values is computed for each crystal and used to correct the calibrations. As a photon deposits its energy in more than one crystal, a change of the central crystal calibration will affect the surrounding ones. Therefore, the correction process has to be repeated iteratively until the results converge. With this technique, a resolution of 8.3 MeV is achieved for the  $\pi^0$  mass.

### PID energy calibration

The main purpose of the PID is to provide banana plots for particle identification (fig. 4.11). Since the bananas are fitted individually for each detector, an absolute calibration of the energy deposited in the PID elements (i.e. the banana absolute position) is not a major issue. A quick calibration was anyhow performed to get similar banana plots for each PID element. A Monte-Carlo simulation showed that the average energy deposition in the PID by particles between 32 and 48 MeV is 0.4 MeV for charged pions and 2.3 MeV for protons. The calibrations are adjusted to these values, so that the distance between the pion and proton peaks is always 1.9 MeV.

## 4.4 Particle identification

### 4.4.1 Clusterization

#### Cluster reconstruction

When a photon hits a crystal, it creates an electromagnetic shower through electron-positron pair creation and bremsstrahlung photons. The typical size of such a shower is defined by the Molière radius whose values - 4.3 cm for NaI and 3.4 cm for BaF2 - are larger than the size of the individual crystals. Therefore, the photon energy deposition spreads over a few crystals. The purpose of the clustering is to group all hits corresponding to a single particle and combine the informations of these neighbouring crystals in order to reconstruct the particle. To achieve this, a clustering routine has been implemented that performs the following steps. In the list of all individual hits in the crystals, it first looks for the one with the maximal energy. It then scans through all the neighbours

of this central crystal and adds all crystals with a non-zero hit to the cluster. For each added neighbour, this neighbour searched is performed again and new crystals are added to the cluster. This procedure is repeated iteratively until no more abutting crystal with a non-zero hit remains. Once this first cluster is built, all its member are marked as 'non-hit' and the procedure is repeated to build a second cluster. More and more clusters are built that way until eventually no more isolated hit remains in the list. This technique that builds only one cluster out of a set of contiguous crystals was chosen in order to minimize the occurrence of split-offs<sup>4</sup> which are a major source of background in the  $\bar{\gamma}p \rightarrow \gamma'\pi^0p$  reaction used to determine the magnetic moment of the  $\Delta(1232)$  resonance. As a drawback, two overlapping clusters will be interpreted as one single cluster. However, due to the small number of final state particles, this is unlikely and only a small fraction of the total number of events are lost that way.

### Time, energy and position

Once clusters are build, one wants to determine the time, the energy and the position of the incident particles by combining the informations of the individual crystals belonging to the cluster. The energy is defined as the sum of all individual crystals energies and the time as the time of the cluster central crystal. The position determination is less straightforward. If one would simply calculate the center of gravity of the cluster by computing the position of the crystal weighted with the energy deposition, the crystals with a small energy deposition would be slightly underweighted. A more proper determination is obtained when weighting the position of each crystal in the cluster with the square root of the deposited energy.

$$\vec{x} = \frac{\sum_{i=1}^{N_{Crystal}} x_i \sqrt{E_i}}{\sum_{i=1}^{N_{Crystal}} \sqrt{E_i}} \quad \text{where} \quad \vec{x} = (x_x, x_y, x_z) \quad (4.3)$$

### Shower Depth Correction in TAPS

When an electromagnetic shower forms in the crystal, the depth corresponding to the maximal energy deposition [PDG06] is given by

$$t_{max} = 2.05 \left( \ln \frac{E}{12.7 \text{MeV}} + 1.2 \right) \quad \text{for BaF2} \quad (4.4)$$

---

<sup>4</sup>A single particle producing more than one cluster

Due to the wall structure of TAPS, particles detected at the outer edge of TAPS are coming askew. A shift between the position where the particle is supposed to be detected (at the crystal surface) and the actual position of the energy deposition will then appear. This is illustrated in fig. 4.6. To account for this, the position has to be corrected using equation 4.5 derived in [Hej98]

$$\Delta x = \frac{x}{L_{corr}} \quad \text{and} \quad y = \frac{y}{L_{corr}} \quad \text{where} \quad L_{corr} = \frac{s}{t_{max}} + 1 \quad (4.5)$$

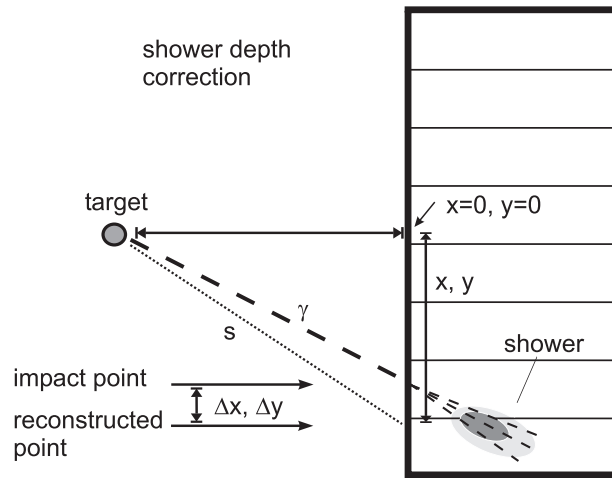


Figure 4.6: Shower depth correction in TAPS.

#### 4.4.2 TAPS particle identification

##### Pulse shape analysis

As seen in section 3.5.2, BaF2 crystals have two scintillation light components whose shape depends on the nature of the incident particle. Here, this property will be used to distinguish between baryons and electromagnetic particles. To achieve this, we take the two different ADC energy values determined using the long -  $2\mu\text{s}$  - and short -  $30\text{ ns}$  - integration times and, for each crystal, we plot  $E_{short}$  against  $E_{long}$ . An example can be seen in fig. 4.7a.

The short and long time gates have been calibrated for the photons<sup>5</sup> to appear on a  $45^\circ$  line. The protons, having a larger long component, form a line below the photon line. As both lines lay close to each other, the use of plots such as fig 4.7a to perform particle identification is awkward. This discrimination is more

<sup>5</sup>In the rest of this section, 'photon' stands for any electromagnetic particle and 'proton' for any baryon

efficient when using polar coordinates such as introduced in [Hej98] and refined in [Kot01] (fig. 4.7b).

$$R = \sqrt{E_{long}^2 + E_{short}^2} \quad \text{and} \quad \phi = \arctan\left(\frac{E_{short}}{E_{long}}\right) \quad (4.6)$$

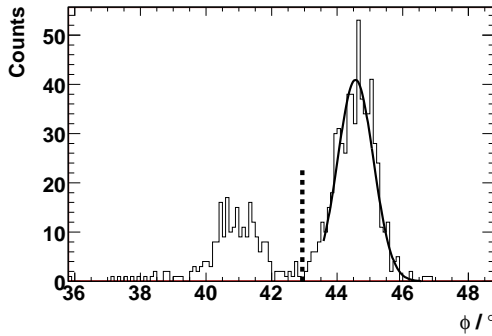


Figure 4.8: *Projection of fig. 4.7 on the energy axis for  $R = 360$  MeV. The data is fitted to determine the peak position and the  $3\sigma$  interval.*

In such plots, the two zones are much more distinct: a vertical zone at  $45^\circ$  corresponding to photons and a curved zone at smaller angles corresponding to protons can be easily told apart. The border between the two zones is determined by projecting such plots on the energy axis for 12 different values of  $R$ . These projections are then fitted by the sum of a Gaussian function and a first order polynomial to determine the peak position and the  $3\sigma$  interval. As an example, fig. 4.8 shows the fitting of the projection for  $R = 360$  MeV.

The distinction between protons and photons then is made by using the  $3\sigma$  values together with the polar coordinate plots. A particle above the  $3\sigma$  line (the dotted line on fig. 4.7b) is marked as a proton, below this line, it is a photon.

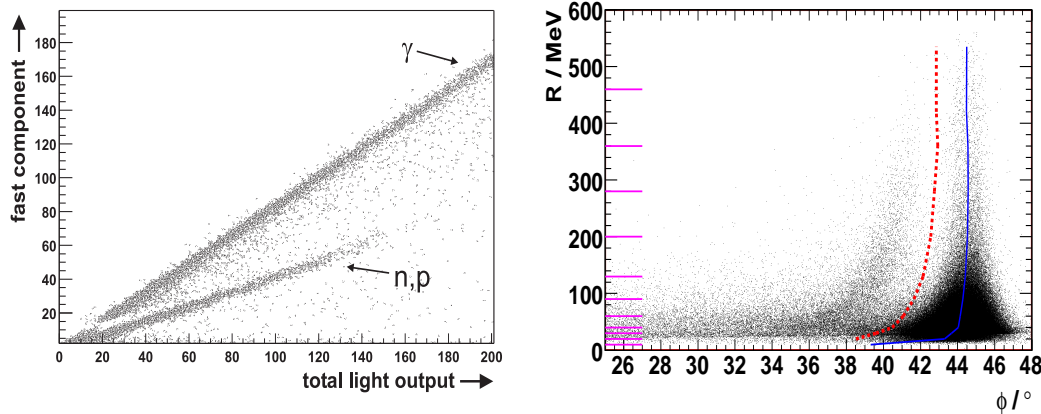


Figure 4.7: *Left: short gate versus long gate energy range. Right: representation in polar coordinates. The dashed line is the  $3\sigma$  border between the two zones (see text, taken from [Lug07]).*

### Time of flight

Due to the good time resolution of TAPS and the large distance -173.4cm - between the target and TAPS, a time of flight analysis is the more accurate way to identify particles. The time of flight can either be defined as the time difference between the tagger (the time at which the recoil electron is detected in the focal plane detector) and the time of the cluster in TAPS or as the difference between CB (average time of all CB clusters) and TAPS times. Both possibilities have been tested and give good results. Here, we will present with more detail the case where the Crystal Ball is selected as the time reference. The main reason for this choice is the absence of random background in the Crystal Ball.

This was done using the  $\vec{\gamma}p \rightarrow \pi^0 p$  reaction. Events with two photons in the Crystal Ball and a third particle (hopefully a proton) in TAPS were selected. The invariant mass of the two photons was computed to ensure that they effectively stem from a  $\pi^0$ . Then, the time difference between the cluster in TAPS and each of the two Crystal Ball clusters was then computed and plotted as a function of the TAPS cluster energy.

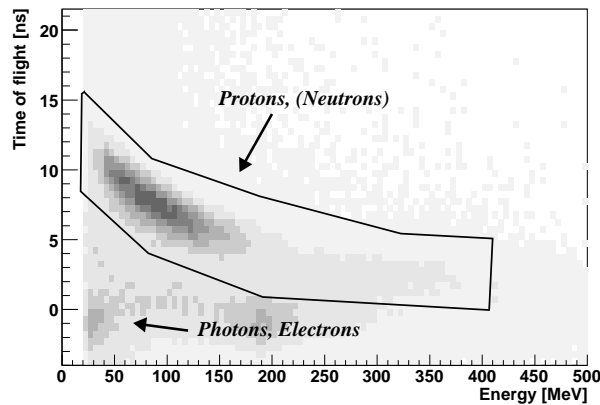


Figure 4.9: *Time difference between the assumed proton (in TAPS) and the two decay photons from  $\pi^0$  (in Crystal Ball) versus TAPS energy for  $\vec{\gamma}p \rightarrow \pi^0 p$ . A zone containing the protons (and possible background neutrons) appears and is delimited by the black curve. Background photons and electrons can also be seen.*

Results are presented in fig 4.9 and show a well defined curved zone corresponding to protons. Some photons or electrons from background reactions can also be seen at  $t = 0$ . The proton region is then fitted manually (black line) to define a cut to be used in subsequent analysis: a particle inside the delimited zone will be marked as a *time-of-flight* particle (i.e. a proton or a neutron). Every particle outside this zone remains *non time-of-flight* (a photon or an electron) <sup>6</sup>.

<sup>6</sup>This technique could in principle be used to identify  $\pi^+$ . However, tests have shown that

## Vetos

To distinguish between neutral and charged particles, one uses the yes/no information provided by the vetos. As the particle may come askew, the veto with the charged particle signal might not be in front of the central cluster. To avoid misidentification, a cluster is marked as *charged* if the veto in front of the central crystal or any of the first ring neighbours had recorded a charged hit.

## Particle identification decision

The nature of the detected particle is determined with a combination of the informations obtained by time-of-flight, PSA and the vetos. A discrimination between photons, electrons, protons and neutrons is possible and is summarized in table 4.2

Time of Flight	PSA	Veto	
non TOF	Electromagnetic	0	Photon
non TOF	Electromagnetic	1	Electron
TOF	Baryonic	1	Proton
TOF	Baryonic	0	Neutron
	<i>any other combination</i>		<i>Rootino</i>

Table 4.2: *Logical table for particle identification. A rootino is a particle whose nature couldn't be determined*

In the case of a discrepancy between time of flight and PSA informations, the nature of the particle is ambiguous and no arbitrary choice is made. This particle is kept in the code as an unidentified particle under the name of *rootino*.

## 4.4.3 Crystal ball particle identification

### MWPC track reconstruction

The multi wire proportional chambers are used to provide a better angular resolution for charged hadronic particles in the Crystal Ball. As already mentioned, an hadronic shower is much narrower than an electromagnetic shower. For this reason, a large fraction of the clusters corresponding to charged particles are made of one crystal only. In such a case, as no clusterization can be done, the position resolution in the Crystal Ball can't be smaller than the individual crystal size. The MWPC is designed to achieve a much better angular resolution for charged

---

when producing plots such as fig. 4.9 for reactions involving  $\pi^+$ , the pions appear in a wide zone between the proton and the photon zones which overlaps with them. An identification of the  $\pi^+$  with this method would be ambiguous and it has therefore been decided not to identify  $\pi^+$  with TAPS. Yet, this is not a serious issue since most of the  $\pi^+$  are emitted at angles covered by the Crystal Ball.

particles in the Crystal Ball. As presented in section 3.5.1, the MWPC consists of an inner and outer multi strips cathode and, in between, a multi wire anode. We will briefly present here how the information provided by these elements is used to reconstruct charged particles tracks.

In a first step, as a charged particle usually fires more than one strip or wire, all contiguous<sup>7</sup> hits are grouped to build clusters. For the anode wires, due to the yes/no structure of the output, the cluster position is simply the averaged position of all cluster members. For cathode strips, a weighting is done using the charge information of each strip provided by the sampling ADCs. In a second step, the inner and outer cathode clusters are combined to determine the charged hit position of the form  $(r, \phi, z)$ . The  $\phi$  information is provided directly by the position of the wire cluster. The  $z$  value is the one where the inner and outer cathode strips cross each other. However, as the strips always cross each other twice, this determination is not unique and a comparison with the wire position has to be done.

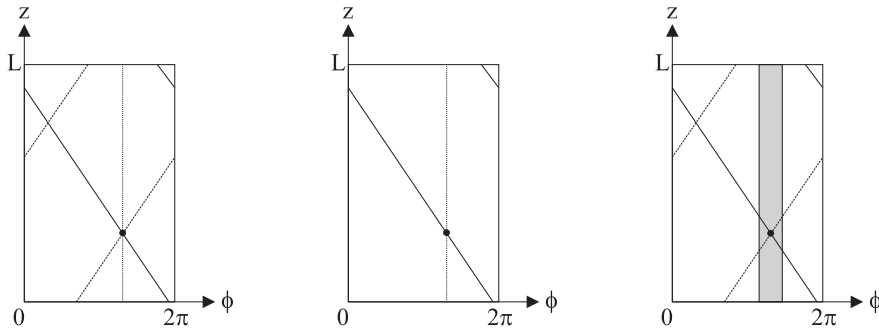


Figure 4.10: *Reconstruction of the interaction point in the MWPC. Left: In the ideal case, all three clusters from the inner and outer strip cathodes and from the wire anode are used to determine the hit position uniquely. Middle: When one strip is missing, the determination is still unambiguous. Right: If the wire information is absent, a PID element (shaded area) is used to rule out the wrong combination (taken from [Sch07]).*

As illustrated in fig. 4.10a we always get two values for  $\phi_{strip}$  so that  $\Delta\phi = |\phi_{wire} - \phi_{strip}| = 0^\circ$  (good) and  $180^\circ$  (bad). A cut ( $\Delta\phi < 0.1$  rad) is then applied to select the good combination. Once  $z$  and  $\phi$  are determined,  $r$  can be calculated knowing the geometry of the MWPCs. In some cases, it might be that the signal of one strip or of one wire is missing. If a strip is missing, the hit position can anyhow be determined uniquely using the other strip and the wire as can be seen in fig. 4.10b. If the wire information is missing, then a

<sup>7</sup>To avoid split-offs due to a single non-firing strip (or wire) inside a cluster, the minimal distance between two clusters has to be at least two strips (or wires)

corresponding hit in the PID is looked for. If a PID element has fired, it is used for an independent determination of  $\phi$ . By analogy with the ideal case, we have  $\Delta\phi_{PID} = |\phi_{strip} - \phi_{PID}| = 0^\circ$  or  $180^\circ$ . Events for which  $\Delta\phi_{PID} < 0.26$  rad are kept (see fig. 4.10c). Once this has been done for each wire chamber, the angular position of the charged particle is obtained by combining the informations from both MWPCs ( $\phi, \theta$ ).

$$\hat{v} = \frac{\vec{v}_1 - \vec{v}_2}{|\vec{v}_1 - \vec{v}_2|} \quad \text{where} \quad \vec{v}_i = (r_i, \phi_i, z_i) \quad (4.7)$$

For each obtained track, we look for a corresponding hit in the Crystal Ball. If the angular position of both hits in the CB and in the wire chambers fulfill equation 4.8, it is assumed that they are the signature of a charged particle. In this case, the Crystal Ball angular position ( $\phi_{CB}, \theta_{CB}$ ) is replaced by the track position ( $\phi_{MWPC}, \theta_{MWPC}$ ) which has a much better resolution

$$\sqrt{(\Delta\phi)^2 + (1.5\Delta\theta)^2} < 15^\circ \quad (4.8)$$

The resolution of the MWPCs is determined using cosmic muons and has been determined as  $\delta\phi = 1.35^\circ$  and  $\delta\theta = 1.88^\circ$ . The track reconstruction efficiency is measured for protons and  $\pi^+$  using  $\gamma p \rightarrow \pi^0 p$  and  $\gamma p \rightarrow \pi^+ n$  reactions. The charged particles were identified and reconstructed by the PID and the Crystal Ball and a corresponding track was looked for in the MWPCs. This method gives an efficiency on 89.7% for protons and 79.3% for  $\pi^+$ .

### PID 'banana plots'

As mentioned in section 3.5.1, the PID is used to determine the nature of charged particles in the Crystal Ball. The particles are identified using the energy they deposit in the PID scintillating elements, which depends on their nature.  $\pi^+$ , which can be approximated as minimum ionizing particles, deposit about 400 keV whereas the proton energy deposition ranges from 1 to 3 MeV depending on its energy. For each PID element, the energy of the charged particle is plotted against the total energy deposition in the Crystal Ball.

A total of 24 plots such as the one in fig. 4.11 are produced and show a clear separation between protons and  $\pi^+$ . Each of these plots show a zone at  $\Delta E \approx 400$  keV corresponding to  $\pi^+$  and a curved zone at higher energies corresponding to protons. Each zone is manually delimited by a polygon. Using this cut, particles inside the top zone are marked as protons and in the bottom zone as  $\pi^+$ . At lower energies, a peak of background electrons can be seen. As they also are

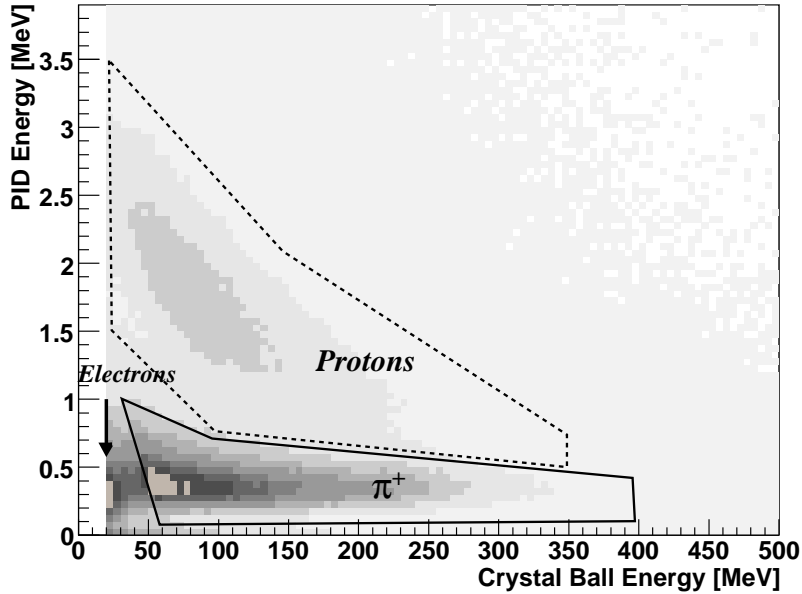


Figure 4.11: *PID versus Crystal Ball energy deposition for charged particles. Protons and  $\pi^+$  zones are fitted with the dashed and solid lines respectively. Low energetic electrons can also be seen. Such plots are commonly referred to as 'Banana Plots'.*

minimum ionizing particles, they appear close to the  $\pi^+$  zone which has to be carefully fitted to exclude these electrons.

As a final remark, let's note that there is no way to identify the nature of neutral particles in the Crystal Ball. This makes the direct detection of the neutron impossible. In the code, all neutral particles are by default marked as photons.

## 4.5 Random subtraction

During data taking, the beam intensity was usually high enough for a large number of background electrons to be detected in the tagger along with the bremsstrahlung electron. We have seen that the photon energy is determined by  $E_\gamma = E_{beam} - E_{e^-}$ . If more than one electron is detected, this high multiplicity creates an ambiguity in the photon energy determination as we don't know which one of the detected electrons actually produced the bremsstrahlung photon in the radiator. In order to distinguish between the good (usually called *prompt*) and all other background electrons (or *random*) we use the time of flight between the tagger and the two detectors. To do this, for each electron detected in the tagger, we compute the time difference  $\Delta t = t_{e^-} - t_{detectors}$  where  $t_{detectors}$  is the average

time of all photons detected in TAPS and in the CB for the event. The results are shown in fig. 4.12.

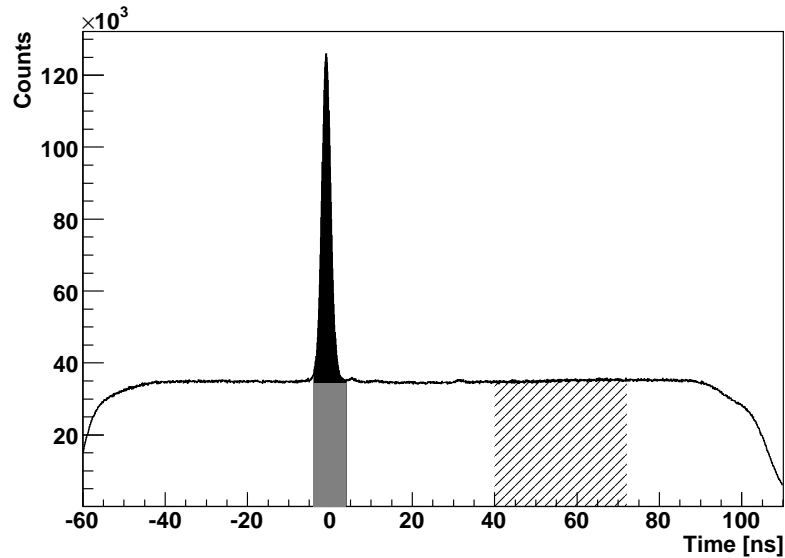


Figure 4.12: *Time difference between the electrons and the tagger for double  $\pi^0$  channel. The zones used for random background subtraction are highlighted.*

In this so-called *coincidence plot*, the three necessary zones needed to perform this random subtraction have been highlighted. In the zone centered at zero, the prompt electrons appear in the black zone while the random electrons appear in the gray zone. As both contributions can't be distinguished with a simple cut on the time of flight, a third (striped) zone is defined far away from the prompt peak, where it's sure the detected electron was a random electron. These zones are then used to produce background free plots. Any variable involving the photon energy is plotted twice. A first plot is produced for electrons appearing in the central zone, containing both prompt and random contributions together with a second plot with electrons in the striped zone, containing background contribution only. Both plots are then scaled to account for the relative width of the two zones and are eventually subtracted, thus getting rid of random background. As an illustration, fig. 4.13 shows the removal of the random background in the determination of the proton missing mass (see section 6.1.1).

## 4.6 Tagging efficiency

In order to determine normalized cross sections, one needs to know the number of photons impinging on the target. In our case, the diamond radiator is thin enough to make the probability of multiple electron interaction negligible, therefore, the

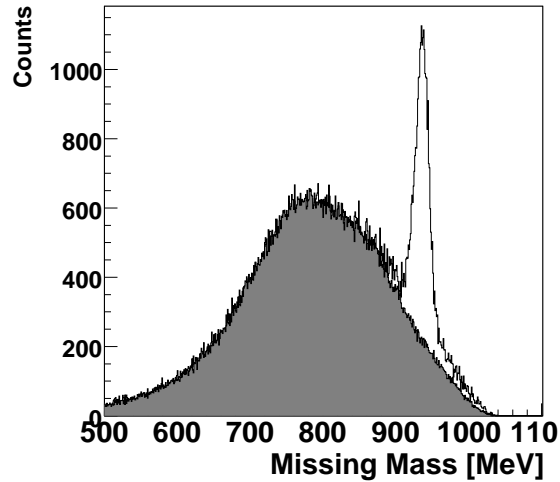


Figure 4.13: *Example of random background subtraction. White: Missing mass corresponding to electrons from the prompt peak region, containing prompt and random contributions. Gray: Missing mass corresponding to background electrons only. Outside the physically meaningful region, both curves match perfectly. The subtracted result can be seen in fig 6.2c.*

number of photons reaching the target should, in the ideal case, be equal to the number of scattered electrons detected in the tagger. As some photons get lost on their way from the radiator to the target, mostly due to collimation, it is useful to define the tagging efficiency as the probability for a bremsstrahlung photon to reach the target.

$$\epsilon_{tagg} = \frac{N_{\gamma}}{N_{e^{-}}} \quad (4.9)$$

The tagging efficiency was estimated approximatively daily with dedicated measurements.  $N_{e^{-}}$  was determined for each channel using the ladder scaler. The number of photons reaching the target was determined with a special Čerenkov Pb glass detector, large and thick enough ( $> 20 X_0$ ) to avoid photon escape, placed in the beam line and used as the stop signal for the tagger TDCs. The tagging efficiency measurements were performed with a beam intensity low enough for the Pb glass not to saturate. Using such a low intensity, the random background in the ladder is negligible and each detected photon can be associated with an electron in the tagger without ambiguity. Before and after each tagging efficiency measurement, the background activity was recorded for ten minutes without any beam. Combining all this, the tagging efficiency is computed channel-wise using

$$\epsilon_{tagg}[i] = \frac{N_{\gamma}[i]}{N_{e^{-}}[i] - \frac{t}{t_{back}} N_{e^{-}}^{back}[i]} \quad (4.10)$$

were  $t_x$  is the duration of the tagging efficiency measurements and  $i$  runs over all tagger channels. When measuring tagging efficiency after long production runs, the background activity was noticeably higher, coming back to a constant value after  $\sim 5$  minutes. For this reason, only background data taken after each tagging efficiency measurement were used to determine  $\epsilon_{tagg}$ .

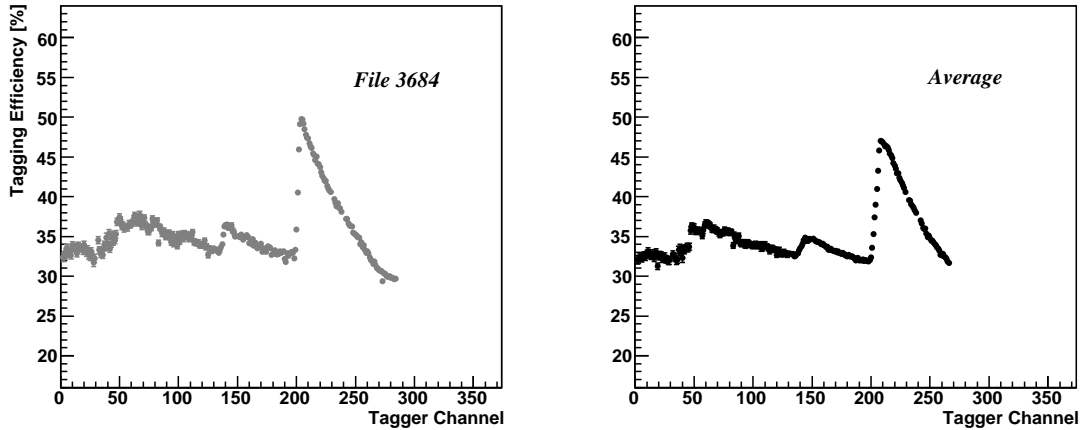


Figure 4.14: *Tagging efficiency as a function of tagger channel. Left: one sample file. Right: average for the complete July beamtime.*

Fig. 4.14a shows the tagging efficiency for one sample file. Between channels 200 and 250, the tagging efficiency shows a large peak, about 50 % higher than the average value at higher energies. In section 3.2, we have seen that the coherent bremsstrahlung photons are more forward peaked than those produced by incoherent bremsstrahlung. The probability to lose linearly polarized photons in the collimator is then smaller than for unpolarized photons. An enhancement of the tagging efficiency in the coherent edge region thus appears. This is treated completely in [Ram98].

Altogether, the tagging efficiency was measured 53 times during the complete experiment. As the conditions might change during data taking the evolution of the tagging efficiency in time has to be taken in account. This is simplified by the fact that the shape of the tagging efficiency as a function of the energy is very stable. Only the absolute value has to be cared of. A good approximation of the overall tagging efficiency is obtained by averaging all individual measurements from a complete beamtime (fig. 4.14b). Still, the tagging efficiency was only measured periodically, approximatively once a day. This leaves room for fluctuations between two consecutive determinations. To account for this, a method described in [Kot01] will be applied to our experiment. A ionization chamber - called P2 - was placed behind the target to measure the beam intensity. During

the runs, the ratio between the counting rates in P2 and in the tagger was continuously monitored. This P2/tagger ratio is proportional to  $\epsilon_{tagg}$ . As shown in fig. 4.15, it is scaled to match the individual tagging efficiency measurements and then integrated over the whole time range. The result of this integration is then used to correct the average value from fig 4.14b. It can be however noticed that this P2/tagger ratio is very stable so that the correction to apply always remains below 1%.

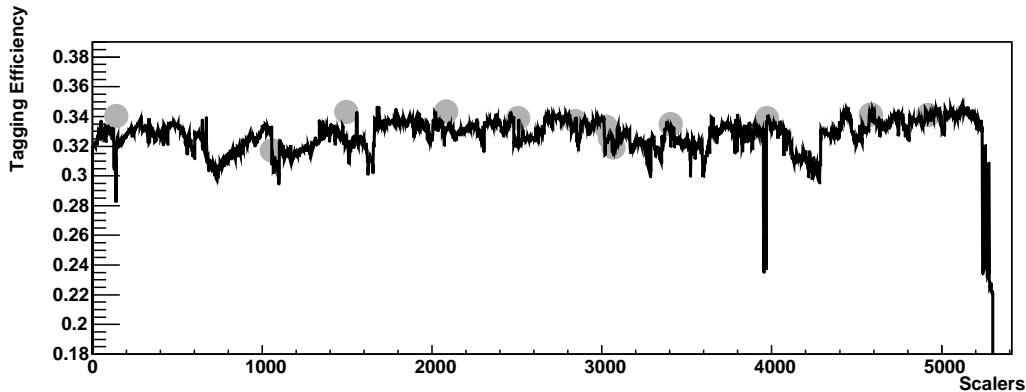


Figure 4.15: *Averaging of tagging efficiency. The ratio P2/Tagger (black line) is compared to the individual measurements (gray dots).*

## 4.7 Credits

All the calibrating techniques presented in this chapter involved long and hard work. In order to optimize the available manpower, the work was divided among the PhD students of the A2 collaboration. Each student was responsible for a specific task for the complete round of experiment, even for beamtimes that were not related to the subject of his thesis. Once this was done, the calibration files were put in a common directory in one of the MAMI computers and anyone could retrieve the calibration corresponding to his work. Detailed information on these calibrations can be found in the thesis written by these nice people.

- Jason Brudvik from Los Angeles and Marc Unverzagt from Mainz performed the Crystal Ball energy calibrations [Bru07], [Unv08]. The time alignment and walk correction were performed by Dirk Krambrich from Mainz [Kra07].
- Evie Downie from Glasgow designed the methods to calibrate the PID and to identify particles in the Crystal Ball [Dow07]. Richard Codling from Glasgow carried them out and also aligned the tagger time [Cod08].

- Alexander Nikolaiev from Mainz analyzed the tagging efficiency measurements [Nik07], [Nik08].
- Sven Schuman from Mainz took care of the MWPC calibrations [Sch07].
- Stefan Lugert and Ralf Gregor from Gießen calibrated the pulse shape analysis and implemented the particle identification scheme for TAPS [Gre07], [Lug07].
- Benedicte Boillat from Basel performed TAPS energy calibrations with cosmic muons [Boi08]. TAPS time calibrations and the clustering routine were done by the author.

## 5 Simulations

*As mentionned in chapter 3, our detector has been designed to provide a complete  $4\pi$  solid angle coverage so that every single event gets observed. Reality is of course slightly off the ideal case and, for different reasons, some events might escape detection. A final state particle might get lost, in most cases due to its low energy, below the detector threshold. It might also be that a particle escapes through the forward or backward beam holes in TAPS and Crystal Ball. An event will also be rejected if it doesn't fulfill the trigger conditions, if one of the particles gets misidentified or if it fails to satisfy any of the cuts applied in the software analysis (see chapters 3, 4 and 6). For all these reasons, the number of detected events won't be equal to the number of events actually produced in the target. In order to calculate fully normalized cross sections, it is important to assess this event loss, usually referred to as the detecting efficiency, as precisely as possible with a dedicated computer simulation. In this chapter, we will first present how a simulated model of our detector is constructed using CERN's GEANT software. We will then describe how the physical events are generated and finally, we will move to the specific case of double pion production and show how the efficiency for the double  $\pi^0$  and the  $\pi^0 \pi^+$  channels is determined.*

### 5.1 Detector simulation

Knowing the performances of a detector is a recurrent concern to every physical experiment involving the detection of particles. The GEANT (GEometry ANd Tracking) toolkit was developed early in CERN history<sup>1</sup> (1974) to allow a precise simulation of the detectors. Simulating the behaviour of a detector with a GEANT based program is a two-step work. First, the virtual detector is build by describing the geometry of its elements in terms of dimension, position and material. This doesn't only concern the detector itself but any of the elements - e.g. sustaining structure, cables, electronics - that could affect the particles behaviour

---

<sup>1</sup>GEANT was first designed to fulfill high energy physics needs but its use has widely spread through fields where particles get detected: nuclear, hadronic and reactor physics, astrophysics and even medical engineering.

(this is the *geometry* part of the job). Once this is done, a set of generated particles is passed to the simulated detector. GEANT simulates the interaction of these particles with matter in any traversed element and calculates the deposited energy in the detector. Any other relevant value, such as the detection time can also be simulated (*tracking*).

Simulations of the Crystal Ball and TAPS have a long history, having been created together with the detectors and evolved along with them. When the new round of experiments started at MAMI, detailed and reliable software were already available for both Crystal Ball and TAPS. As the Crystal Ball geometry was by far the most complex, it was decided to base the new simulation on the software previously developed by the Crystal Ball collaboration, referred to as *cbsim*. *Cbsim* was a GEANT<sup>2</sup> 3.21 program that featured a complete description of the Crystal Ball as it was used at its previous location at SLAC. In an early step, TAPS geometry was added to it in a basic way by UCLA people. Then, along with data taking, *cbsim* was progressively improved and all the elements presented in chapter 3 were added. The PID, the MWPC and TAPS vetos were added. TAPS geometry was greatly improved, Crystal Ball geometry was updated and the solid target geometry was implemented. All these improvements were performed by E. Downie, V. Kashevarov, S. Schumann, M. Unverzagt and S. Lugert. More details about this can be found in the latter's thesis [Lug07].

## 5.2 Event generation

As mentioned, GEANT calculates the interaction between any particle and the simulated detector. But it is left to the user to provide a start distribution describing the studied physical process in an accurate way. For the generation of double pion events, it has been decided to use a simple phase space event generator. The motivations for this choice can be found in the kinematics of the  $\gamma p \rightarrow p\pi^0\pi^0$  reaction<sup>3</sup>. In such a three body decay, the kinematics are described by 12 variables, 4 for each particle. Not all of these variables are independent though: 3 are set by the particle masses and 4 by the energy and momentum conservation. The start distribution has then to be described in the 5-dimensional space generated by any convenient choice of five independent variables.

Generating a phase space distribution consists in the choice of an appropriate

---

<sup>2</sup>GEANT 3.21 is FORTRAN based and is no longer maintained by CERN. The most up to date version is the C++ based GEANT4. In the first stage of CB@MAMI experiments it has been chosen to keep the pre-existing *cbsim* as a basis. The building of a new reliable GEANT4 simulation from scratch would have required too much time. Recently, a first version of a GEANT4 simulation giving very good results [GlaPr], [BruPr] has been released by the University of Glasgow. This GEANT4 program was not used in this work.

<sup>3</sup>The arguments are the same for the  $\gamma p \rightarrow n\pi^+\pi^0$  reaction.

set of five independent variables. The value for each variable is then set randomly. This is the simplest and the more reasonable technique to use. Any other method than a phase space distribution would be a tedious and unnecessary work. A physically accurate event generation complying with one of the theoretical models presented in chapter 2 -which include up to 25 Feynman diagrams contributions- would be a very long job. Another method to account for deviations from phase space which doesn't imply any initial knowledge of the start distribution is commonly used for single  $\pi^0$  photoproduction. In this technique, a first phase space distribution is generated, simulated and analyzed. The results are then compared to the data. If both data and simulation disagree, a weighting factor is calculated and applied to the generated distribution. The weighted distribution is then analyzed again. This procedure is repeated iteratively until both simulations and data match each other (see [Kru95]). This method is easy to carry out for single meson photoproduction since the reaction is only described by one kinematical variable. For double pion production, it would be much harder to carry out since it implies a similar fitting of the data in a 5-dimensional space.

In order to evaluate the validity of the approximation of the use of a phase space distribution, we compute the  $\theta$  angle and the kinetic energy of the two pions. The result for both simulation (thick line) and data (thin) is shown in fig 5.1. As the agreement between both curves is good one can assume that no big systematic error is introduced in the efficiency determination by the use of a phase space distribution. The main one could be the fact that the correlations between two particles (studied with invariant mass distributions, see section 7.5) are not taken into account. But due to the homogeneous  $4\pi$  angle coverage of detector, this is not expected to introduce a large experimental bias in our results. The writing of an event generator for a phase space decay is an easy task, simplified by the use of a pre-defined decay routine provided e.g. by GEANT or ROOT. In this work, we used the event generator provided by the Crystal Ball collaboration called *mkln* as well as *mcgen*, the event generator from AcqRoot.

### 5.3 Efficiency determination

The efficiency is determined as a function of the incoming photon energy. For a set<sup>4</sup> of 242 beam energies corresponding to the tagger channels above threshold, 50'000 events were generated. The efficiency of the detector is estimated by computing the ratio between the number of reconstructed and generated events  $\epsilon(E_\gamma) = N^{reconstructed} / N^{generated}$  for each incoming photon energy. The values are then plotted as a function of the energy and fitted with a polynomial function to

---

<sup>4</sup>Only 241 for  $\gamma p \rightarrow n\pi^+\pi^0$  as the threshold is slightly higher

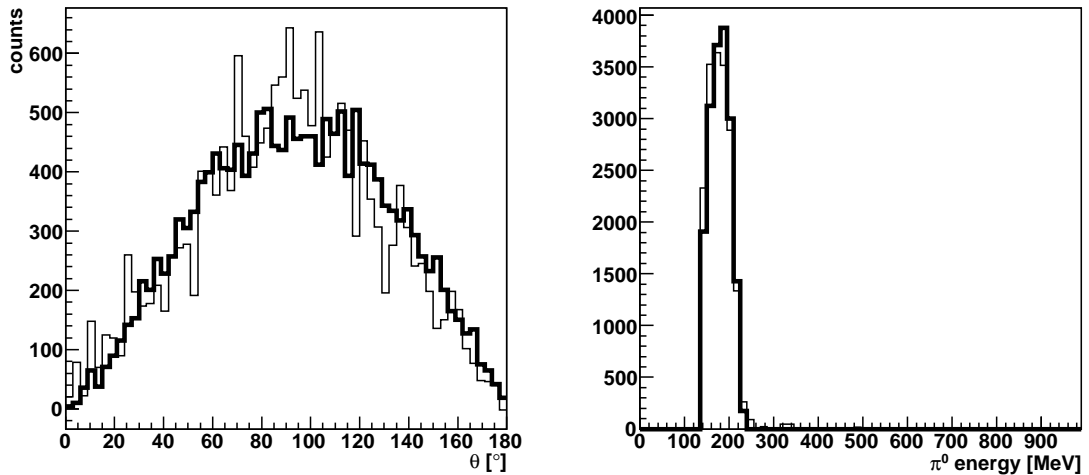


Figure 5.1:  $\pi^0$  theta angle (left) and energy (right) in the center of mass for energies between 430 and 450 MeV. The simulation (thick line) is compared with the data (normal). The agreement between the two curves accounts for the use of a phase space event generation.

smooth out the fluctuations. The results of this method are presented individually for each channel in the following.

### 5.3.1 $\gamma p \rightarrow p\pi^0\pi^0$ efficiency

Fig 5.2 shows the detection efficiency for the  $\gamma p \rightarrow p\pi^0\pi^0$  reaction as a function of the incoming photon energy. For this reaction, the efficiency remains fairly stable over the whole energy range, between 35 and 55%. The use of a  $\sim 4\pi$  detector ensures that the kinematics of the reaction doesn't have a major influence on the shape of the efficiency. Even at energies close to threshold ( $E_\gamma = 315 - 350$  MeV) the efficiency remains very high. At such low energies, all three final state particles come out with a very low momentum. This doesn't influence the detecting efficiency of each of the two  $\pi^0$  which decay rapidly into two photons and are reconstructed by invariant mass analysis. The proton, on the contrary, will almost never have an energy large enough to produce a signal above the detection threshold and will thus get lost. Still, we will show in chapter 6 that this is not a problem since the detection of the proton is not necessary to identify the double  $\pi^0$  channel. The detection efficiency will therefore remain high very close to threshold allowing for a very precise determination of the cross section in this energy region.

This plot is a nice illustration of the benefits resulting from the use of a  $4\pi$  detector for reaction channels with a large number of particles in the final state. Here, the efficiency between 0.35 and 0.55 ensures that more than one out of three

produced  $\pi^0 \pi^0$  events are detected. As a comparison, the previous experiments on double  $\pi^0$  at MAMI [Wol00], [Kot01] that used a detector covering 37% of the solid angle had an efficiency smaller by two orders of magnitude, losing more than 99.5% of the total number of events.

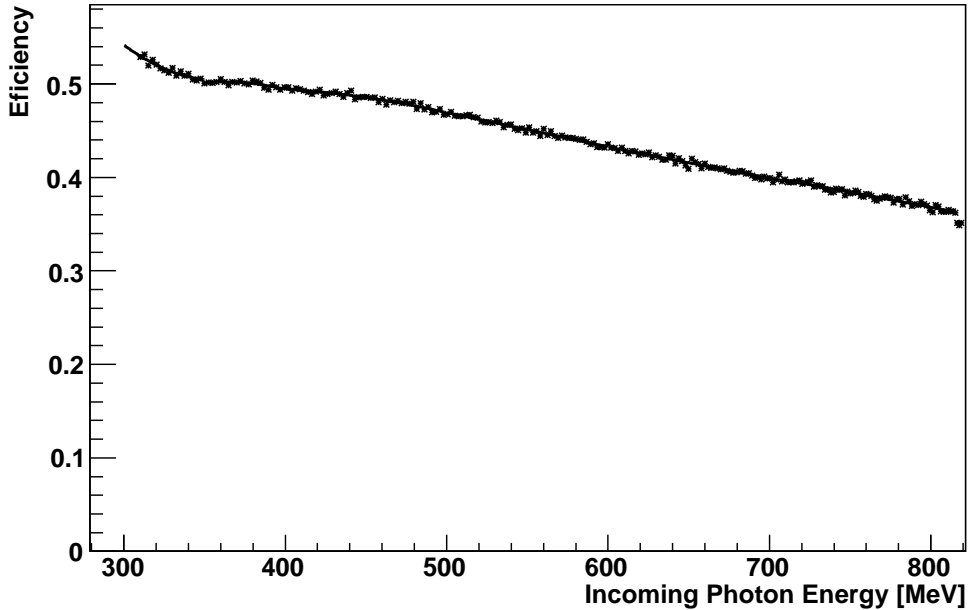


Figure 5.2: *Detection efficiency for the  $\gamma p \rightarrow p\pi^0\pi^0$  channel as a function of the incoming photon energy.*

### 5.3.2 $\gamma p \rightarrow n\pi^+\pi^0$ efficiency

Fig 5.3 shows the efficiency for the  $\gamma p \rightarrow n\pi^+\pi^0$  channel. The main difference with the double  $\pi^0$  case is the sharp drop at low energies. As mentioned, at energies just above threshold, all three final state particles come out with a very small momentum. In the case of  $\gamma p \rightarrow n\pi^+\pi^0$  the lifetime of the neutron and of the  $\pi^+$  is long enough for them to reach the detectors. Their energy being too low to trigger a signal in the crystals, they will, in most cases, escape detection. The only particle that gets detected in this case is the  $\pi^0$ , rapidly decaying into two photons. If both  $\pi^+$  and neutron get lost, only two clusters will be reconstructed and the event will be rejected by the trigger. At low energies, most of the  $\gamma p \rightarrow n\pi^+\pi^0$  events will therefore get lost, making the efficiency very low. A precise determination of the  $\gamma p \rightarrow n\pi^+\pi^0$  cross section in this energy region will unfortunately not be possible.

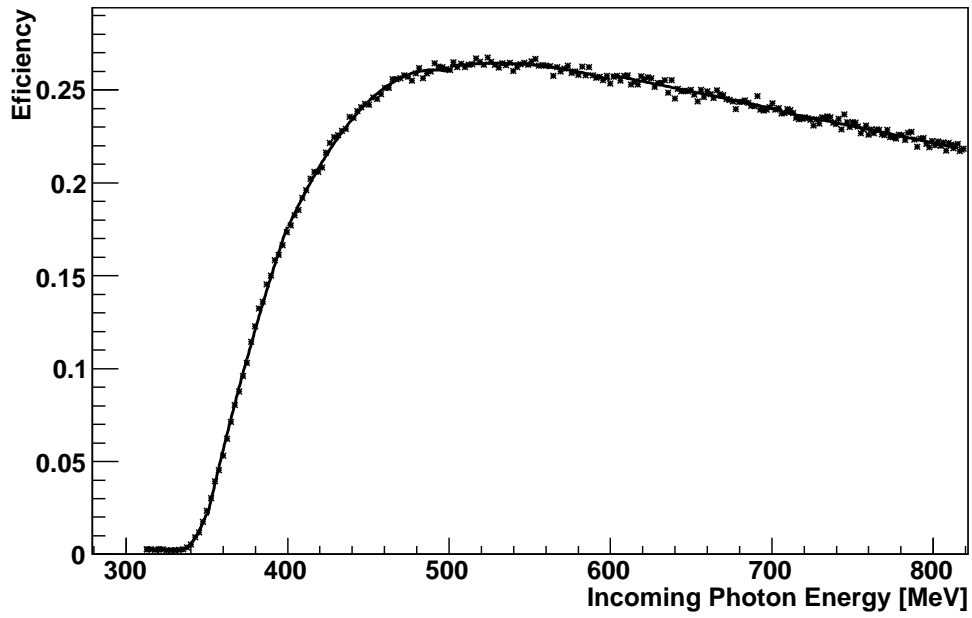


Figure 5.3: *Detection efficiency for the  $\gamma p \rightarrow n\pi^+\pi^0$  channel as a function of the incoming photon energy.*

# 6 Data analysis

*Calibrated using the methods presented in the previous two chapters, the data are now ready to be analyzed and to produce physical results. In this chapter, we will explain how significant quantities such as cross sections, Dalitz plots and asymmetries are defined and can be computed in our framework. We will then show the most significant results that will be used in chapter 7 to compare our results with the theoretical calculations presented in chapter 2.*

## 6.1 Cross sections

The cross section is given by the formula

$$\sigma = \frac{N_x}{N_{e^-} \epsilon_{tagg} \epsilon_{det} N_{target} \Gamma_{X \rightarrow Y}} \quad (6.1)$$

where  $N_x$  is the absolute number of reconstructed events and the denominator factors allow the normalization of  $\sigma$  to the conditions of the experiment. They are accounted for in the previous chapters.

- $N_{e^-}$  is the number of electrons measured by the tagger. (see section 3.3)
- $\epsilon_{tagg}$  is the tagging efficiency. (4.6)  
therefore  $N_{e^-} \epsilon_{tagg}$  corresponds to the photon flux impinging on the target.
- $\epsilon_{det}$  is the overall detector efficiency. (5.3)
- $N_{target}$  is the number of protons in the target. (3.4)
- and  $\Gamma_{X \rightarrow Y}$  the branching ratio of the studied channel into the measured decay products<sup>1</sup> [PDG06].

---

<sup>1</sup>In our case  $\Gamma_{p\pi^0\pi^0 \rightarrow p\gamma\gamma\gamma\gamma} = \Gamma_{\pi^0 \rightarrow \gamma\gamma} \Gamma_{\pi^0 \rightarrow \gamma\gamma} = 0.976$  for the double  $\pi^0$  channel and  $\Gamma_{n\pi^0\pi^+ \rightarrow p\gamma\gamma\pi^+} = \Gamma_{\pi^0 \rightarrow \gamma\gamma} = 0.988$  for the  $\pi^0 \pi^+$  channel

### 6.1.1 Identification of double $\pi^0$ events

#### Invariant mass analysis

Double  $\pi^0$  events were detected via their decay into 4 photons by reconstructing the invariant mass of each pion pair using

$$m_{inv}^2 = (P_{\gamma_1} + P_{\gamma_2})^2 = (E_{\gamma_1} + E_{\gamma_2})^2 - (\vec{p}_{\gamma_1} + \vec{p}_{\gamma_2})^2 \quad (6.2)$$

Since the 4 final state photons are undistinguishable, a direct reconstruction of each  $\pi^0$  is not possible. In order to assign each photon to the corresponding pion, all possible combinations of photon pairs have to be tested. To do this we define

$$m_{diff} = |(m_{\gamma_i\gamma_j} - m_{\pi^0})^2 + (m_{\gamma_k\gamma_l} - m_{\pi^0})^2|. \quad (6.3)$$

The value of  $m_{diff}$  is computed for all values of  $i, j, k, l = 1, 2, 3, 4; i \neq j \neq k \neq l$  and the best pion pair corresponding to the minimal value of  $m_{diff}$  is selected.

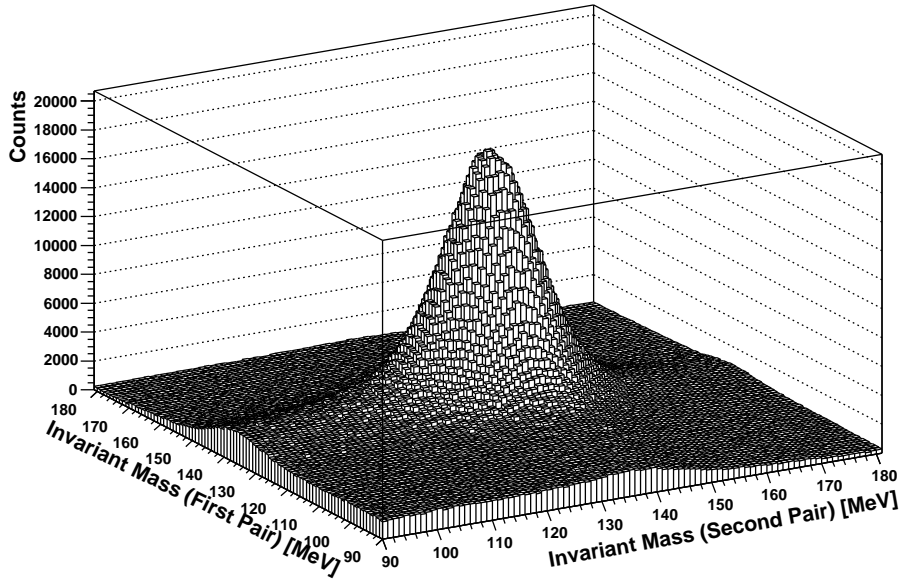


Figure 6.1: 2-dimensional invariant masses of the reconstructed  $\pi^0$  pairs.

Fig. 6.1 is a 2-dimensional view of the invariant mass of these selected pion pairs. For each event, the values of  $m_{ij}$  and  $m_{kl}$  corresponding to the minimal value of  $m_{diff}$  define an entry into the plot. A cut on the invariant mass is then applied: events for which at least one  $\pi^0$  has an invariant mass value outside of the range [100,160] MeV are rejected. Once this cut is applied, the energy resolution can be improved by fitting the energies of the photon to the mass of the  $\pi^0$ . To do

this, we apply the so-called X-formula which sets the invariant mass of the pion pairs to  $m_{\pi^0}$ :

$$P_{\gamma\gamma} \rightarrow \frac{m_{\pi^0}}{m_{\gamma\gamma}} P_{\gamma\gamma} \quad (6.4)$$

In a  $\gamma p \rightarrow p\pi^0\pi^0$  event, the recoil proton can also be detected. At low incoming photon energies, it is however likely that the energy of the proton is too low to allow its detection. To account for this, events with 4 photon clusters and 1 additional proton cluster (*detected proton*) were taken in account together with events made of 4 photon clusters only (*lost proton*).

### Missing mass analysis

To ensure that the selected  $\pi^0$  pair really originates from a  $\gamma p \rightarrow p\pi^0\pi^0$  event and separate it from background channels (mainly due to  $\eta \rightarrow 3\pi^0$  where two of the six decay photons are lost) we calculate the missing mass defined by

$$\begin{aligned} m_{miss}^2 &= (P_{beam} + P_{target} - P_{\pi_1^0} - P_{\pi_2^0})^2 \\ &= (E_\gamma + m_p - E_{\pi_1^0} - E_{\pi_2^0})^2 - (\vec{p}_\gamma - \vec{p}_{\pi_1^0} - \vec{p}_{\pi_2^0})^2 \end{aligned} \quad (6.5)$$

For a good double  $\pi^0$  event,  $m_{miss}$  has to be equal to the mass of the proton. Fig. 6.2 shows the missing mass as a function of the incoming photon energy. For each of the six incoming energy bins, a nice peak can be observed as a unique signature of the low background identification of double  $\pi^0$  events. In order to reject the small remaining background an energy dependant cut has to be applied. At each energy the peak was fitted with a Gaussian distribution and a  $3\sigma$  cut was applied. This cut is represented by the vertical thick lines in fig. 6.2.

The good statistics, low background data obtained here are a striking evidence of the benefits of a  $4\pi$  solid angle detector. At energies just above threshold ( $E_{beam} < 350$  MeV, top left) around 200 events are reconstructed, even though the cross section in this energy region is of the order of a few nanobarns only. This ensures a very precise energy of the  $\gamma p \rightarrow p\pi^0\pi^0$  reaction close to threshold. At the opposite side of the energy range, ( $E_{beam} > 707$  MeV =  $E_{thresh}^\eta$ , bottom right) the background due to  $\eta \rightarrow 3\pi^0$  where a  $\pi^0$  gets lost is very small. In the previous double  $\pi^0$  experiments this background was a strong limiting factor for the precision of the cross section. It appeared as a huge peak at  $m_{mass} > m_{proton}$  and strongly contaminated the results at energies above the eta threshold.

### 6.1.2 $\gamma p \rightarrow p\pi^0\pi^0$ Cross Section

Using formula 6.1 with  $N_x$  as the total number of events that passed the invariant mass and missing mass cuts, we compute the total cross section for the

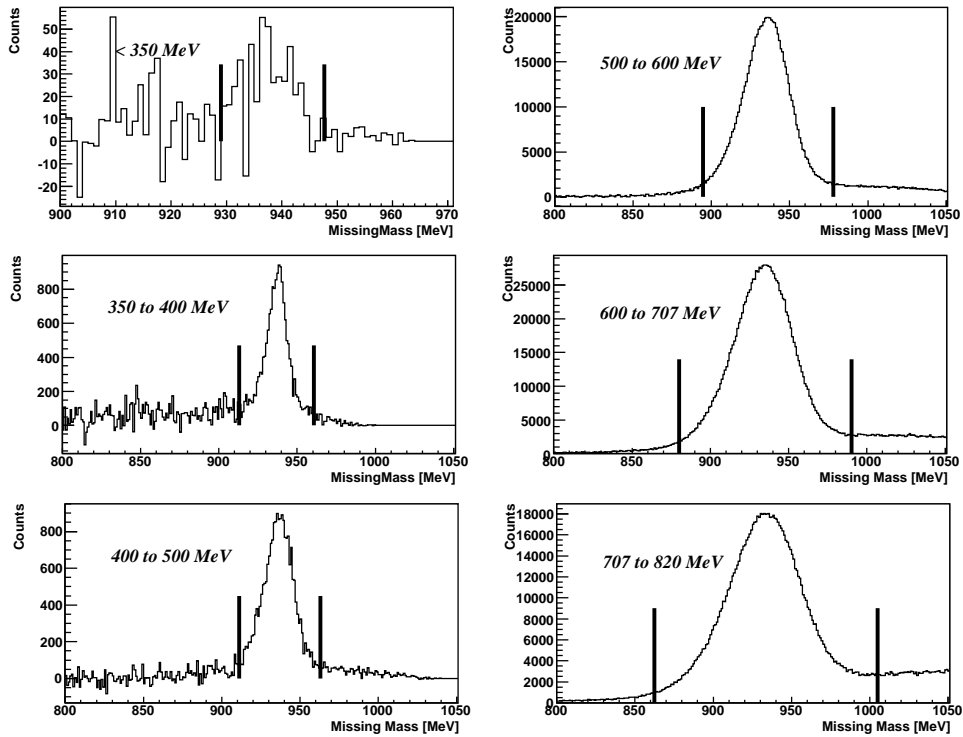


Figure 6.2: Missing mass for different incoming photon energy bins. The good events show a peak at  $m_{miss} = m_{proton}$ . The peak is fitted with a Gaussian distribution and a  $3\sigma$  cut is applied.

$\gamma p \rightarrow n\pi^+\pi^0$  reaction. Fig. 6.3 shows this cross section for the three different beamtimes over the complete energy region as well as for the complete data set. Fig. 6.4 shows the same results zoomed over the threshold region. In the threshold region, all beamtimes agree quite well. At higher energies, especially in the region where the cross section is maximal ( $E_\gamma > 700$  MeV), there is some discrepancy between the July beamtime and the other ones. This can be explained by the large systematic error for this beamtime due to the presence of ice on the target exit window and the lack of empty target measurement (see appendix B). For a further interpretation of these results, see section 7.1

A careful reader might notice a few 'holes' in the cross section, as in fig. 6.4 for  $E_\gamma = 337$  and  $340$  MeV. Such missing points correspond to tagger channels whose information is missing or was not recorded correctly. These dead channels have been systematically removed from our results.

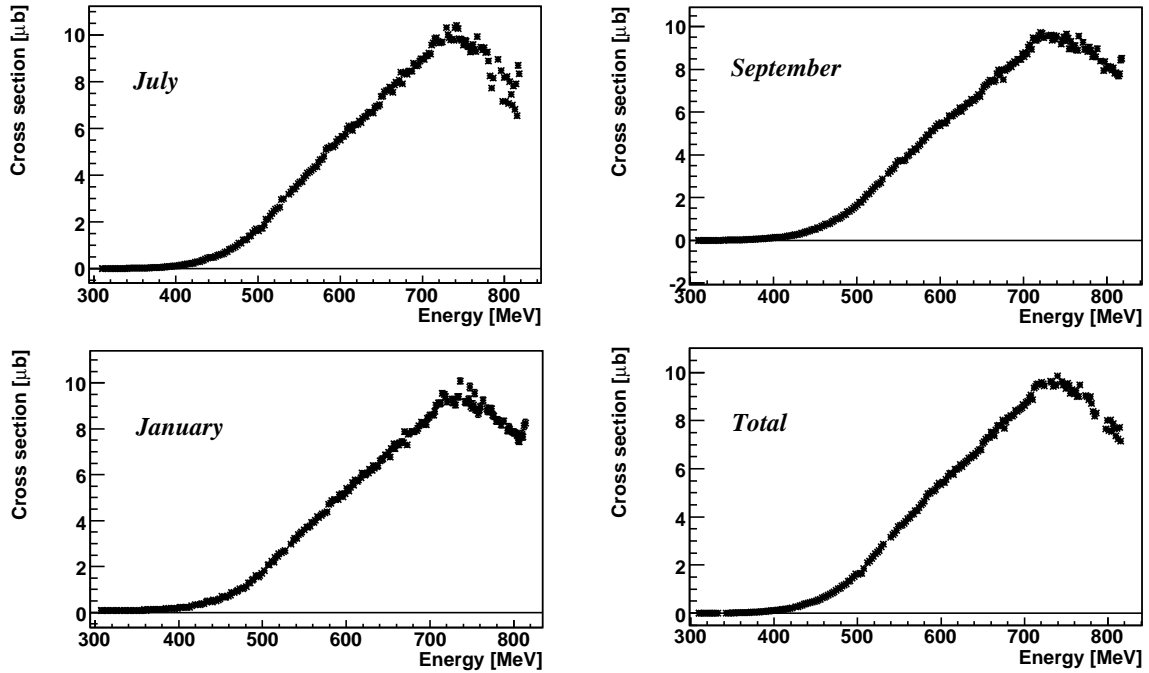


Figure 6.3: Cross section for the  $\gamma p \rightarrow p\pi^0\pi^0$  reaction for the different beamtimes and for the complete data set.

### 6.1.3 Identification of $\pi^0 \pi^+$ events

#### Invariant mass analysis

The methods used to identify  $\pi^0 \pi^+$  events are similar to the ones used for double  $\pi^0$ . When a  $\gamma p \rightarrow n\pi^+\pi^0$  event is produced, the final state particles are the two  $\pi^0$  decay photons, the  $\pi^+$ , whose lifetime is long enough to reach the detectors and the recoil neutron. To reconstruct this reaction, we selected events with two photon clusters and one  $\pi^+$  cluster. The neutron<sup>2</sup> could either be detected (2 photons, one  $\pi^+$  and one additional neutron cluster) or lost (2 photons and one  $\pi^+$  only).

The invariant mass of the  $\pi^0$  was reconstructed from the two decay photons using eq. 6.2. As expected (no background channel can add a significative contribution at this point) fig. 6.5 shows a very clean identification of the  $\pi^0$ . As in the double  $\pi^0$  case, a cut on the invariant mass (between 115 and 160 MeV) is applied and the energy of the photons is fitted using eq. 6.4 so that  $m_{\gamma\gamma} = m_{\pi^0}$ .

<sup>2</sup>The detecting efficiency of the neutron is  $\sim 30\%$  in TAPS while in the Crystal Ball, neutron identification isn't possible

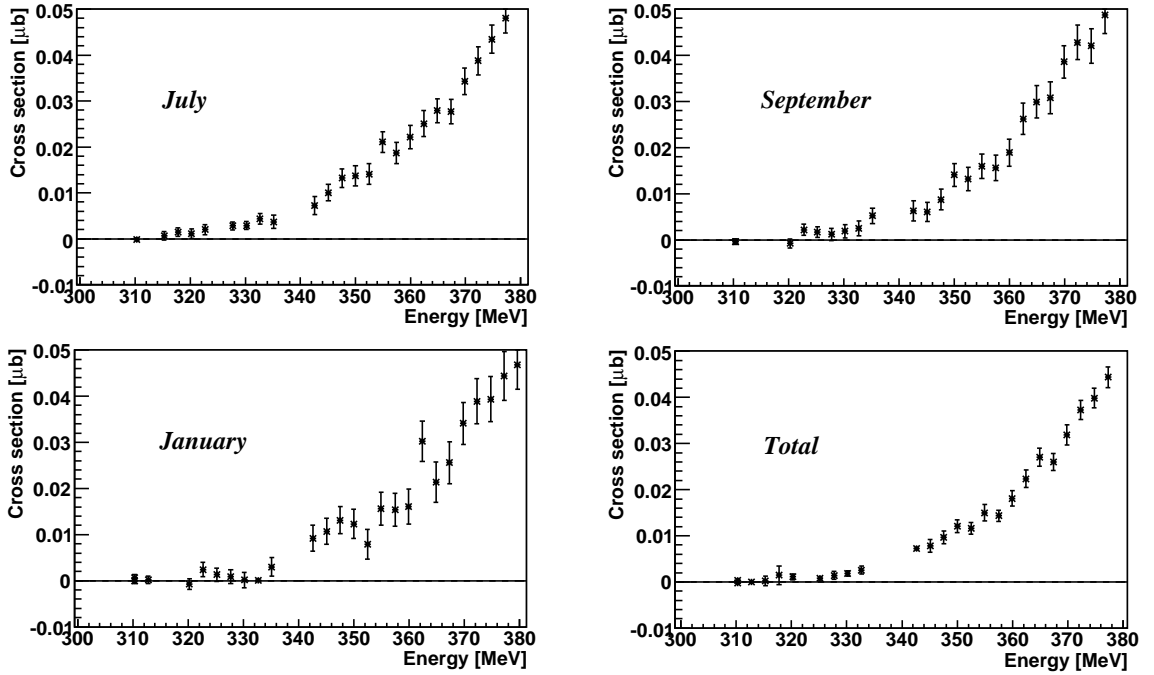


Figure 6.4: Cross section in the threshold region for the  $\gamma p \rightarrow p\pi^0\pi^0$  reaction for the different beamtimes and for the complete data set.

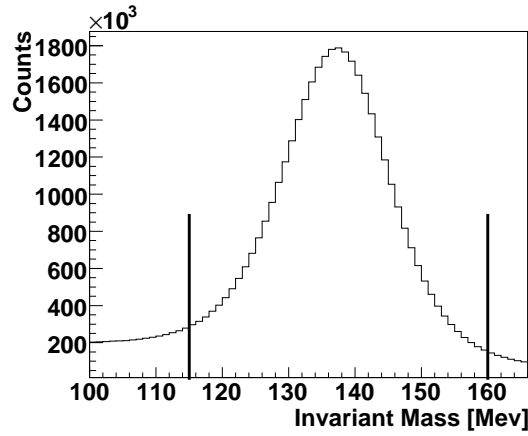


Figure 6.5: Invariant mass of the two photons from a candidate  $\gamma p \rightarrow n\pi^+\pi^0$  event. A cut between 115 and 160 MeV is applied.

### Missing mass analysis

As in the case of double  $\pi^0$ , the missing mass is used to ensure that the selected events really correspond to  $\gamma p \rightarrow n\pi^+\pi^0$  events. The missing mass is computed using eq. 6.5 where the  $\pi^+$  replaces one of the two  $\pi^0$ . Fig. 6.6 represents the missing mass as a function of the incoming photon energy. For this channel, the background plays a more important role than for double  $\pi^0$  and two structures can

be distinguished. The first one is a peak centered at  $m_{neutron}$  and corresponds to good  $\pi^0 \pi^+$  events. The second one is a broader structure appearing at lower energies and corresponds to  $\gamma p \rightarrow p\pi^0$  events for which the proton is falsely identified as a  $\pi^+$ . In this case,  $\gamma p \rightarrow p\pi^0$  events will be treated as  $\gamma p \rightarrow \pi^0 \pi^+(n)_{not\ detected}$  events. This is especially visible in the 300-500 MeV range where the cross section for the  $\gamma p \rightarrow n\pi^+\pi^0$  is smaller than  $\gamma p \rightarrow p\pi^0$  by two orders of magnitude<sup>3</sup>. The origin of this background is confirmed by computing the missing mass in a different way, subtracting only the  $\pi^0$  from the initial 4-vector.

$$\begin{aligned} m'^2_{miss} &= (P_{beam} + P_{target} - P_{\pi^0})^2 \\ &= (E_\gamma + m_p - E_{\pi^0})^2 - (\vec{p}_\gamma - \vec{p}_{\pi^0})^2 \end{aligned} \quad (6.6)$$

In the case of a misidentified  $\gamma p \rightarrow p\pi^0$  event,  $m'_{miss}$  will be equal to the mass of the proton. Fig 6.7 shows  $m'_{miss}$  over the full energy range and indeed a sharp peak is visible at  $m_{proton}$ . The broader structure at higher energies correspond to good  $\gamma p \rightarrow n\pi^+\pi^0$  events.

The calculation of  $m'_{miss}$  is also helpful to separate the background contribution from good  $\pi^0 \pi^+$  events. When comparing fig. 6.6 and 6.7, we see that the two peaks overlap much less when computing  $m'_{miss}$  than  $m_{miss}$ . In order to get rid of as much background as possible, a  $3\sigma$  cut on  $m_{miss}$  is applied in the same way as for double  $\pi^0$  and is followed by a cut on  $m'_{miss}$  ( $m'_{miss} > 1040$  MeV, thick line on fig. 6.8).

#### 6.1.4 $\gamma p \rightarrow n\pi^+\pi^0$ cross section

Here again, the cross section is calculated with eq. 6.1 and is presented for all the beamtimes in fig. 6.8. As in the case of double  $\pi^0$ , both beamtimes agree very well except for a small discrepancy at high energies for the July beamtime which was perturbed by the presence of ice on the target window. These results are discussed further in section 7.2.

## 6.2 Asymmetry

As presented in section 2.5, the asymmetry is a powerful tool to study the internal mechanisms of a reaction and especially the individual contribution of the resonances. Due to the high sensitivity of polarization observables to small details of the models, a precise calculation of asymmetry observables using models such

---

<sup>3</sup>In addition, the detecting efficiency for this latter channel is very high, around 80% [HorPr].

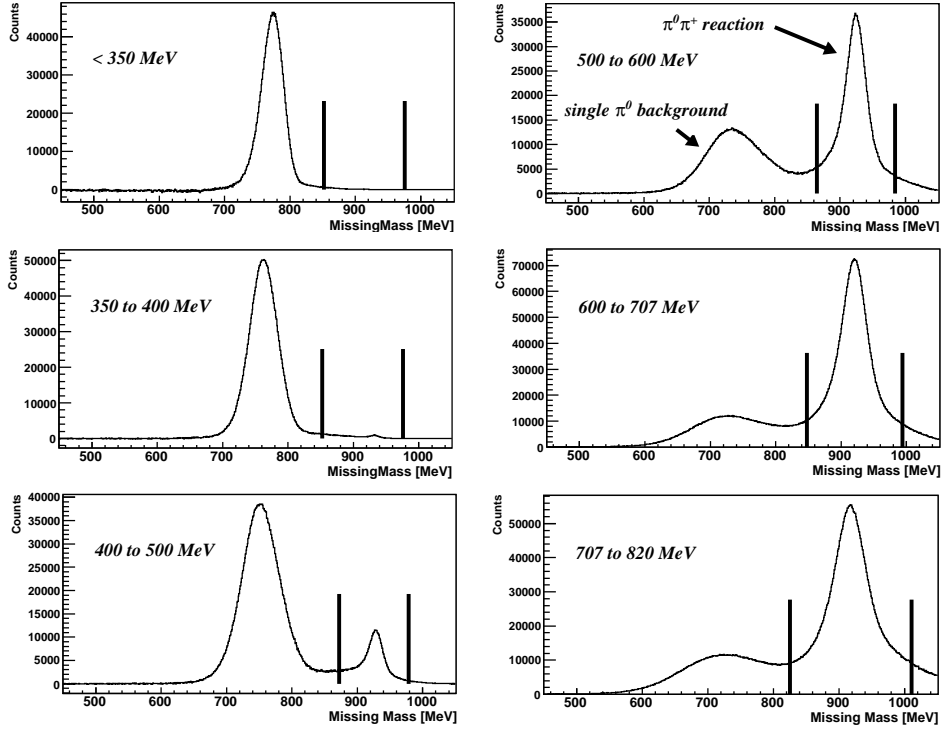


Figure 6.6: Missing mass for different incoming photon energy bins for the  $\gamma p \rightarrow n\pi^+\pi^0$  reaction. The good events show a peak at  $m_{miss} = m_{neutron}$  whereas misidentified  $\gamma p \rightarrow p\pi^0$  appear in a broader structure at lower energies. The peak is fitted with a Gaussian distribution and a  $3\sigma$  cut (thick line) is applied.

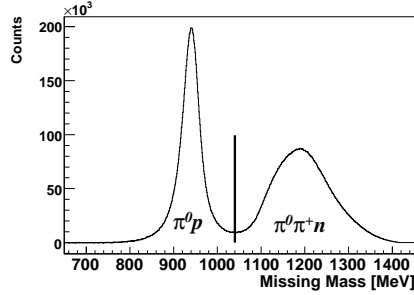


Figure 6.7: Missing mass  $m'_{miss}$  for the  $\gamma p \rightarrow n\pi^+\pi^0$  reaction. The  $\gamma p \rightarrow p\pi^0$  background forms a peak at  $m_{proton}$ . A cut is applied to remove it ( $m'_{miss} > 1040$  MeV).

as [Roc05] and [Fix05] containing up to 25 Feynman diagrams is a tricky task. In the experimental case, the determination of the asymmetry is on the contrary quite straightforward. It is defined by

$$A = \frac{1}{P_\gamma} \frac{d\sigma^+ - d\sigma^-}{d\sigma^+ + d\sigma^-} \quad (6.7)$$

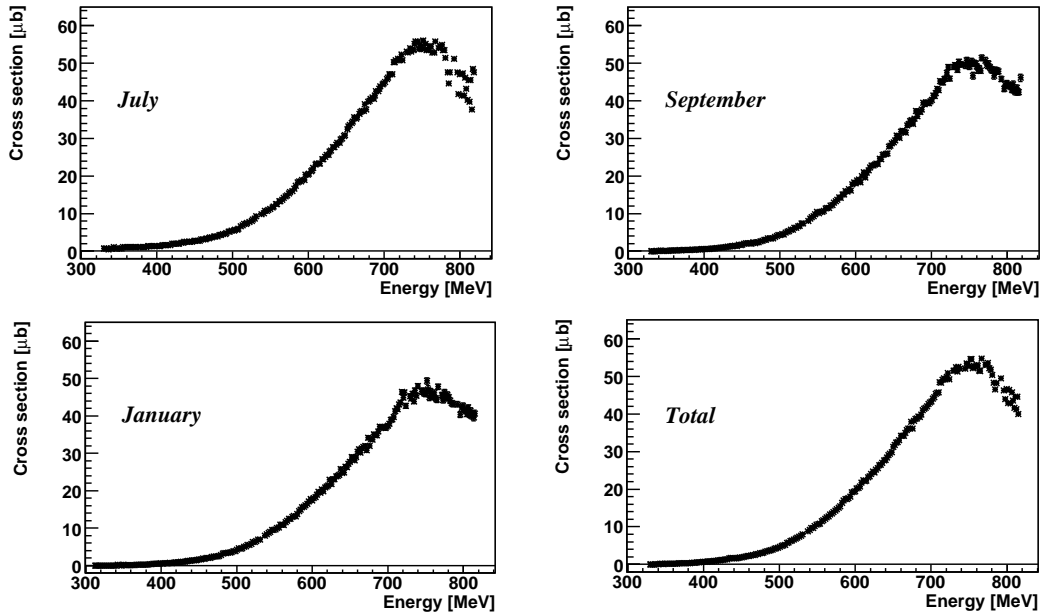


Figure 6.8:  $\gamma p \rightarrow \pi^0 \pi^0 p$  Cross section for the  $\gamma p \rightarrow n \pi^+ \pi^0$  reaction for the different beamtimes and for the complete data set.

which is eq. 2.4 in which the polarization degree of the beam (determined in section 3.2) has been introduced. This equation can be simplified. The factors used in eq. 6.1 for the absolute normalization of the cross section are equal for each polarization state of the incoming photon<sup>4</sup>. In addition, the difference in the incoming photon flux  $\alpha$  has to be taken in account. For circularly polarized photons, the value of  $\alpha = N_{\gamma}^{Left}/N_{\gamma}^{Right}$  has been estimated to 1.00055 in [Kra06] and is thus negligible. For linearly polarized photons, the orientation of the diamond radiator responsible for the orientation of the polarization was flipped approximately every 15 minutes. In this case, no careful matching of the two states of polarization has been done but when counting the total amount of parallel and perpendicular events for each beamtime, it turns out that the introduced bias is of the order of  $10^{-5}$ , neglectable as well.

$$A = \frac{1}{P_{\gamma}} \frac{N^{+}(\phi) - N^{-}(\phi)}{N^{+}(\phi) + N^{-}(\phi)} \quad (6.8)$$

Using formula 6.8, the asymmetry can be directly determined by computing  $\phi$  for each of the two photon polarization states as well as their sum and difference. This is illustrated in fig. 6.9 for circular asymmetry in the  $\vec{\gamma} p \rightarrow n \pi^+ \pi^0$  reaction. The asymmetry will be calculated as a function of the incoming beam energy.

<sup>4</sup>The detecting efficiency is not dependant on the the polarization due to the  $4\pi$  coverage and the azimuthal symmetry of the detector. For the other factors  $\epsilon_{tagg}$ ,  $N_{e-}$  and  $N_{target}$ , this is a trivial observation.

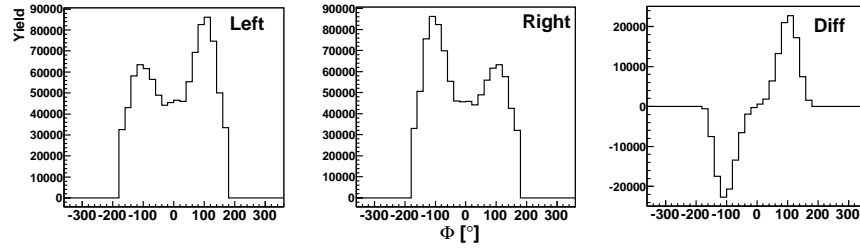


Figure 6.9:  $\phi$  angle yield used to determine the asymmetry. Left: Left-handed photon. Middle: Right-handed photon. Right: Difference between the two.

The results for each type of polarization and each reaction are presented in the following sections.

### 6.2.1 Circular asymmetry

#### Circular asymmetry for $\vec{\gamma}p \rightarrow n\pi^+\pi^0$

We have calculated the circular asymmetry for the  $\vec{\gamma}p \rightarrow n\pi^+\pi^0$  reaction as a function of the incoming photon energy. Nine 50 MeV bins between 370 and 820 MeV have been defined.

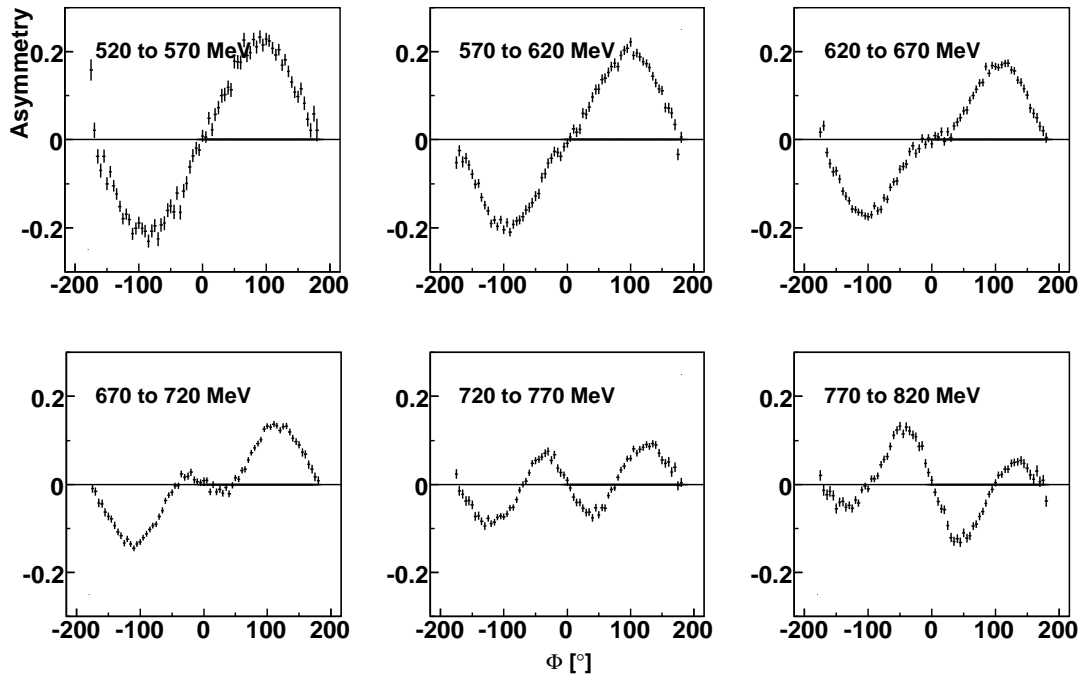


Figure 6.10: Circular asymmetry for the  $\vec{\gamma}p \rightarrow n\pi^+\pi^0$  channel.

In fig. 6.10, which shows our results for the six higher energy bins, the very high

statistical quality of the data as well as the strong dependance on the incoming photon energy can be observed. The physical interpretation of these sensitive results is done in section 7.3. In the same section, we show the circular asymmetry results for the two other isospin channels ( $\vec{\gamma}p \rightarrow p\pi^0\pi^0$  and  $\vec{\gamma}p \rightarrow \pi^+\pi^-p$ ) which were determined by D. Krambrich using the same data [Kra07].

### 6.2.2 Linear asymmetry

As we have seen in section 3.2, linearly polarized photons are produced at energies between 390 and 450 MeV. This choice was made to optimize the study of the asymmetry for the  $\Delta$  magnetic moment reaction, the cross section for this reaction being maximal at  $\sim 450$  MeV. For double pion production, this choice is much less favorable as the cross section are smaller than  $1 \mu b$  in this energy region. More important, the expected asymmetries are supposed to be tiny and then very difficult to observe.

#### Linear asymmetry for $\vec{\gamma}p \rightarrow p\pi^0\pi^0$

The linear asymmetry for  $\vec{\gamma}p \rightarrow p\pi^0\pi^0$  was anyhow computed using eq. 6.8 and the results can be found in fig. 6.11

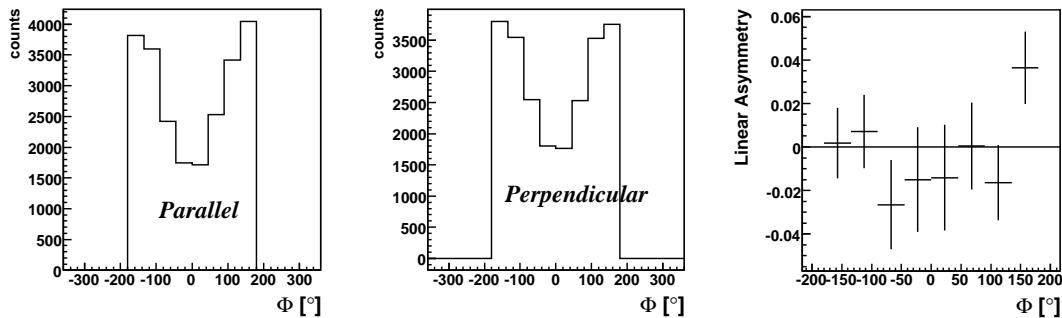


Figure 6.11: *Linear asymmetry for the  $\vec{\gamma}p \rightarrow p\pi^0\pi^0$  channel in the 390 - 450 MeV incoming photon energy range. Left and middle:  $\phi$  angle distribution for each of the two polarization states. Right Linear asymmetry.*

As an opposite to circular polarization, no significative difference can be observed between the two polarization states. This make all asymmetry points gather around zero with large error bars. The few conclusions we can draw about this result are presented in section 7.4.

#### Linear Asymmetry for $\vec{\gamma}p \rightarrow n\pi^+\pi^0$

Linear asymmetry for the  $\vec{\gamma}p \rightarrow n\pi^+\pi^0$  reaction has been measured in the same way as  $\vec{\gamma}p \rightarrow p\pi^0\pi^0$ . Here again, no significative difference between parallel

and perpendicular orientations of the incoming photon can be observed. The asymmetries are therefore compatible with zero with large error bars.

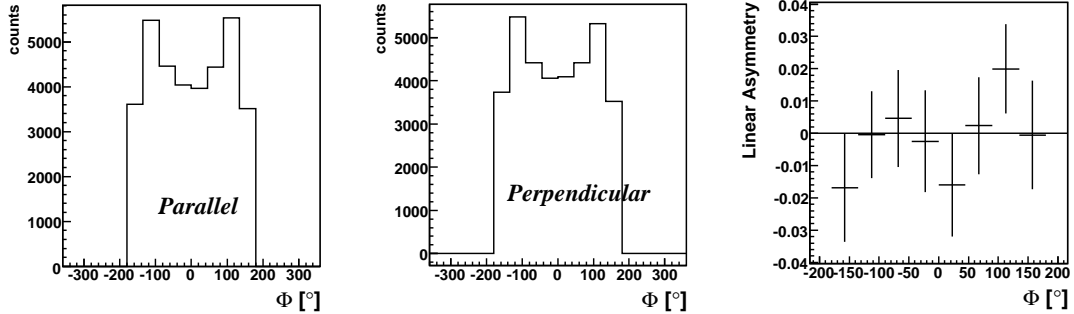


Figure 6.12: *Linear asymmetry for the  $\vec{\gamma}p \rightarrow n\pi^+\pi^0$  channel in the 390 - 450 MeV incoming photon energy range. Left and middle:  $\phi$  angle distribution for each of the two polarization states. Right: Linear asymmetry.*

### 6.3 Dalitz plots

Along with the asymmetry, Dalitz plots are a simpler and still efficient tool to investigate the existence of intermediate states in 3-body decays of resonances. They were first introduced by R. Dalitz in 1953 [Dal53] to study the decay of strange mesons into three pions ( $K^+ \rightarrow \pi^+\pi^+\pi^-$ ). Although Dalitz plots is a generic term that encompasses various kinds of scatter plots, they are nowadays mostly to be found in the form defined in [PDG06] and described below. For a particle A decaying into three particles  $A \rightarrow C_1 + C_2 + C_3$  with mass  $m_i$  and 4-vectors  $P_i$ , we define the variables  $m_{ij}^2$  corresponding to the invariant masses of all possible combinations of two particles.

$$m_{12}^2 = (P_1 + P_2)^2, \quad m_{13}^2 = (P_1 + P_3)^2, \quad m_{23}^2 = (P_2 + P_3)^2 \quad (6.9)$$

Dalitz plots are then produced by picking two of the three  $m_{ij}^2$  and plotting them in a two dimensional scatter plot. For a given 3-body decay, three possible Dalitz plots ( $m_{12}^2$  vs  $m_{23}^2$ ,  $m_{12}^2$  vs  $m_{13}^2$  and  $m_{13}^2$  vs  $m_{23}^2$ ) can therefore be constructed.

In a Dalitz plot, not all combinations of  $m_{12}^2$  and  $m_{23}^2$  are accessible. Fig 6.13 shows the limits allowed by the kinematics of the 3-body decay. The minimal value for  $m_{12}^2$  is obtained when both particles are at rest and all the available energy has been transmitted to the third particle ( $(m_1 + m_2)^2 \leq m_{12}^2$ ). At the other side, the maximal value of  $m_{12}^2$  happens when the third particle is at rest and all the available energy is distributed between particles 1 and 2. ( $m_{12}^2 \leq (m_A - m_3)^2$ ). Between these extreme values, the kinematically allowed

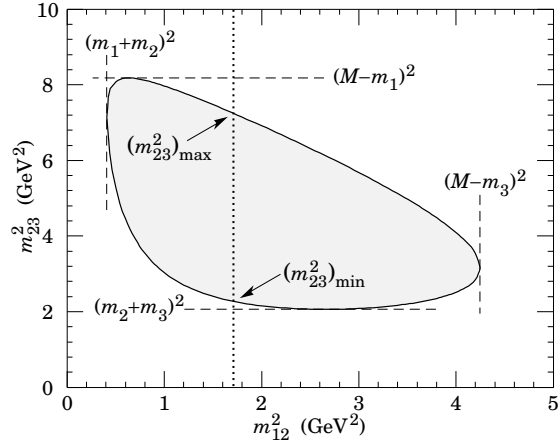


Figure 6.13: *Kinematical limits for a 3-body final state Dalitz plot. ( $M = m_A$ ).*

values for  $m_{23}^2$  are represented by the shaded area in fig. 6.13. The boundary of this zone is given by eq. 6.10 from [PDG06].

$$(m_{23}^2)_{min/max} \leq (E_2^* + E_3^*)^2 - (\sqrt{E_2^{*2} - m_2^2} \pm \sqrt{E_3^{*2} - m_3^2})^2 \quad (6.10)$$

where  $E_2^* = (m_{12}^2 - m_1^2 + m_2^2)/2m_{12}$  and  $E_3^* = (m_A^2 - m_{12}^2 - m_3^2)/2m_{12}$  are the energies of the particles in the  $m_{12}$  rest frame.

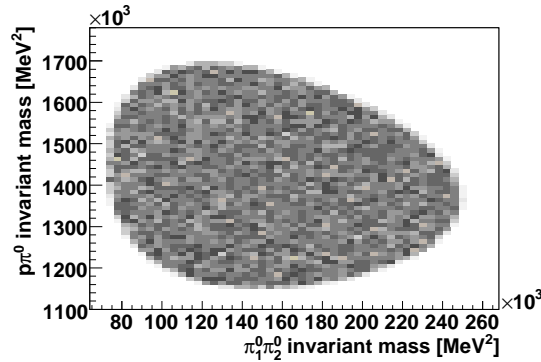


Figure 6.14: *Dalitz plot for the  $\gamma p \rightarrow p\pi^0\pi^0$  reaction using simulated data from a phase space generator. The data is uniformly distributed inside the kinematically allowed region.*

The physical interest of the Dalitz plots lies in the way the events are distributed in the kinematically allowed region. In the simplest case, when the 3-body decay is a phase space decay, no conditions are imposed on the values of  $m_{12}^2$  and  $m_{23}^2$  and the Dalitz plot will be uniformly populated. This can be seen in fig 6.14 which shows a Dalitz plots made with our phase space generator for the

$\gamma p \rightarrow p\pi^0\pi^0$  reaction with an incoming photon energy of 630 MeV. When the decay of the initial state is a sequential decay with an intermediate resonance  $A \rightarrow B + C_3 \rightarrow C_1 + C_2 + C_3$  further conditions will be imposed to the value of  $m_{12}^2$ . Here, the intermediate state B decaying into  $C_1$  and  $C_2$  imposes the condition  $m_{C_1C_2}^2 = m_B^2$  and an enhanced region will appear in the Dalitz plots at  $m_{12}^2 = m_B^2$ .

### 6.3.1 $\gamma p \rightarrow p\pi^0\pi^0$ Dalitz plots

Dalitz plots were produced in the  $\gamma p \rightarrow p\pi^0\pi^0$  channel by computing all three mass combinations  $m_{\pi_1^0\pi_2^0}^2$ ,  $m_{\pi_1^0p}^2$  and  $m_{\pi_2^0p}^2$  for each event. As previously stated, for a given 3-body decay, three different Dalitz plots can be created. In the case of double  $\pi^0$  production however, both  $\pi^0$  are undistinguishable so that, among the three possible Dalitz plots, ( $m_{\pi_1^0\pi_2^0}^2$  vs  $m_{\pi_1^0p}^2$ ,  $m_{\pi_1^0\pi_2^0}^2$  vs  $m_{\pi_2^0p}^2$  and  $m_{\pi_1^0p}^2$  vs  $m_{\pi_2^0p}^2$ ) the first two would produce physically identical results. They are therefore added in a single  $m_{\pi^0\pi^0}^2$  vs  $m_{\pi^0p}^2$  Dalitz plot.

The results are presented as a function of the incoming photon energy: for each combination, 6 Dalitz plots corresponding to 50 MeV incoming photon energy bins between 500 and 800 MeV have been produced. As for cross sections, the Dalitz plots have to be normalized to account for the conditions of our experiment (eq. 6.1). The detecting efficiency for Dalitz plots is determined with the methods presented in chapter 5. All other normalization factors don't depend on the mass distributions and are simply treated as global scaling factors. The results are presented in fig. 6.15 for  $m_{\pi^0\pi^0}^2$  vs  $m_{\pi^0p}^2$  and in fig. 6.16 for  $m_{\pi_1^0p}^2$  vs  $m_{\pi_2^0p}^2$ .

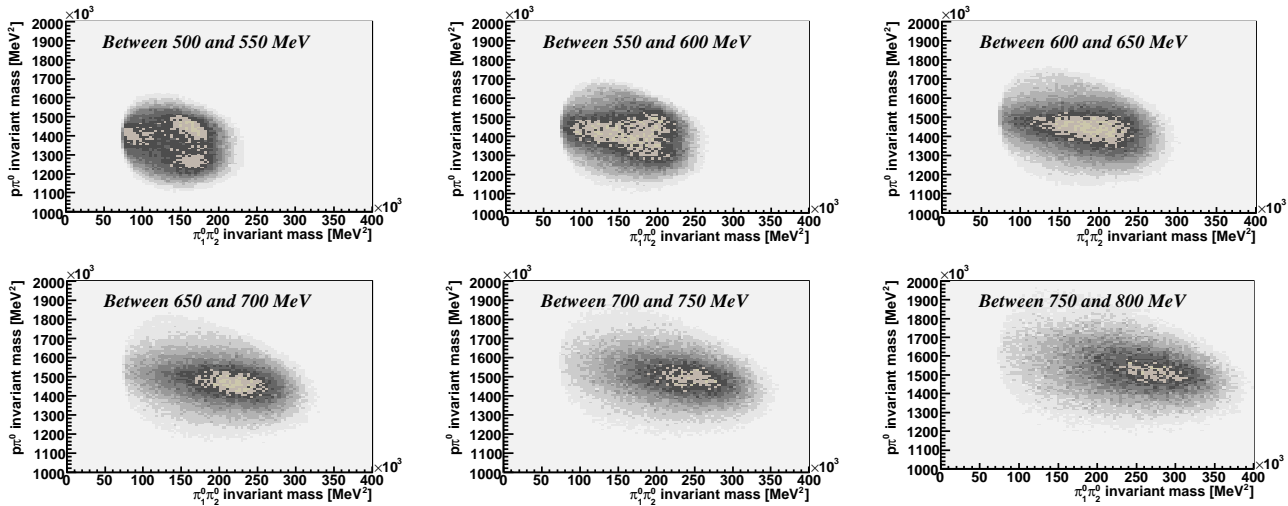


Figure 6.15: Dalitz plots for the  $\gamma p \rightarrow p\pi^0\pi^0$  reaction. The combination  $m_{\pi^0\pi^0}^2$  vs  $m_{\pi^0p}^2$  is represented as a function of the incoming photon energy.

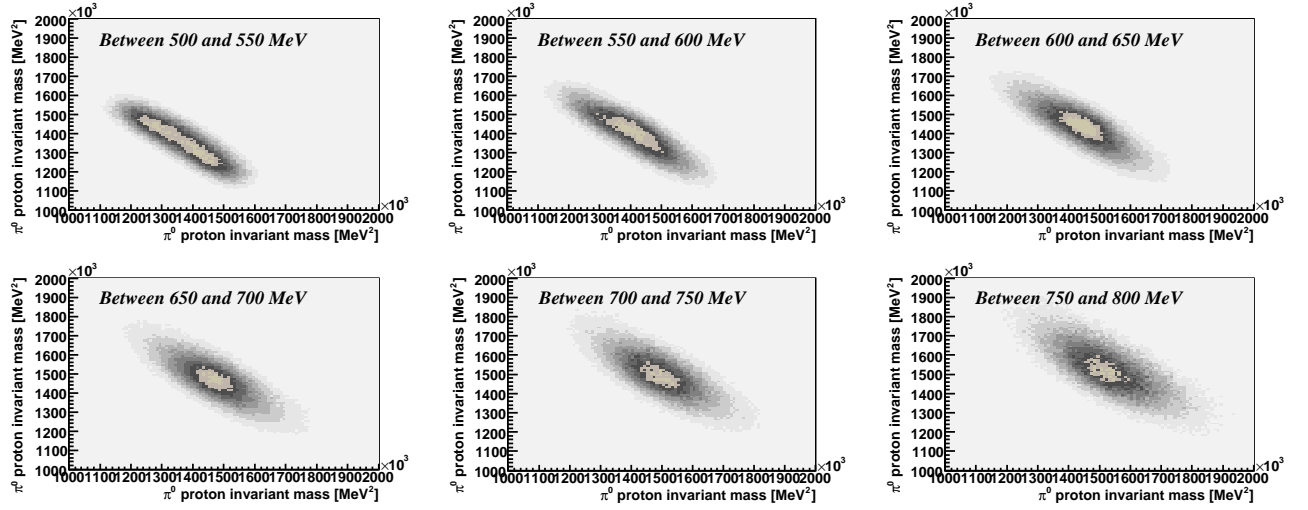


Figure 6.16: Dalitz plots for the  $\gamma p \rightarrow p\pi^0\pi^0$  reaction. The combination  $m_{\pi^+p}^2$  vs  $m_{\pi^0p}^2$  is represented as a function of the incoming photon energy

In these two sets of Dalitz plots, a well defined enhanced region can be seen at all energies. It is a clear signature for the presence of an intermediate state in the production of the  $\pi^0 \pi^0 p$  final state. Since this enhanced region appears at  $m_{\pi^0p}^2 \approx 1.5 \cdot 10^6 \text{ Gev}^2 \approx m_{\Delta(1232)}^2$ , this is a first good indication of the dominance of a sequential decay of the resonance. Since two-dimensional plots are difficult to interpret further without introducing elaborate data analysis tools, we will base our discussion on the projections of these plots on each of their axis. This is done in section 7.5. Again, these plots were shown above all to insist on the very good statistical quality of our data in comparison to previous experiments.

### 6.3.2 $\gamma p \rightarrow n\pi^+\pi^0$ Dalitz plots

In fig. 6.17 to 6.19, we show the three possible Dalitz plots for the  $\gamma p \rightarrow n\pi^+\pi^0$  reaction. Here again, an enhanced region appearing at  $m_{\pi^0n}^2$  and  $m_{\pi^+n}^2 \approx m_{\Delta(1232)}^2$ , is the signature of a sequential decay of the resonance. As for the double  $\pi^0$ , more detailed physics is extracted with the projection of these Dalitz plots on their axis.

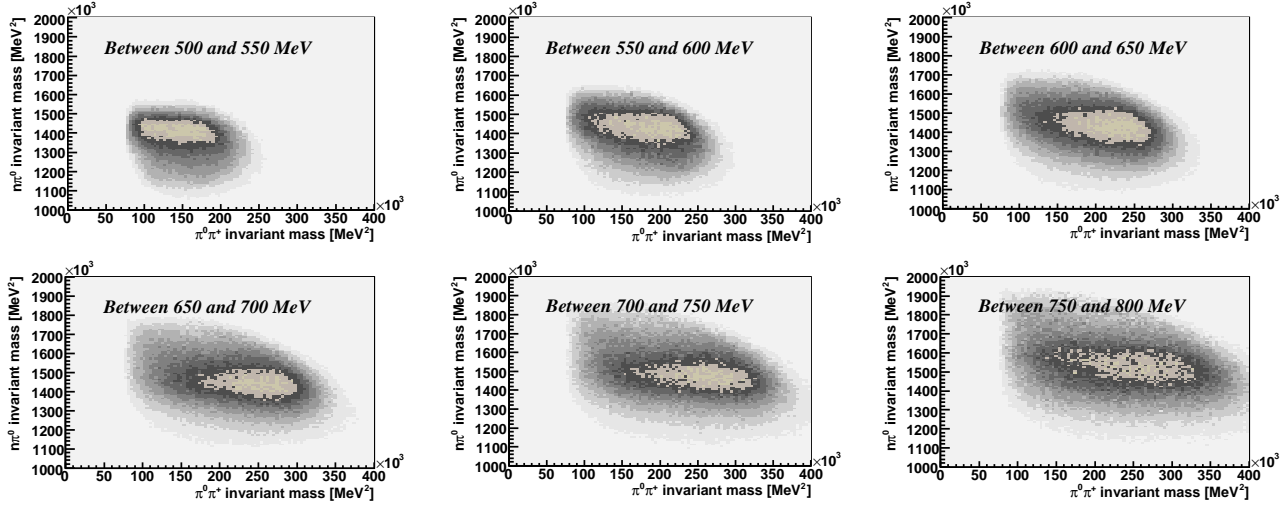


Figure 6.17: *Dalitz plots for the  $\gamma p \rightarrow n\pi^+\pi^0$  reaction. The combination  $m_{\pi^0\pi^+}^2$  vs  $m_{\pi^0n}^2$  is represented as a function of the incoming photon energy.*

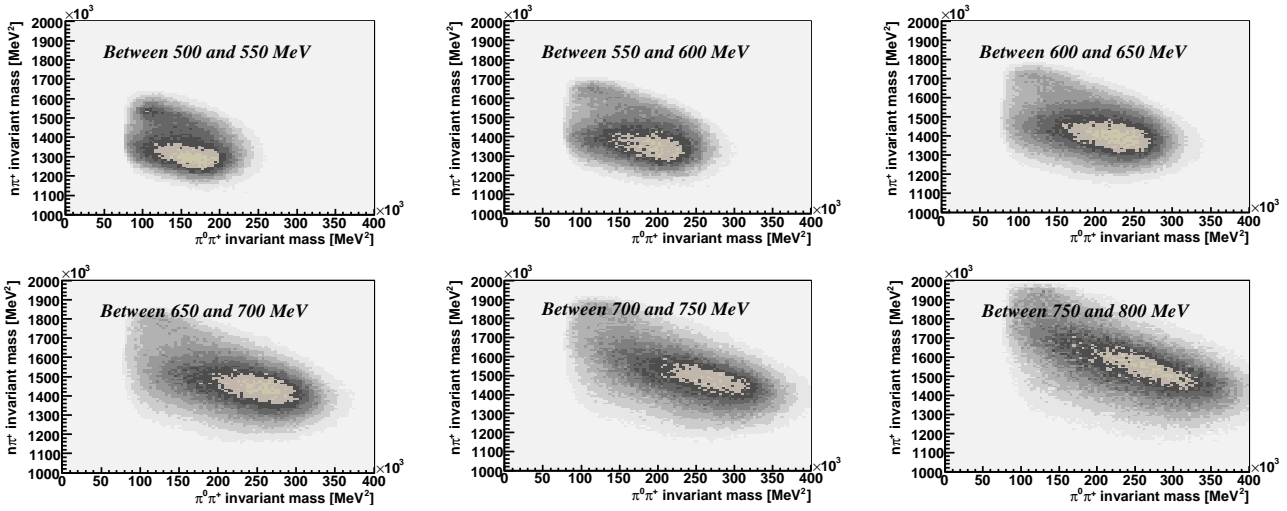


Figure 6.18: *Dalitz plots for the  $\gamma p \rightarrow n\pi^+\pi^0$  reaction. The combination  $m_{\pi^0\pi^+}^2$  vs  $m_{\pi^+n}^2$  is represented as a function of the incoming photon energy.*

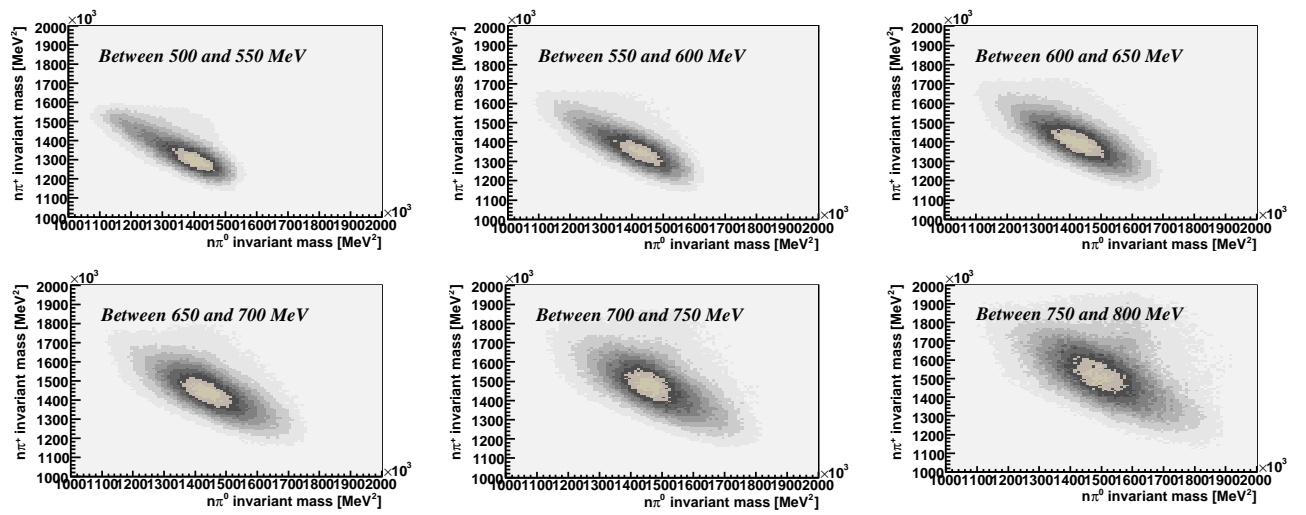


Figure 6.19: Dalitz plots for the  $\gamma p \rightarrow n\pi^+\pi^0$  reaction. The combination  $m_{\pi^0 n}^2$  vs  $m_{\pi^+ n}^2$  is represented as a function of the incoming photon energy.



# 7 Results

*In chapters 3 to 6, our data has been measured, calibrated, simulated and analyzed. It is now ready to be compared with the theoretical previsions presented in chapter 2 and with the results from previous measurements to give a clearer understanding of the behaviour of double pion photoproduction reactions.*

*We will first present the total cross section of the  $\gamma p \rightarrow p\pi^0\pi^0$  and the  $\gamma p \rightarrow n\pi^+\pi^0$  reactions with a special emphasis on the double  $\pi^0$  cross section at threshold which will be precisely compared with chiral perturbation theory previsions for the first time. We will then compare our asymmetries with the Valencia and Mainz models and see what conclusions we can draw about the internal mechanisms of the reaction. Finally, we will use the Dalitz plots and the invariant mass distributions to account for the intermediate resonances present in the double pion decays. About this latter point, the  $D_{13}(1520) \rightarrow \rho n$  contribution to the  $\gamma p \rightarrow n\pi^+\pi^0$  channel will attract most of the attention.*

## 7.1 $\gamma p \rightarrow p\pi^0\pi^0$ cross section

Fig. 7.1 shows the total cross section for the  $\gamma p \rightarrow p\pi^0\pi^0$  reaction as a function of the incoming photon energy. Our results are compared with the most precise measurement of this channel so far [Kot01] and with the predictions from the Valencia [Nac01] and Mainz [Fix05] models. Compared with the previous experiment, our results show a large improvement in the statistical quality of the data without any significant discrepancy. For both measurements, the cross section rises slowly for the first 150 MeV above production threshold ( $E_\gamma^{threshold} = 309$  MeV) due to the small number of Born terms contributing to this channel. It then rises steadier for the next 300 MeV before reaching a maximum of  $10 \mu\text{b}$  at 730 MeV. At higher energies the cross section decreases, attaining  $8 \mu\text{b}$  at 820 MeV.

The theoretical model best describing these results is the Valencia model. For energies up to 650 MeV, our data is very well reproduced by this model, while at higher energies they get slightly overestimated. Still, on the whole energy range,

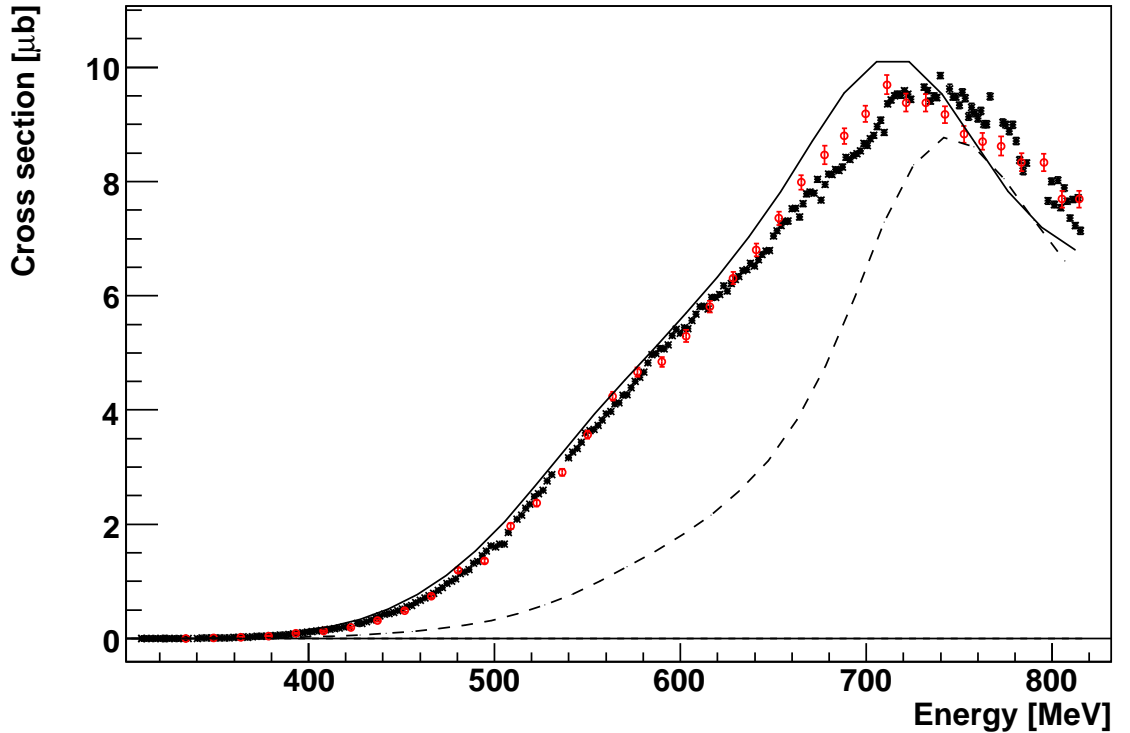


Figure 7.1: Total cross section for the double  $\pi^0$  reaction. Our results (black squares) are represented together with the most precise results so far (red circles, [Kot01]) and the theoretical predictions from the Valencia (solid) and Mainz (dashed) models.

the agreement is fairly good with discrepancies not exceeding 10%. The situation is different for the Mainz model. For energies up to 700 MeV, this model strongly underestimates our data. In the most extreme case ( $\sim 640$  MeV), our results are three times higher than the Mainz calculation. At higher energies, the agreement is better with a peak predicted at  $9 \mu\text{b}$  for  $E_\gamma = 750$  MeV and a decrease of the cross section at higher energies. This is a first illustration of the difficulties arising in the theoretical handling of the double pion channel. Two models with very similar assumptions lead to dramatically different predictions. This will be a recursive remark throughout this chapter.

Physically, the peak observed at  $E_\gamma \approx 730$  MeV ( $\sqrt{s} \approx 1500$  MeV) is the signature of a strong contribution of resonances from the second energy region (diagrams fig. 2.3). A further interpretation of this total cross section is limited by the fact that the three resonances forming the second resonance region are broad, lay close to each other and thus strongly overlap, preventing us to distinguish the individual contribution of each resonance. In order to disentangle the  $P_{11}(1440)$ ,

the  $D_{13}(1520)$  and the  $S_{11}(1535)$ , we will have to use more sensitive observables such as asymmetries and Dalitz plots presented in the next sections.

### 7.1.1 $\gamma p \rightarrow p\pi^0\pi^0$ Cross section at threshold

In the second resonance region, the previous experiments had already fixed the values of the cross sections with a precision of a few percent. Our results, however improving largely the precision of the cross section, don't bring much new information about the physics behind the  $\gamma p \rightarrow p\pi^0\pi^0$  reaction. In the threshold region, this is different. For energies between  $E_{\pi^0\pi^0 p}^{thresh} = 308.8$  MeV to  $\sim 350$  MeV in which the chiral perturbation theory [Ber96] can be applied, even the most conclusive experiment so far [Kot03] is reproducing the prevision of the model with large error bars.

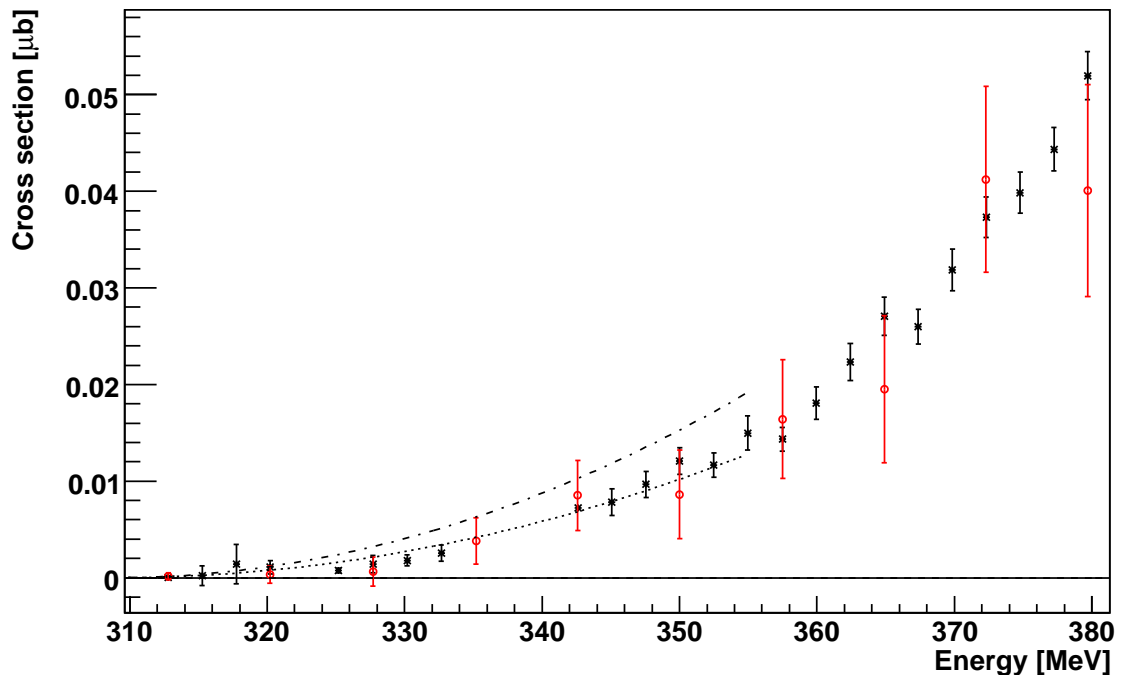


Figure 7.2: *Total cross section for the double  $\pi^0$  reaction at threshold. Our results (black squares) are represented together with the results from [Kot03] (red circles) and the theoretical predictions from [Ber96]. Dotted: ChPT average value. Dash-dotted: ChPT upper limit.*

Fig. 7.2 shows the total cross section as a function of the incoming photon en-

ergy in the threshold region. The results from the previous experiment have been represented as well as the predictions from chiral perturbation theory. For this last one, the prevision from eq. 2.7 has been represented together with the upper limit of this model. This difference lies in the uncertainty of the coupling of the  $P_{11}(1440)$  resonance to the s-wave  $\pi\pi$  channel.

Here, the very good statistical quality of our data allows a precise determination of the cross section close to threshold with very small error bars. The predictions of chiral perturbation theory are admirably well reproduced with a very high precision. This is a striking evidence of the pertinence of ChPT in this energy region. In addition, these results can be used to constraint the coupling of the  $P_{11}(1440)$  to the s-wave  $\pi\pi$  channel in this energy range.

### Systematic errors

As an opposite to all other results presented in this chapter, which might vary in absolute magnitude without affecting their interpretation, the determination of the absolute value of the cross section is here the key issue. In that sense, the discussion would not be complete without an estimation of the systematic errors. The main sources of systematic errors are -

- the photon flux and the target density with an error estimated in [Dow07] to be 4.5%
- the tagging efficiency which can vary up to 2% within each beamtime
- the efficiency determination which is estimated to be 5%
- the 4X4 tagger structure (4%) and the ice deposition on the target window (5%) accounted for in appendix A and B.

Altogether, the quadratic addition of these uncertainties gives an overall 9.5% systematic error on the double  $\pi^0$  cross section close to threshold. This additional error is not big enough to change the interpretation of our results. Even 10% higher or lower, they would still be in good agreement with the average value of the ChPT calculation.

## 7.2 $\gamma p \rightarrow n\pi^+\pi^0$ cross section

Fig. 7.3 shows the total cross section for the  $\gamma p \rightarrow n\pi^+\pi^0$  reaction as a function of the incoming photon energy. Again, our results are compared with the most precise experiment so far [Lan01] and with the theoretical previsions from the Valencia and Mainz models. On the whole, the observations that were drawn for

the double  $\pi^0$  channel still hold for the  $\pi^0 \pi^+$  channel. Our data confirms the result of the previous experiment with a very large improvement in the statistics. (When looking closer at the cross sections though, one can distinguish a small discrepancy between both data sets. For energies between 450 and 550 MeV, our values are slightly smaller than W. Langgärtner's. This is opposite at higher energies, between 550 and 650 MeV). Here, the cross section rises faster than for the double  $\pi^0$  channel due to the larger number of background processes allowed. It peaks at  $\sigma \approx 50 \mu\text{b}$  for  $E_\gamma \approx 750$  MeV before slightly going down. Again, this peak is the signature of a contribution of resonances from the second resonance region to this channel but due to the strong overlapping of the resonances doesn't allow any further interpretation.

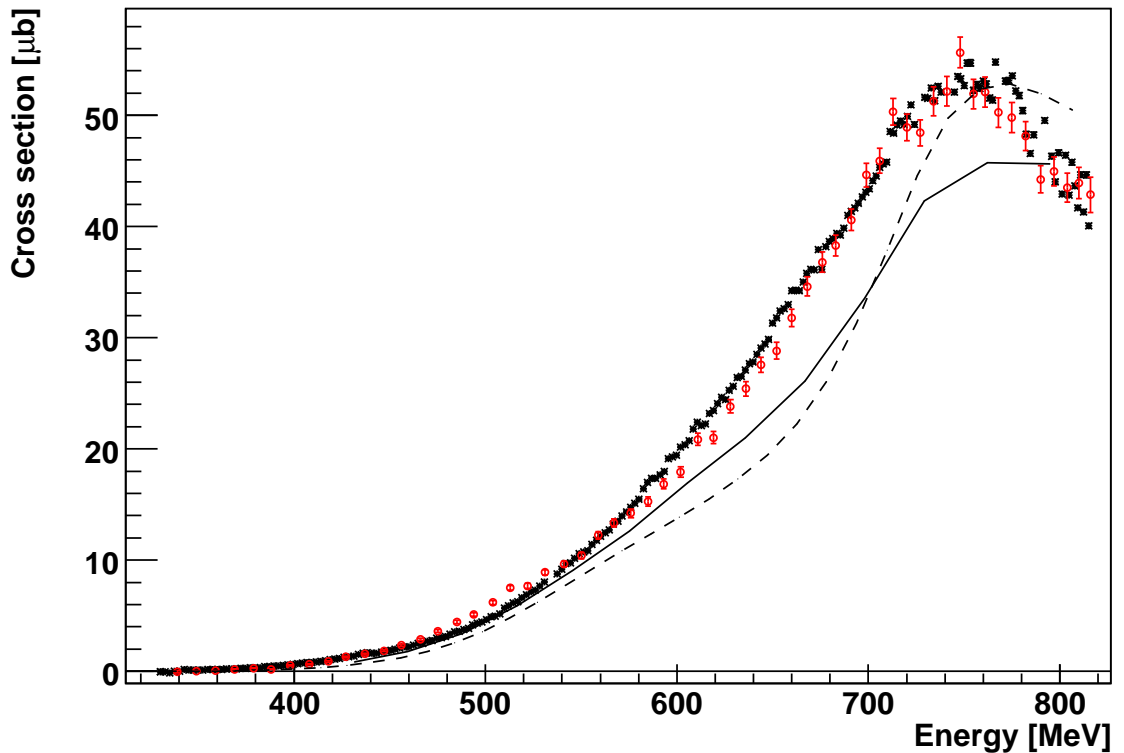


Figure 7.3: Total cross section for the  $\pi^0 \pi^+$  reaction. Our results (black squares) are represented together with the most precise results so far (red circles, [Lan01]) and the theoretical predictions from the Valencia (solid) and Mainz (dashed) models.

In this case, the behaviour of our cross section is best reproduced by the Mainz model. It agrees quite well with our results below 500 MeV. At higher energies,

it noticeably underestimates them up to 750 MeV at which it knows its maximal value. The height of this peak is in good agreement with our data ( $50 \mu\text{b}$ ) though shifted towards higher energies. As an opposite to the double  $\pi^0$  channel, this maximal predicted value is more a plateau than a peak so that the decrease of our cross section between 750 and 820 MeV is not well reproduced by this model. The shape of the Valencia model's predictions is in better agreement with our data, but the magnitude is underestimated over the complete energy range. Its maximal value only reaches  $45 \mu\text{b}$ . In this model again, the decrease of the cross section at higher energies is not well reproduced.

Finally, let's mention that these two models include contribution from the  $\rho$  meson, especially the  $D_{13}(1520) \rightarrow n\rho^+ \rightarrow n\pi^+\pi^-$  decay.  $\rho$  processes were not taken in account in early models describing this channel which led to much smaller cross sections.

### 7.2.1 $\gamma p \rightarrow n\pi^+\pi^0$ cross section at threshold

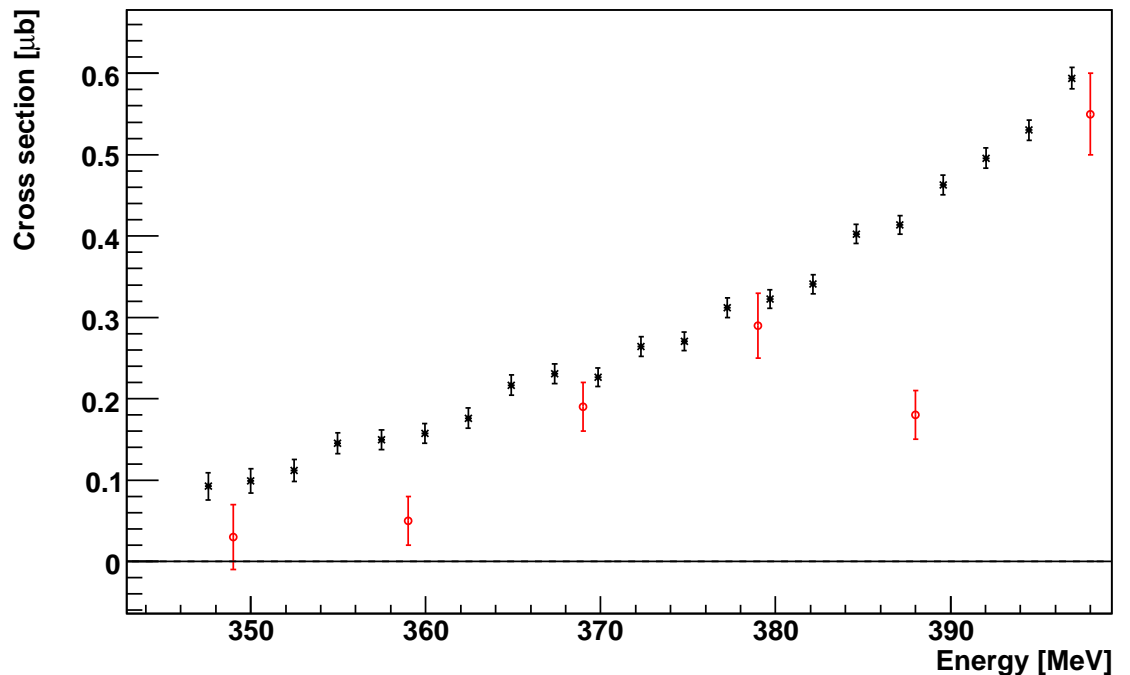


Figure 7.4: Total cross section for the  $\pi^0 \pi^+$  reaction. Our results (black squares) are represented together with the most precise results so far (red circles, [Lan01])

Fig. 7.4 shows the total cross section for the  $\gamma p \rightarrow n\pi^+\pi^0$  as a function of the

incoming photon energy in the threshold region. As an opposite to the double  $\pi^0$  reaction this cross section can't be determined with a very good precision for energies just above production threshold ( $E_\gamma^{threshold} = 315$  MeV). We have seen in fig. 5.3 that the detecting efficiency for this channel drops in this energy range, being negligible at energies below 340 MeV. A precise determination of the cross section close to threshold is therefore not possible. In order to show the difference in the quality of the data between double  $\pi^0$  and  $\pi^0 \pi^+$  production, we have plotted the cross sections for both reactions close to threshold on fig. 7.5.

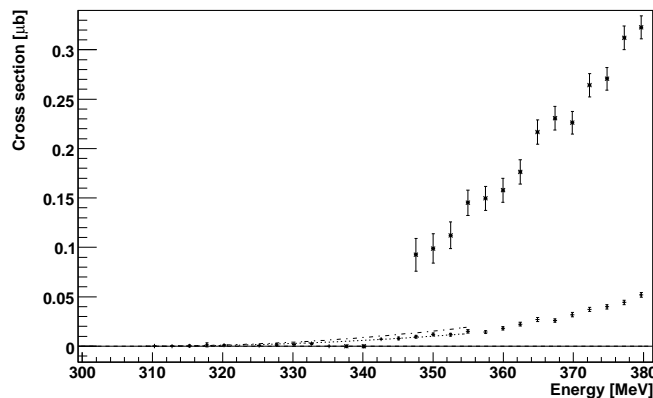


Figure 7.5: Comparison between the  $\gamma p \rightarrow p\pi^0\pi^0$  and  $\gamma p \rightarrow n\pi^+\pi^0$  cross section at threshold. The much better efficiency for the double  $\pi^0$  channel leads to a much more precise determination of the cross section.

### 7.3 Circular asymmetries

In fig. 7.6 we present the beam-helicity asymmetries for the  $\gamma p \rightarrow n\pi^+\pi^0$  reaction for nine incoming energy bins. Our very high statistics data is compared with calculations from the Mainz and Valencia models. Using this later model, two sets of predictions have been produced: one with the full model, the other without the  $D_{13}(1520) \rightarrow \rho n$  contribution<sup>1</sup>.

The first non-vanishing asymmetry is observable in the bin between 420 and 470 MeV. Up to 670 MeV, the shape of this asymmetry is fairly stable, whereas at higher energies, the incoming photon energy dependance is more pronounced. At lower energies (up to 570 MeV), both models fail to reproduce the data. With an increase in the energy, the agreement between the Mainz model and the data

<sup>1</sup>Let's note that since  $\pi^+$  can't be detected in TAPS, an experimental bias could be introduced in our results. Some tests have however showed that the asymmetries are almost not dependant on  $\theta_{\pi^+}$ , so that a comparison between our data and the theoretical calculations without any further correction is reasonable.

would show some improvement if the sign of the model would be flipped, especially in the energy bin from 670 to 720 MeV. At the highest energies, this model fails again to describe our data. The Valencia model is in poor agreement with the data for energies smaller than 720 MeV. At higher energies, the version of this model without contribution from the  $D_{13}(1520) \rightarrow \rho n$  decay reproduces our data much better.

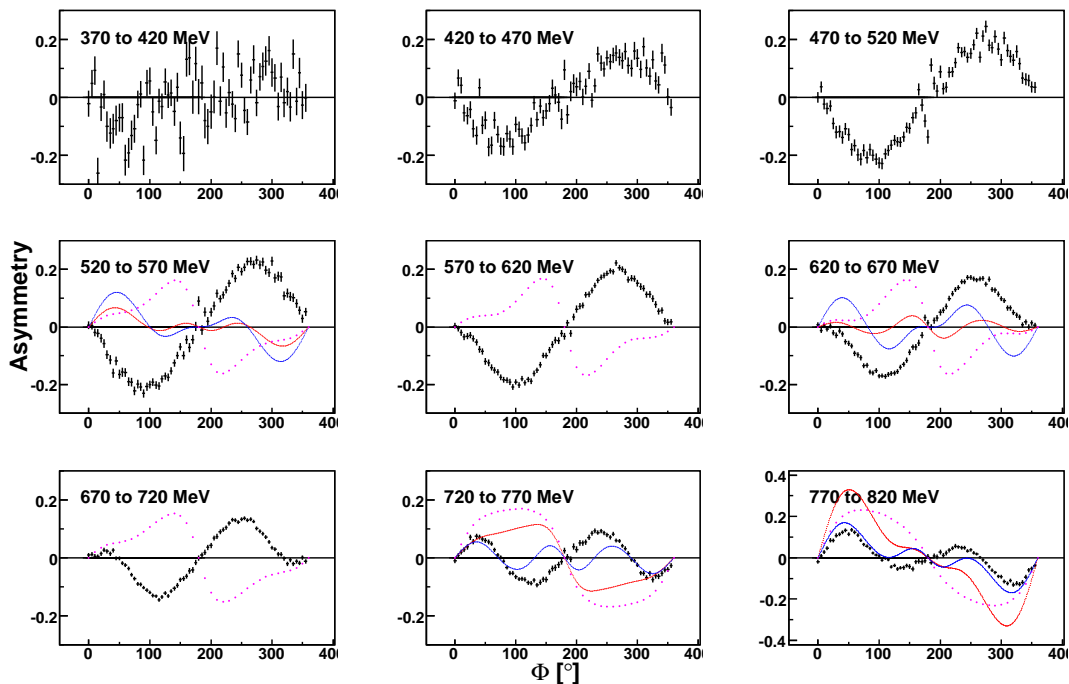


Figure 7.6: *Beam helicity asymmetries in the  $\gamma p \rightarrow n\pi^+\pi^0$  reaction for nine incoming photon energy bins (dots). The lines represent theoretical model calculations. Purple: Mainz model. Red: Valencia full model. Blue: Valencia without  $D_{13}(1520) \rightarrow \rho n$ . For this later model, four fixed photon energies have been used: 575.3, 651.3, 729.9 and 811.1 MeV.*

Giving a physical interpretation of these results is at this point a challenging task. We have seen in section 2.5 that polarization observables are very precious tools to study the individual contribution of resonances. Even diagrams that have a very small influence on unpolarized cross sections can give sizeable contributions to the asymmetry. Furthermore, the interference between different processes -even those giving a small contribution by themselves- leads to noticeable changes in the asymmetries. Therefore, the lack of agreement between our data and the theoretical models doesn't allow such an extraction of resonance contributions to double pion photoproduction. Significant improvements in the models are needed. In a first step, deep modifications are to be performed to give

a rough estimation of our data over the complete energy range. (For instance, it is stated in [Roc05] that the Valencia model doesn't include final state interactions nor complex relative phases in the amplitudes that could influence the asymmetry observables.) Once this done, the contribution of individual processes in the models will be adjusted in order for the calculations to match our results perfectly thus revealing the underlying physics.

Let's however note the surprising fact that our results are best reproduced by the version of the Valencia model without contribution from the  $D_{13}(1520) \rightarrow \rho n$  decay than by the full model. As explained previously, this diagram was introduced to give a reasonable description of the total  $\gamma p \rightarrow n\pi^+\pi^0$  cross section. Once again, this discrepancy calls for further improvements in the models.

To conclude this section, let's mention that the beam helicity asymmetry has also been measured for the two other isospin channel by D. Krambrich using the same data.

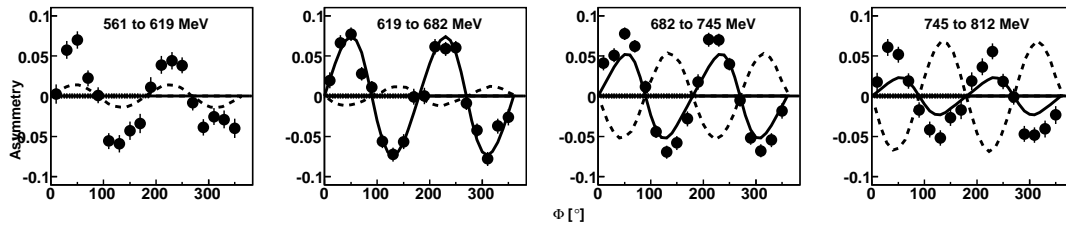


Figure 7.7: Beam helicity asymmetries in the  $\gamma p \rightarrow p\pi^0\pi^0$  reaction for four incoming photon energy bins. The lines represent theoretical model calculations (see fig. 7.6).

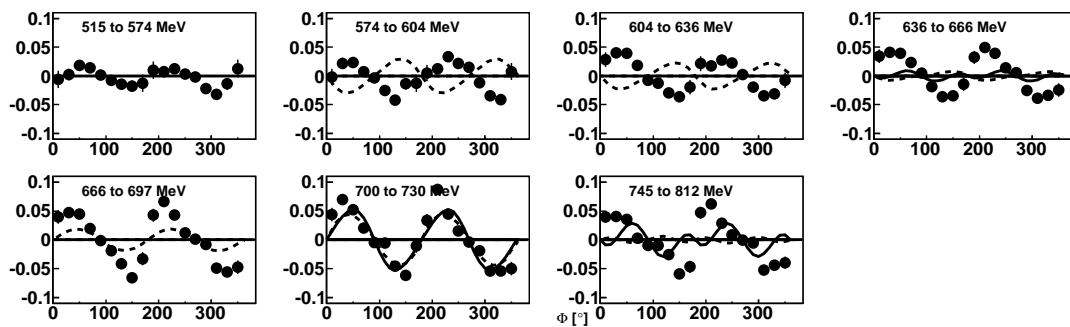


Figure 7.8: Beam helicity asymmetries in the  $\gamma p \rightarrow p\pi^+\pi^-$  reaction for seven incoming photon energy bins. The lines represent theoretical model calculations (see fig. 7.6).

The results are shown in fig. 7.7 and 7.8. Here again, the theoretical models

may show some agreement with the models in some energy bins but fail to give a correct interpretation over the full energy range. The  $\gamma p \rightarrow p\pi^0\pi^0$  asymmetry shows a good agreement with the Mainz model between 619 and 745 MeV but underestimates it at higher energies. The Valencia model underestimates the magnitude at low incident photon energies and is completely out of phase at higher energies. For the  $\gamma p \rightarrow p\pi^+\pi^-$  reaction both models are in agreement for photon energies between 700 and 730 MeV but fail elsewhere. For these two channels also, improvements are needed, even for the double  $\pi^0$  which is simpler to handle due to the smaller number of processes involved. More details on these latest two results can be found in D. Krambrich thesis [Kra07] and in [Kra08].

## 7.4 Linear asymmetries

Fig. 7.9 shows the linear asymmetry in the  $\gamma p \rightarrow p\pi^0\pi^0$  and  $\gamma p \rightarrow n\pi^+\pi^0$  reactions for photons between 390 and 450 MeV corresponding to the region of maximal linear polarization. At such low energies, the asymmetry is very small. Even though the total amount of gathered data is very high, the only observation that can be extracted from these results is that they are compatible with zero within large error bars. Obviously, the study of the linear asymmetry would make more sense at higher energies, where resonances from the second resonance region contribute to the double pion photoproduction. Regrettably for us, the position of the coherent peak was set at this low energy to optimize the determination of the linear asymmetry in the  $\Delta$  magnetic moment experiment. It would anyhow be interesting to compare these results with theoretical calculations. But up to now, this subject has not been investigated by the Mainz nor by the Valencia model people.

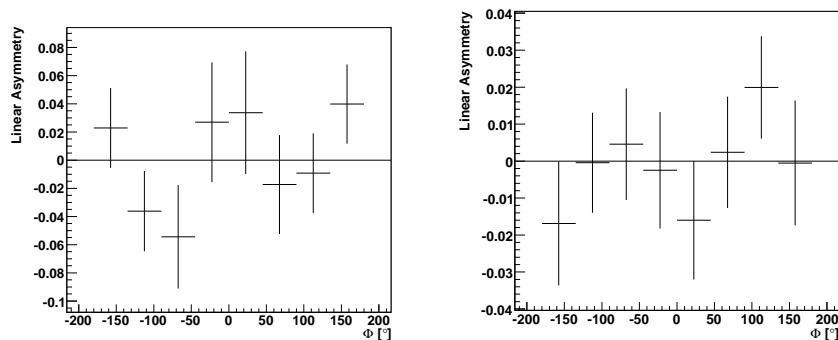


Figure 7.9: *Linear asymmetries for the  $\gamma p \rightarrow p\pi^0\pi^0$  (left) and  $\gamma p \rightarrow n\pi^+\pi^0$  (right) reactions for photons in the coherent peak of linear polarization (390 - 450 MeV).*

## 7.5 Dalitz plots and invariant masses distributions

Dalitz plots are very nice tools for the investigation of intermediate states in resonance decay. In section 6.3 all possible Dalitz plots have been produced for the  $\gamma p \rightarrow p\pi^0\pi^0$  and  $\gamma p \rightarrow n\pi^+\pi^0$  reactions. In this section, we want to extract the physics contained in these plots. Since this extraction from two-dimensional plots might be tricky to carry out, this discussion will be based on invariant mass distributions which correspond to the square root of the projections of the Dalitz plots on each of their axis.

### 7.5.1 $\gamma p \rightarrow p\pi^0\pi^0$ invariant masses

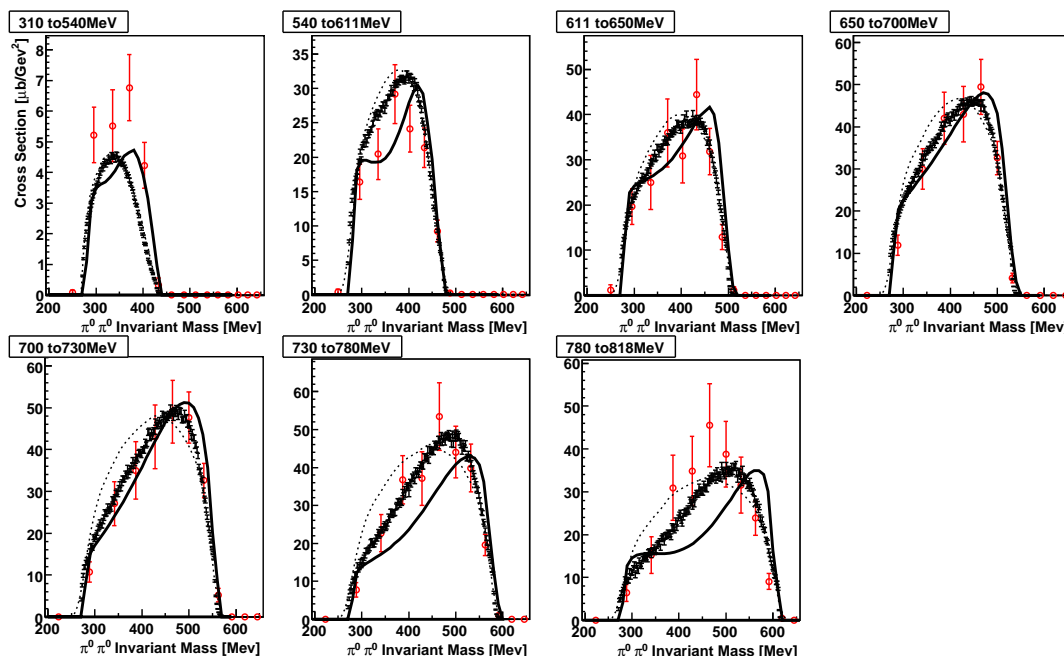


Figure 7.10:  $\pi^0 \pi^0$  invariant mass in the  $\gamma p \rightarrow p\pi^0\pi^0$  reaction. Dashed curve: phase space distribution. Solid Curve: Calculations from the Valencia model.

Figures 7.10 and 7.11 show the  $m_{\pi^0\pi^0}$  and  $m_{\pi^0 p}$  invariant mass distributions for seven incoming energy bins. Our data is compared with the most precise published results so far [Wol00] and with calculations from the Valencia model [Nac01]. A second curve corresponding to a reaction dominated by phase space has also been represented for reference. As for the total cross sections, our experiment confirms the results of the previous experiment without any significant discrepancy. And once again, the very large amount of data gathered gives a much clearer outline of the behaviour of double  $\pi^0$  photoproduction throughout

the whole studied energy range.

The invariant mass of the two  $\pi^0$  is fairly consistent with a phase space distribution. On the complete energy range, the divergence doesn't exceed 10%, indicating that no strong correlation between the two pions exists in double  $\pi^0$  photoproduction. The behaviour of the  $m_{\pi^0 p}$  invariant mass is different. In the lowest energy bin (310 - 540 MeV), our results are well described by a phase space distribution. At higher energies, a significant enhancement at the mass of the  $\Delta$  resonance appears. Between 540 and 610 MeV, this merely creates a bump in the distribution while for the next energy bins, a very important deviation is visible.

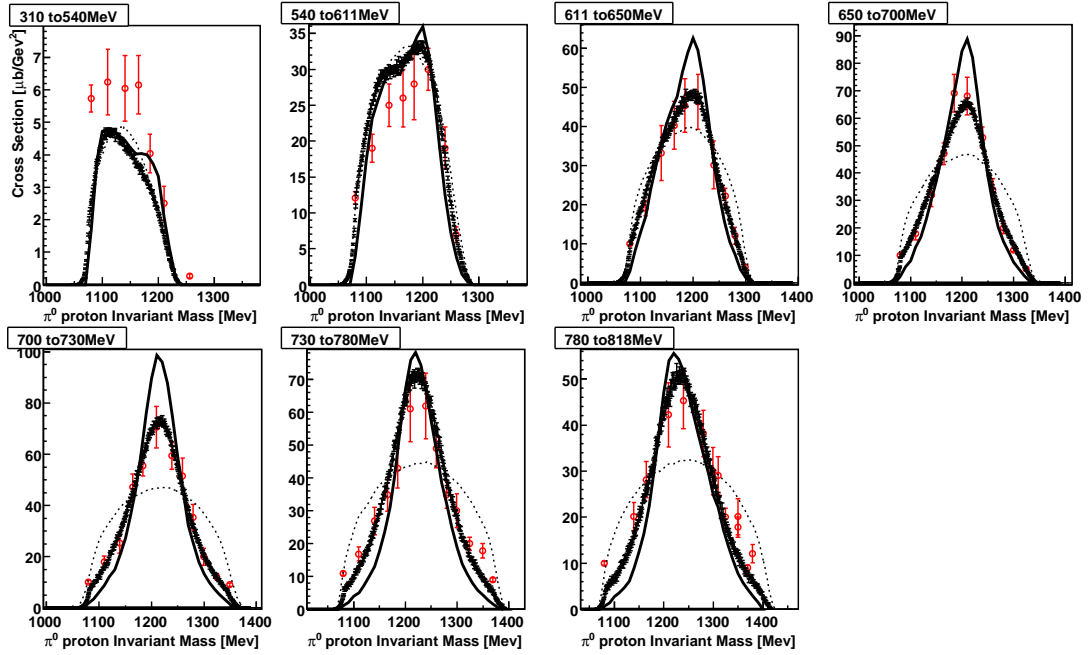


Figure 7.11:  $p \pi^0$  invariant mass in the  $\gamma p \rightarrow p \pi^0 \pi^0$  reaction. Dashed curve: phase space distribution. Solid Curve: Calculations from the Valencia model.

These results nicely confirm the general overview of the mechanisms involved in double  $\pi^0$  photoproduction. The first important feature is that no correlation between the two  $\pi^0$  can be observed. Among all processes contributing to the double  $\pi^0$  channel, the only one that can possibly give a significant contribution to such a correlation is the  $P_{11}(1440) \rightarrow p(\pi^0 \pi^0)_{S\text{-wave}}^{I=0}$  decay. Here, the very small deviation from phase space indicates that this decay only plays a minor role in double  $\pi^0$  photoproduction. This is also visible in the Valencia model calculations in which this  $P_{11}(1440)$  decay only adds a small contribution so that the predictions don't deviate much from a phase space reaction. Altogether, this definitively rules out the dominance of the  $P_{11}(1440) \rightarrow (\pi^0 \pi^0)_{S\text{-wave}}^{I=0} p$  decay as-

sumed by the Saclay model.

In the Valencia and Mainz models, the dominant resonant contribution to double  $\pi^0$  photoproduction comes from the  $D_{13}(1520) \rightarrow \Delta\pi^0 \rightarrow p\pi^0\pi^0$  sequential decay. This assumption is nicely confirmed by our results on the  $m_{\pi^0 p}$  invariant mass distributions. In the the energy range corresponding to the second resonance region, where this decay is supposed to contribute to more than half of the total cross section, a very strong peak at the mass of the  $\Delta$  resonance predicted by the Valencia model and accurately reproduced by our results is a clear evidence of such a dominance. Even at lower energies (540-610 MeV), where only the low energy tail of the  $D_{13}$  can contribute, a clear enhancement at  $m_\Delta$  is predicted by the Valencia model and is confirmed by our data.

### 7.5.2 $\gamma p \rightarrow n\pi^+\pi^0$ invariant masses

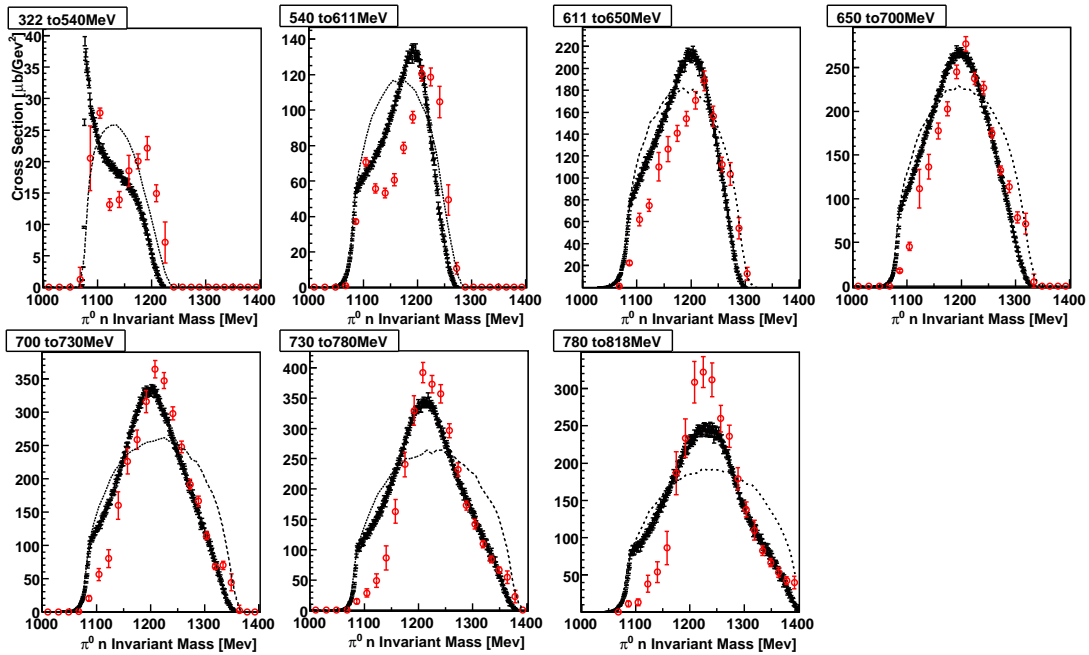


Figure 7.12:  $n\pi^0$  invariant mass in the  $\gamma p \rightarrow n\pi^+\pi^0$  reaction. Dashed curve: phase space distribution.

In fig. 7.12 to 7.14, we show all three possible invariant mass combinations in the  $\gamma p \rightarrow n\pi^+\pi^0$  reaction. Here again, our data is compared with the results of the most precise experiment so far [Lan01] as well as calculations from the Valencia model (for  $m_{\pi^0\pi^+}$ ) and a phase space distribution. As for the double  $\pi^0$  channel, our results show a very nice improvement in the statistics compared to the previous experiment.

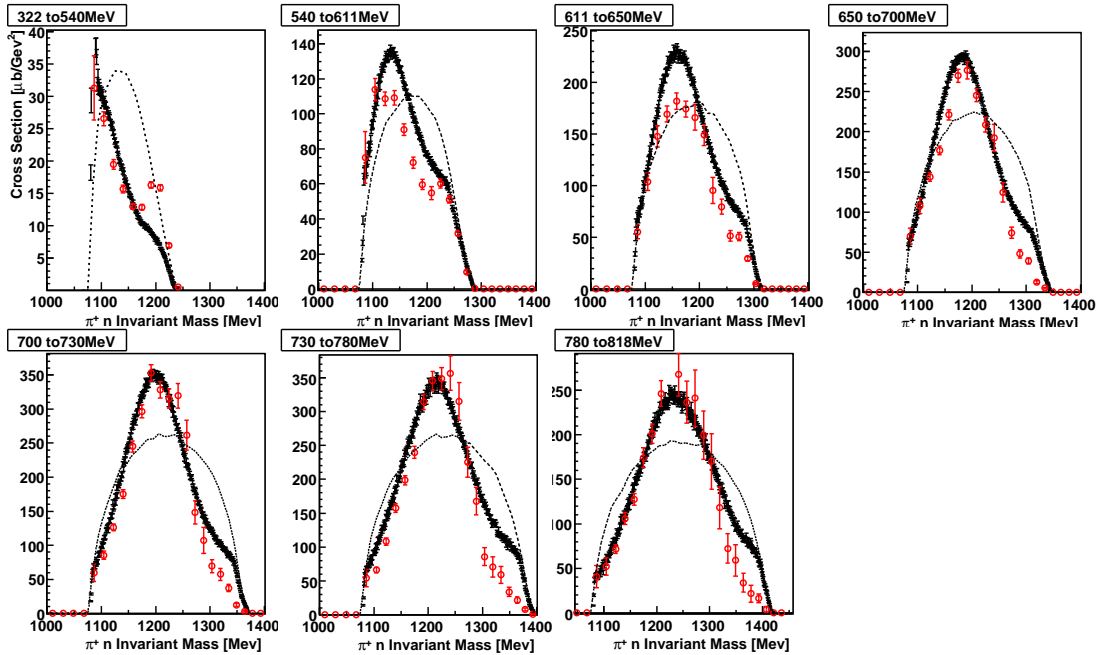


Figure 7.13:  $n \pi^+$  invariant mass in the  $\gamma p \rightarrow n \pi^+ \pi^0$  reaction. Dashed curve: phase space distribution.

Fig. 7.12 and 7.14 represent the  $m_{\pi^0 n}$  and  $m_{\pi^+ n}$  missing masses. In the second resonance region, both invariant masses look very similar, with a strong enhancement at the mass of the  $\Delta$ -resonance. As in the case of the double  $\pi^0$  channel, this is the signature of a dominance of the  $D_{13}(1520) \rightarrow \pi \Delta \rightarrow \pi^+ \pi^0 n$  decay. The distribution look very similar: it can be easily calculated that the contribution of the two channels  $D_{13}(1520) \rightarrow \pi^+ \Delta^0 \rightarrow \pi^+ \pi^0 n$  and  $D_{13}(1520) \rightarrow \pi^0 \Delta^+ \rightarrow \pi^+ \pi^0 n$  to the total cross section is identical. At lower energies, the situation is completely different, this will be examined in detail in the next section. Let's note that a small discrepancy between both data sets appears as a bump for the smallest values of  $m_{\pi^0 n}$  and the highest values of  $m_{\pi^+ n}$ . At lower energies, results from [Lan01] also present such a bump, while at higher energies, the discrepancy gets bigger. The origin of this bump is not yet clear, but it doesn't affect the fact that the  $D_{13}(1520)$  sequential is here the dominant process.

A key feature of the  $\pi^0 \pi^+ n$  is the role of the  $\rho$  meson which had to be introduced to give a reasonable description of the total cross section. Since the  $\rho^+$  decays into two pions, the signature of this meson will be visible in the  $m_{\pi^0 \pi^+}$  invariant mass. Fig. 7.14 shows this invariant mass for seven incoming energy bins together with a phase space distribution and predictions from the Valencia model including the  $D_{13} \rightarrow \rho N$  decay. In order to assess the contribution of the  $D_{13} \rightarrow \rho N$  decay, it is more instructive to compare the  $m_{\pi^0 \pi^0}$  invariant mass from the double  $\pi^0$  (fig. 7.10) channel and  $m_{\pi^0 \pi^+}$  from the  $\pi^0 \pi^+$  channel. This

comparison is a striking evidence of the role of the  $\rho$  meson. As mentioned in chapter 2, the  $\rho^0$  can't decay into two  $\pi^0$ . Therefore, no correlation in the  $m_{\pi^0\pi^0}$  should appear. This is clearly visible in our results which almost don't deviate from a phase space distribution. On the contrary, the  $\rho^+$  always decays into a  $\pi^0$  and a  $\pi^+$ . This leads to a correlation between the two pions. This enhancement is more pronounced in the energy range corresponding to the second resonance region, highlighting the importance of the  $D_{13}(1520) \rightarrow \rho^+n \rightarrow \pi^0\pi^+n$  decay.

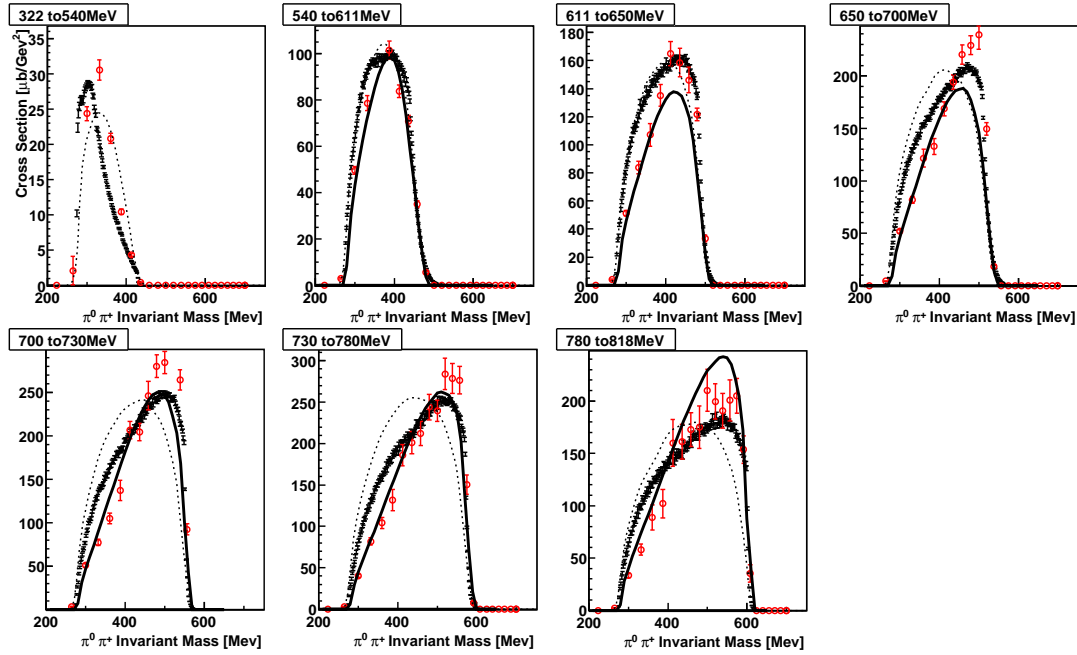


Figure 7.14:  $\pi^0 \pi^+$  invariant mass in the  $\gamma p \rightarrow n\pi^+\pi^0$  reaction. Dashed curve: phase space distribution. Solid Curve: Predictions from the Valencia model.

### 7.5.3 Invariant masses close to threshold

#### Double $\pi^0$ channel

In order to investigate the production mechanisms close to threshold, the invariant masses have been plotted again for smaller energy bins, covering the first 200 MeV above production threshold. For the double  $\pi^0$  channel, our results (fig. 7.16 and 7.15) are compared with the ones from a previous experiment performed at Mainz [Kot03]. Once again, our results show a very good improvement in the statistical quality of the data. (For the 330-360 MeV energy bin however, since two tagger channels were dead (this is visible in fig. 7.2), the total amount of data available is slightly lower than expected.).

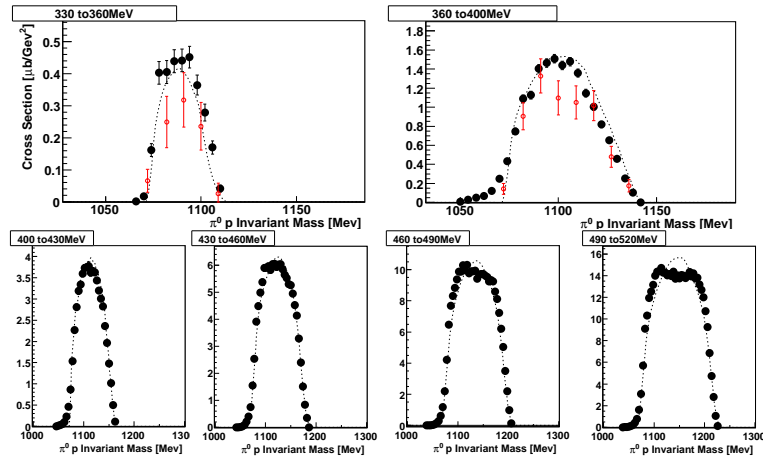


Figure 7.15:  $\pi^0 p$  invariant mass in the  $\gamma p \rightarrow p\pi^0\pi^0$  reaction. Dashed curve: phase space distribution. Red: Data from [Kot03]. Black: This work.

Although a little bit higher in absolute magnitude (especially in the 330-360 MeV bin for  $m_{\pi^0\pi^0}$ ), our results nicely confirm the behaviour of the double  $\pi^0$  channel at low energies outlined in [Kot03]. For the first four energy bins,  $m_{\pi^0 p}$  is consistent with a phase space distribution. It only starts to diverge in the 460-490 MeV energy bin. At this energies, the low tails of resonances from the second resonance region become available and the different resonant processes already mentioned start to contribute. The situation is less simple for the  $m_{\pi^0\pi^0}$  invariant mass. Already in the lowest energy bin (even though this deviation is much less important for the small energies in our results than in [Kot03]), and for all energies, our data slightly deviates from a pure phase space distribution. According to the Valencia model ([Roc02], which deals with the role of the  $\sigma$  meson in double pion photoproduction) this deviation towards high energies is due to an interference between the I=0 and I=2 amplitudes.

### $\pi^0 \pi^+$ channel

The same work has been done for the  $\gamma p \rightarrow n\pi^+\pi^0$  reaction. In this channel the production processes close to threshold are clearly visible in a comparison between  $m_{\pi^0 n}$  and  $m_{\pi^+ n}$  (fig. 7.18 and 7.19). In this energy region, all models predict a dominance of the  $\Delta$ -Kroll-Rudermann and the  $\Delta$ -pion pole terms. These two terms can be written as  $\gamma p \rightarrow \pi\Delta \rightarrow \pi\pi n$  and, a priori, two different decays (represented in fig. 7.17) leading to  $\pi^0 \pi^+ n$  final states are possible.

However, since the  $\pi^0$  doesn't couple to the photon, the  $\gamma p \rightarrow \pi^0\Delta^+ \rightarrow \pi^0\pi^+ n$  is strongly suppressed. As a consequence,  $m_{\pi^0 n}$  should show an enhancement at the mass of the  $\Delta$  resonance which should be absent in the  $m_{\pi^+ n}$  invariant mass distribution. This behaviour is clearly visible in our results:  $m_{\pi^+ n}$  shows a strong deviation from a phase space distribution at the mass of the  $\Delta$  resonance

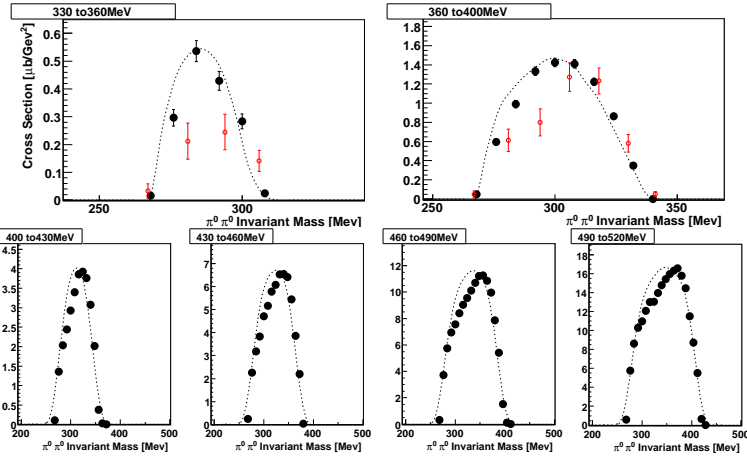


Figure 7.16:  $\pi^0 \pi^0$  invariant mass in the  $\gamma p \rightarrow p \pi^0 \pi^0$  reaction. Dashed curve: phase space distribution. Red: Data from [Kot03]. Black: This work.



Figure 7.17: Feynman diagrams of the two possible  $\Delta$ -Kroll-Rudermann terms leading to  $\pi^0 \pi^+$  final states.  $\gamma p \rightarrow \pi^+ \Delta^0 \rightarrow \pi^0 \pi^+ n$  (left) is allowed while  $\gamma p \rightarrow \pi^0 \Delta^+ \rightarrow \pi^0 \pi^+ n$  (right) is strongly suppressed since the  $\pi^0$  doesn't couple to the photon.

between 430 and 520 MeV. At lower energies, this distortion disappears and our results tend to a phase space distribution. As an opposite, the  $m_{\pi^0 n}$  invariant mass plots don't show such a large correlation. Only a small corresponding bump is visible in this energy range. As mentioned, the two main  $\Delta$ -Born terms can't give rise to such a structure, but other processes with a smaller contribution to the  $\pi^0 \pi^+ n$  channel, such as diagrams 12 and 13 from fig. 2.8 can contribute. Since they don't imply any  $\pi^0 \gamma$  coupling, the decay of the  $\Delta$  into a  $\pi^0$  and a neutron is not suppressed, giving rise to this small bump at the mass of the  $\Delta$ .

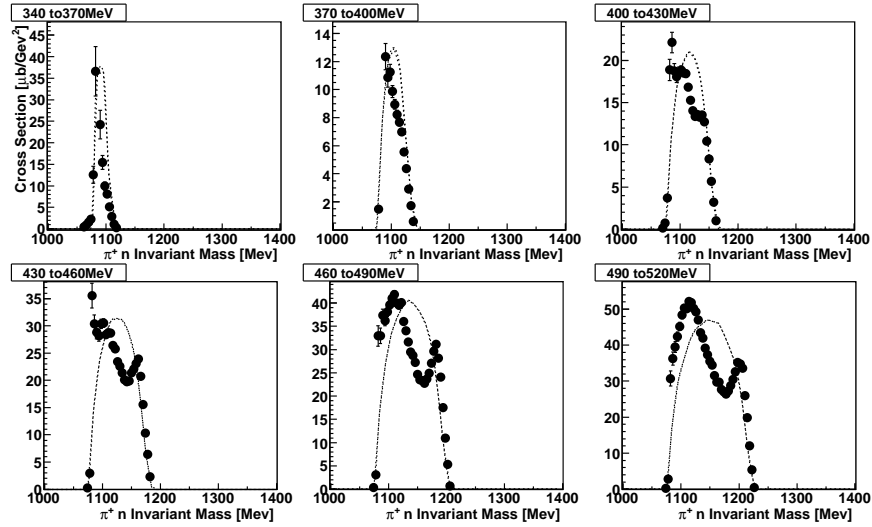


Figure 7.18:  $\pi^+ n$  invariant mass in the  $\gamma p \rightarrow n\pi^+\pi^0$  reaction. Dashed curve: phase space distribution.

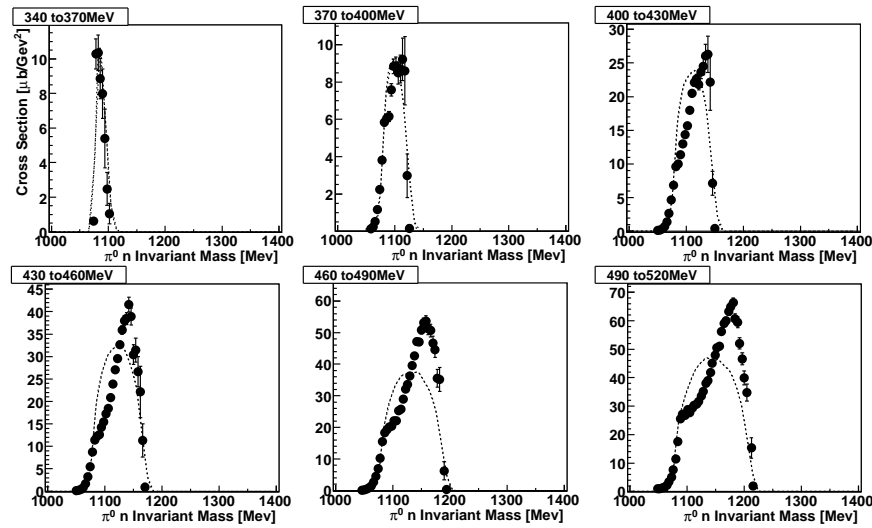


Figure 7.19:  $\pi^0 n$  invariant mass in the  $\gamma p \rightarrow n\pi^+\pi^0$  reaction. Dashed curve: phase space distribution.

# 8 Conclusion and outlook

## Conclusion

The study of double pion photoproduction and especially double  $\pi^0$  photoproduction has always been a main focus of the physics performed at MAMI. This experiment, part of the rich CB/TAPS at MAMI program performed in 2004 and 2005, was the fifth in a series of double  $\pi^0$  experiments to be performed at MAMI B using 880 MeV electrons (after [Bra95], [Här97], [Wol00] and [Kot01]). As a main new feature, this experiment was the first to provide an almost  $4\pi$  coverage of the solid angle using the Crystal Ball and TAPS detectors. This allowed the taking of a huge amount of statistics and made possible a precise study of the double  $\pi^0$  reaction at energies close to threshold. In addition, this work was the first one to investigate double pion reactions with linearly and circularly polarized photons, allowing a first glimpse into the very promising field of polarized observables.

Altogether, the results of this work presented throughout chapter 7 qualitatively confirm the results obtained in previous experiments with a significative improvement in the statistical quality of the data and thus more firmly establishes the underlying physical processes present in double pion photoproduction. In addition, they allowed the measurement of linear and circular asymmetries, one of the first steps on the very promising road of polarization observables. Here is a short summary of the most important results.

- In the second resonance region, invariant mass distributions show that the main contribution to the  $\gamma p \rightarrow p\pi^0\pi^0$  reaction is due to the  $D_{13}(1520) \rightarrow \pi^0\Delta \rightarrow \pi^0\pi^0p$  sequential decay with a very small contribution of the  $P_{11}(1440) \rightarrow p(\pi^0\pi^0)_{S-wave}^{I=0}$  direct decay.
- For the  $\gamma p \rightarrow n\pi^+\pi^0$  reaction, the  $D_{13}(1520)$  decay is also the main resonant process, but a non negligible contribution from  $\rho$  mesons and especially from the  $D_{13}(1520) \rightarrow \rho n \rightarrow \pi^0\pi^+n$  is also observed. Such diagrams play a key role in the models to give correct predictions for  $\pi^0\pi^+n$  cross sections.
- At threshold, the double  $\pi^0$  cross section has been determined very precisely and is in excellent agreement with the prediction from [Ber96]. This is a

striking confirmation of chiral perturbation theory which predicts an unexpectedly large contribution from pion loops to this channel in this energy region.

- Finally, this work has shown the feasibility to precisely measure polarization observables. Circular asymmetries, which is a very precious tool due to its high sensitivity to small changes in the models, have been determined with a great accuracy for all three isospin channels. In the future, such results will be used to efficiently disentangle the contribution of overlapping resonances from the second resonance region to double pion photoproduction. At this time however, the different models used to interpret our results are still in an early stage of development and will need further refinement before such a task is possible.

## Outlook

Double pion photoproduction and especially double  $\pi^0$  photoproduction (due to the small number of background processes allowed) is a wonderful tool for the investigation of nucleon resonances. For a long time in the future, it will continue to attract lots of attention at facilities with ever increasing precision, energy and refinement.

As emphasized throughout this work, polarization observables are very precise tools for a precise study of individual resonances. This field will know a lot of activity in the near future with double polarization experiments (circularly and linearly polarized beam, longitudinally polarized target) planned at MAMI [Are05] and ELSA [Tho05]. In the second resonance region, more constraints will be added to the resonances -especially to the least known  $P_{11}(1440)$ - with the measurement of the E and G double polarization observables. In the third resonance region, which will be available for the first time at MAMI using 1.5 GeV electrons from MAMI C, a similar job will be performed to disentangle and measure the individual properties of the  $F_{15}(1680)$ ,  $D_{13}(1700)$ ,  $D_{33}(1700)$  and  $P_{13}(1720)$  resonances. At higher energies, ELSA will use polarized double  $\pi^0$  to try to discover some of the missing resonances predicted by the models for energies up to 3.5 GeV. In the longer term, even more constraints will be added to the study of nucleon resonances with the development of a recoil polarimeter [Wat05] designed by the University of Glasgow to measure the polarization of the recoil nucleon, thus allowing the measurement of triple polarization observables. This quest for polarized observables is by no means limited to double pion photoproduction on a free proton target. A large number of experiments are planned at MAMI [MAMwww] and ELSA [ELSwww] which include the measurement of polarization in single pion,  $\eta$ ,  $\eta'$ ,  $\omega$  and  $\eta\pi^0$  on both polarized free proton and deuteron (to study photoproduction on the neutron in quasifree kinematics or coherent production) targets. Let's finally mention that in addition to the study

of nucleon resonances, a big part of this program is dedicated to the measurement of the GDH sum rule (see e.g. [Ped05]).

All these oncoming experiments, together with meson photoproduction on heavy nuclei used to study in-medium modifications of mesons and resonances and with more specific subjects such as the measurement of the  $\Delta$  magnetic moment of the  $S_{11}(1535)$  resonance [Kot05] and the quest for bound states such as  $\eta$ -mesic nuclei [Bec03] will offer a lot of opportunities for the study of matter in the future and will hopefully lead to many spectacular results such as the possible new resonance at 1680 MeV discovered at ELSA with  $\eta$  photoproduction off a deuteron target [Jaé07] and [Jaé08].



## 9 Acknowledgments

First of all, I would like to thank Prof. Bernd Krusche for the constant advice, help and answer to every question I had during these four years and for having given me the opportunity to join the fruitful A2 collaboration. All my gratitude goes also to Martin Kotulla for his everyday help during his postdoc time at Basel. I'm especially grateful for the constant and careful supervision of the data taking and for the regular organization of analysis meetings. Without them, the results presented here would never have been so good.

Next, I wish to thank all the members of the A2 collaboration for the very efficient working atmosphere and the very relaxed after-work atmosphere. I especially want to thank all PhD students for their long and hard work during the shifts and for the tedious calibration of every single part of the detector. Many thanks to Ralf Gregor, Stefan Lugert, Marc Unverzagt, Sven Schumann, Alexander Nikolaiev, Claire Tarbert, Evie Downie, Richard Codling, Jason Brudvik and Benedicte Boillat. I didn't forget Dirk Krambrich: thanks for the big help with the electronics and for the very useful discussions on the analysis of double pion data. For the big help during the shifts, thanks also to Dave Hornidge and his summer students squad, the russian team present in Mainz and Andreas Thomas and all the target people. For all the work he performs in the collaboration and the patience he had to answer every single question on AcqRoot I had, thanks to John R. M. Annand.

In Basel, Benedicte was my twin PhD student: thanks for accompanying me along this difficult road and good luck for the future!

Thanks also to the short time postdocs who shared a bit of their experience with me: Cedric, Thierry and Igal.

Thanks for the good atmosphere to all former and present members of the institute: Fred, Cedric, Florian, Christophe, Thierry, Giuseppe. – Benedicte, Igal, Yasser, Francis, Dominik, Therese, Roman.

Thanks to Peter Schmid, Beat Glatz and Roman Trojer for the big help with the servers and the computers and to Astrid Kalt and Barbara Kammerman for all the administrative work.

Finally, I wish to thank my parents and family for their everlasting support. All my non-physicist friends who took some interest in this work - explaining what

you're doing to Muggles is always a very good exercise. And of course Cindy for her patience and understanding - all my love.

Last but not least, I thank the Swiss National Science Foundation (SNF) and the Deutsche Forschungsgemeinschaft (DFG) for the money that made this work possible.

# A Specific problems in the analysis

## A.1 Tagger 4x4 structure

When computing total cross sections (fig. 7.1 and 7.3), each point is determined using the data from a single tagger channel. If no further rebinning is applied, it turns out that an unwanted 4 by 4 structure appears and spoils our results. This is illustrated in fig. A.1 for the double  $\pi^0$  channel, but it also appears in the  $\pi^0 \pi^+$  cross section or in any other reaction studied with these data.

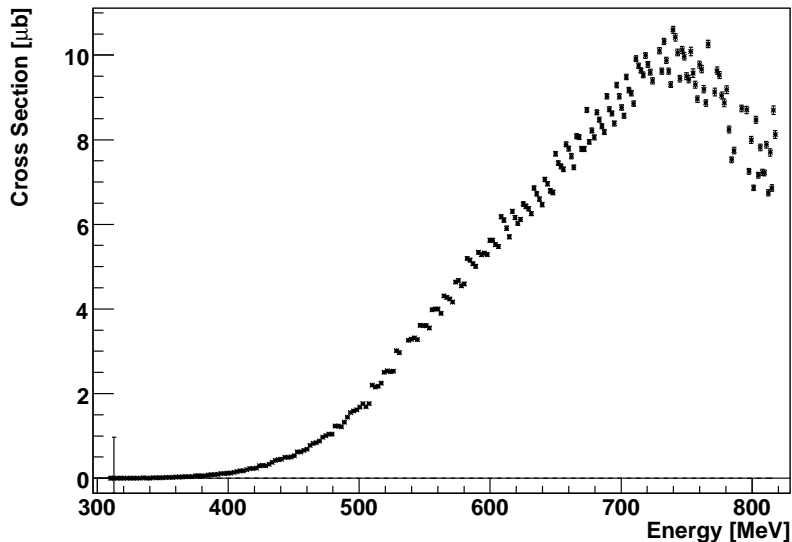


Figure A.1: *Cross section for the  $\gamma p \rightarrow p\pi^0\pi^0$  reaction without any 4x4 tagger staggering correction. A structure is clearly visible for energies higher than 500 MeV, but is present over the complete energy range.*

This structure is the consequence of some inconsistency in the determination of the tagger hits. According to S. Schuman [SchPr], it might be due to a problem in the tagger TDCs, but up to now, its exact origin is not yet fully understood. In fig. A.2, this structure becomes even more evident when dividing the tagger hits by the tagger scalars (solid line).

Since the problem appears at a 'low' level (the tagger hits are simply readout without any further fancy software operation), it is highly probable that it is due to some hardware flaw and therefore that a proper correction by software is impossible. Nevertheless, it is always preferable to present smooth results. In that sense, the following procedure has been applied to hide this structure. For each group of 4 points in the tagger\_hits/tagger\_scalars ratio, the average value has been calculated. Then, for each of these four points, the deviation (individual\_value/average\_value) has also been calculated. These deviations are represented by the black dots on fig. A.2. As the deviation is very stable over the complete energy range (the black dots are distinctly grouped in 4 lines), it is possible to calculate 4 overall correction factors (red dots) that are applied to our cross sections which, that way, get a much smoother look.

But as stated, this method is not a proper correction, only a mere cosmetic trick and thus includes an additional systematic error in the determination of the cross sections. As the values of the four correction factors are 0.964, 0.985, 1.009 and 1.036, this error is assumed to be 4%.

Let's finally note that this 4 by 4 structure is not visible for all beamtimes performed during the the 2004/2005 round of experiments. It is clearly visible for all MDM and for the June single  $\pi^0$  beamtimes. For the November and December  $\eta$  runs and all solid target runs, it is much less evident but still affects the cross sections in some way [SchPr], [TarPr].

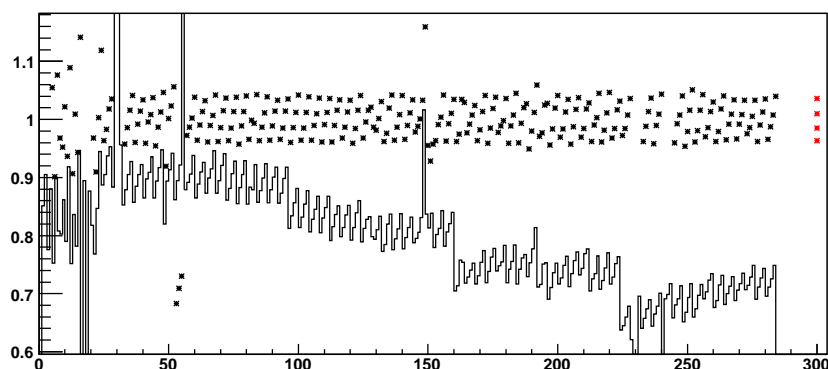


Figure A.2: *Correction of the  $4 \times 4$  tagger structure. The tagger\_hits/tagger\_scalars ratio (solid line) is used to calculate individual correction factors (black dots) which are averaged to obtain four overall correction factors (red dots).*

## A.2 Ice deposition on the target window

Another unexpected problem that had a significant influence on the precision of our results was the constant growth of ice on the target exit window. This ice deposition wouldn't have been a problem if it had been removed properly. Unfortunately, it went unnoticed for the complete July beamtime and half of the September beamtime. Moreover, empty target measurements can be used to handle the effects of this ice, but no such measurement has been performed during the whole July beamtime.

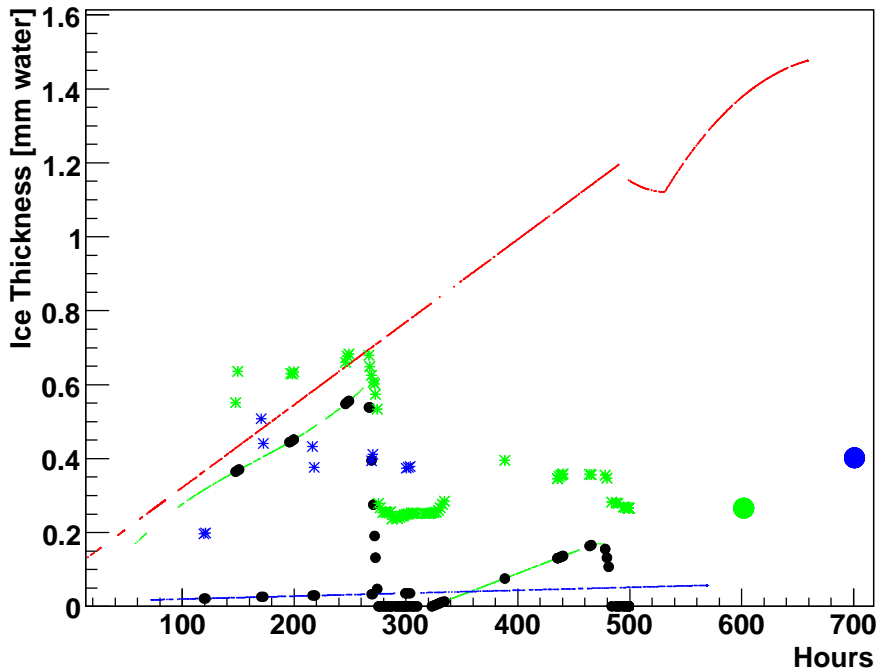


Figure A.3: *Ice deposition on the target exit window (small dots, red: July, green: September, blue: January, big black: empty targets runs) together with the corresponding double  $\pi^0$  cross sections. See text for more explanation.*

In order to account for this ice as well as can be, the following procedure, illustrated in fig A.3 is applied.

- The ice thickness has been determined by V. Kashevarov and A. Thomas with a method based on the comparison between the single  $\pi^0$  photoproduction yields on ice and water targets [Tho05b]. The ice thickness is given in mm of water equivalent. Let's note that at its maximum (end of July beamtime), it reached 1.5 mm, a very high value that can by no means be neglected. The ice thickness is represented by the small dots on fig A.3 .

The points corresponding to empty target measurements have been highlighted in black.

Once this problem was noticed (half of September beamtime), a long time warm empty target measurement has been performed. Following this, the ice growing was permanently kept under control with additional isolation devices and wasn't allowed to reach more than 0.1 mm of water equivalent.

- In a second step, the double  $\pi^0$  cross section was determined for each empty target file. The corresponding values are represented by the stars on fig A.3. A relatively good correlation between the ice thickness and the cross section values can be observed, especially for the September beamtime.
- This correlation is used to account for the ice. For the September beamtime, when no ice is present on the target window, the empty target contributes for 0.26  $\mu\text{b}$  to the total cross section (big green dot). Each additional 0.1 mm of water equivalent is responsible for 0.08 additional  $\mu\text{b}$ .
- The ice thickness is then integrated over the total data taking time. The average value is added to the ice-free empty target to give the total (warm target + ice) empty target contribution.
- For the July beamtime, the same procedure is applied, but since no empty target measurement is available, the September values have been used. (without ice: 0.26  $\mu\text{b}$ . 0.08  $\mu\text{b}$  for each 0.1 mm of water equivalent). Of course, the assumption that both September and July beamtimes present the same linear behaviour is only a rough approximation. At the end of the July beamtime, it is likely that the very thick ice layer is responsible for much more background than expected.
- For the January beamtime, the situation is made simpler by the much slower growth of ice. All empty target files are simply added and the corresponding double  $\pi^0$  cross section computed (big blue dot). Let's note that even if the ice plays a much less important role, the empty target contribution to the total cross section is higher due to the additional isolation devices put around the target.

Once the total contribution of the empty target is known, it is removed from the total cross section. As an illustration, fig. A.4 shows the double  $\pi^0$  cross section for the July beamtime before and after the ice is removed. The effect is clearly visible and is maximal for energies higher than 700 MeV in the second resonance region. For the September and January beamtimes, the change is much less evident due to the smaller amount of ice involved.

This ice problem is a source of further imprecision in our results. The additional systematic error is estimated to be 5%.

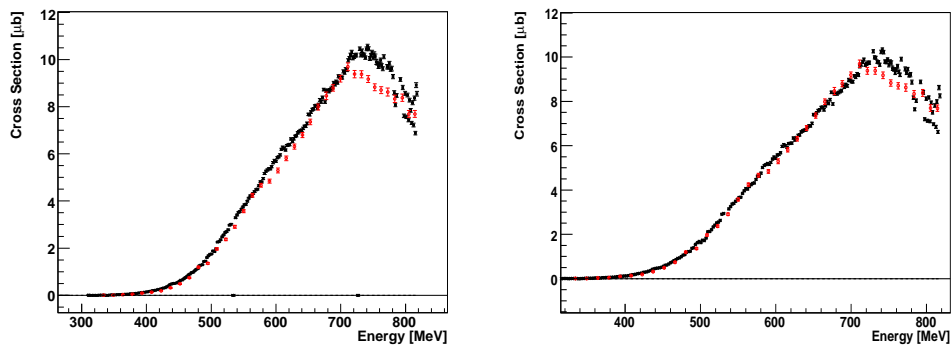


Figure A.4: *Double  $\pi^0$  cross section before (left) and after (right) subtraction of the empty target for the July beamtime.*



## B Tables

For all the histograms presented in this work, ascii files with the values of the points are (will be) available at <http://jazz.physik.unibas.ch/~zehr/xxx.dat>

Plot	Data File
$\gamma p \rightarrow p\pi^0\pi^0$ total cross section	CSPi0Pi0.dat
$\gamma p \rightarrow n\pi^+\pi^0$ total cross section	CSPi0PiP.dat
$\gamma p \rightarrow n\pi^+\pi^0$ circular asymmetries	AsymCirc.dat
$\gamma p \rightarrow p\pi^0\pi^0$ and $\gamma p \rightarrow n\pi^+\pi^0$ linear asymmetries	AsymLin.dat
$\gamma p \rightarrow p\pi^0\pi^0$ invariant mass distributions	MIPi0Pi0.dat MIPi0p.dat
$\gamma p \rightarrow n\pi^+\pi^0$ invariant mass distributions	MIPi0PiP.dat MIPi0n.dat MIPiPn.dat



# Bibliography

- [XxxPr] indicate a private communication from one of the A2 collaboration members (see the full A2 members list at the end of this bibliography).
- [Ahr05] J. Ahrens et al.: *Intermediate resonance excitation in the  $\gamma p \rightarrow p\pi^0\pi^0$  reaction*. Phys. Lett. B **624** 173 (2007)
- [Aja07] J. Ajaka et al.: *Double  $\pi^0$  photoproduction on the neutron at GRAAL*. Phys. Lett. B **651** 108 (2007)
- [Ann05] J. R. M. Annand: *Data Analysis within an AcquRoot Framework*. University of Glasgow (2005)
- [Ant91] I. Anthony et al.: *Design of a tagged photon spectrometer for use with the Mainz 840 MeV microtron*. Nucl. Inst. and Meth. A **301** 230 (1991)
- [Are05] H.-J. Arends, A. Braghieri, M. Kotulla and P. Pedroni: *Helicity Dependence of Meson Photoproduction on the Proton*. Proposal for an experiment MAMI/A2/7-05 (2005)
- [Ass05] Y. Assafiri et al.: *Double  $\pi^0$  Photoproduction on the Proton at GRAAL*. Phys. Rev. Lett. A **90** 222001 (2003)
- [Aud91] G. Audit et al.: *DAPHNE: a large-acceptance tracking detector for the study of photoreactions at intermediate energies*. Nucl. Inst. and Meth. A **301** 473 (1991)
- [Aul97] K. Aulenbacher, C. Nachtigall et al.: *The MAMI source of polarized electrons*. Nucl. Inst. and Meth. A **391** 498 (1997)
- [Bec03] R. Beck, B. Krusche and M. Pfeiffer: *Coherent Photoproduction of  $\eta$ -mesons from light nuclei - search for  $\eta$ -mesic nuclei*. Proposal for an experiment MAMI/A2/7-03 (2003)
- [Ber96] V. Bernard, N. Kaiser and U.-G. Meißner: *Double neutral pion photoproduction at threshold*. Phys. Lett. B **382** 19 (1996)

- [Bra95] A. Braghieri, L. Y. Murphy et al.: *Total cross section measurement for the three double pion photoproduction channels on the proton*. Phys. Lett. B **363** 46 (1995)
- [Blo07] F. Bloch et al.: *Double pion photoproduction off  $^{40}\text{Ca}$* . Eur. Phys. J. A **32** 219 (2007)
- [Boi08] B. Boillat: *Determination of the Magnetic Dipole Moment of the  $\Delta^+(1232)$  Resonance*. PhD Thesis, Universität Basel (2008)
- [Bru07] J. Brudvik: *Measurement of the branching ratio for eta-meson decay into a neutral pion and two photons*. PhD Thesis, UCLA (2007)
- [Cah89] R. N. Cahn and G. Goldhaber: *The Experimental Foundations of Particle Physics*. Cambridge University Press (1989)
- [Cap00] S. Capstick and W. Roberts: *Quark Models of Baryon Masses and Decays*. Prog. Part. Nucl. Phys. **45** 241 (2000)
- [Cod08] R. Codling: PhD Thesis, University of Glasgow (2008)
- [Dal53] R. H. Dalitz: *On the analysis of  $\tau$ -meson data and the nature of the  $\tau$ -meson*. Phil. Mag. **44** 1068 (1953)
- [Dow07] E. Downie: *Radiative  $\pi^0$  photoproduction in the region of the  $\Delta(1232)$  resonance*. PhD Thesis, University of Glasgow (2007)
- [Dre01] D. Drechsel and M. Vanderhaegen: *Magnetic dipole moment of the  $\Delta^+(1232)$  from the  $\gamma p \rightarrow \gamma \pi^0 p$  reaction*. Phys. Rev. C **64** 065202 (2001)
- [Dre03] P. Drexler et al.: *The new readout electronics for the BaF<sub>2</sub> calorimeter TAPS*. IEEE Trans. on Nucl. Sci. **50** 969 (2003)
- [Dre04] P. Drexler: *Entwicklung und Aufbau der neuen TAPS-Elektronik*. PhD Thesis, Universität Gießen (2004)
- [ELSWww] *Crystal Barrel proposals to the PAC*. <http://www.cb.uni-bonn.de>  $\rightarrow$  intern  $\rightarrow$  proposals (restricted access)
- [Fix05] A. Fix and H. Ahrenhövel: *Double-pion photoproduction on nucleon and deuteron*. Eur. Phys. J. A **25** 115 (2005)
- [FixWWW] <http://www.kph.uni-mainz.de/MAID/twopion/>
- [Gom94] J. A. Gómez Tejedor and E. Oset: *A model for the  $\gamma p \rightarrow p \pi^+ \pi^-$  reaction*. Nucl. Phys. A **571** 667 (1994)

- [Gom96] J. A. Gómez Tejedor and E. Oset: *Double pion photoproduction on the nucleon: study of the isospin channels*. Nucl. Phys. A **600** 413 (1996)
- [Gre07] R. Gregor: PhD Thesis, Universität Gießen (2007)
- [Här97] F. Härter et al.: *Two neutral pion photoproduction off the proton between threshold and 800 MeV*. Phys. Lett. B **401** 229 (1997)
- [Hej98] V. Hejny: *Photoproduktion von  $\eta$ -Mesonen an Helium 4*. PhD Thesis, Universität Gießen (1998)
- [Hir03] M. Hirata, N. Takagiri and T. Takaki:  *$\pi NN$  coupling and two-pion photoproduction on the nucleon* Phys. Rev. C **67** 034601 (2003)
- [Hor06] M. Horras: *The walkcorrection in a nuclear physical experiment*. Semester project, Universität Basel (2006)
- [Jaé07] I. Jaeglé:  *$\pi^0 \pi^0$ ,  $\eta$  and  $\eta'$  photoproduction off the deuteron or The search for missing resonances*. PhD Thesis, Basel Universität (2007)
- [Jaé08] I. Jaeglé, T. Mertens et al.: *Quasi free photoproduction of  $\eta$ -mesons off the deuteron*. To be published in Phys. Rev. Lett. (2008)
- [Jan00] S. Janssen et al.: *The New Charged-Particle Veto Detector for the Photon Spectrometer TAPS*. IEEE Trans. on Nucl. Sci. **47** 798 (2000)
- [Jan05] A. Jankowiak: *The Mainz Mikroton MAMI - past and future*. Technical Report 1, KPH Universität Mainz (2005)
- [Kon68] A. Konratyuk and L. A. Ponomarev: *Possibility of measuring the magnetic moment of the isobar  $\Delta^{++}(1236)$  in radiative  $\pi^+ p$  scattering*. Sov. J. Nucl. Phys. **7** 82 (1968)
- [Kot01] M. Kotulla: *Experiment zur Bestimmung des magnetischen Moment der  $\Delta^+(1232)$  Resonanz*. PhD Thesis, Universität Gießen (2001)
- [Kot02] M. Kotulla et al.: *The reaction  $\gamma p \rightarrow \pi^0 \gamma p$  and the magnetic moment of the  $\Delta^+(1232)$  resonance*. Phys. Rev. Lett. **89** 272001 (2002)
- [Kot03] M. Kotulla et al.: *Double  $\pi^0$  photoproduction off the proton at threshold*. Phys. Lett. B **578** 63 (2003)
- [Kot05] M. Kotulla et al.: *The Reaction  $\gamma p \rightarrow \eta \gamma p$  and the Magnetic Moment of the  $S_{11}^+(1535)$  Resonance*. Proposal for an experiment MAMI/A2/4-05 (2005)

- [Kra07] D. Krambrich: *Aufbau des Crystal Ball-Detektorsystems und Untersuchung des Helizitätsasymmetrie in  $\gamma p \rightarrow n\pi^+\pi^0$* . PhD thesis, Universität Mainz (2007)
- [Kra08] D. Krambrich, F. Zehr et al.: *Beam-Helicity Asymmetries in Double Pion Photoproduction off the Proton*. To be published in Phys. Rev. Lett. (2008)
- [Kru95] B. Krusche: *Photoproduction of  $\pi^0$  and  $\eta$  mesons from nucleons and nuclei in the second resonance region*. Habilitation Thesis, Gießen Universität (1995)
- [Kru03] B. Krusche and S. Schadmand: *Study of Non-Strange Baryon Resonances with Meson Photoproduction*. Prog. Part. Nucl. Phys. **51** 399 (2003)
- [Kru05] B. Krusche: *Photoproduction of mesons from nuclei – in medium-properties of hadrons*. Prog. Part. Nucl. Phys. **55** 46 (2005)
- [Lan01] W. Langgärtner et al.: *Direct Observation of a  $\rho$  Decay of the  $D_{13}(1520)$  Baryon Resonance*. Phys. Rev. Lett. **87** 052001 (2001)
- [Liv05] K. Livingston: *The Stonehenge technique: a new method of crystal alignment for coherent bremsstrahlung experiments*. Proceedings of the SPIE **5974** 170 (2005)
- [Loh94] D. Lohmann, J. Peise et al.: *Linearly polarized photons at MAMI (Mainz)*. Nucl. Inst. and Meth. A **343** 494 (1994)
- [Lug07] S. Lugert: PhD Thesis, Universität Gießen (2007)
- [Lük71] D. Lücke and P. Söding: *Symposium on Meson-, Photo-, and Electroproduction at Low and Intermediate Energies, Bonn: September 21-26, 1970*. Springer Tracts in Modern Physics **59** 39 (1971)
- [MAMwww] *A2 proposals from the Year 2005*. <http://wwwa2.kph.uni-mainz.de/A2> → publications → proposals (restricted access)
- [Mur96] L. Y. Murphy and J-M. Laget: *Reaction mechanisms in two-pion photoproduction on the proton: I- Meson exchange picture*. DAPHNIA/SPhN 96-10 (1996)
- [Nac01] J. C. Nacher et al.: *The role of  $\Delta(1700)$  excitation and  $\rho$  production in double pion photoproduction*. Nucl. Phys. A **696** 295 (2001)
- [Nac02] J. C. Nacher and E. Oset: *Study of polarization observables in double pion photoproduction on the proton* Nucl. Phys. A **697** 372 (2002)

- [Nat03] F. A. Natter et al.: *Monte Carlo simulation and analytical calculation of coherent bremsstrahlung and its polarisation* Nucl. Inst. and Meth. B **211** 465 (2003)
- [Nef95] B. M. K. Nefkens: *The Crystal Ball Technical Report 1*. UCLA (1995)
- [Nef05] B. M. K. Nefkens for the Crystal Ball Collaboration: *Highlights of Crystal Ball Physics*. Int. J. Mod Phys. A **20** 1575 (2005)
- [Nik07] A. Nikolaiev: *The tagging efficiency measurements*. Universität Mainz (2007)
- [Nik08] A. Nikolaiev: PhD Thesis, Universität Mainz (2008)
- [Nov91] R. Novotny: *The BaF<sub>2</sub> Photon Spectrometer TAPS*. IEEE Trans. Nucl. Sci. **38** 379 (1991)
- [Och97] K. Ochi, M. Hirata and T. Takaki: *Photoabsorption on a Nucleon in the D<sub>13</sub>(1520) Resonance Energy Region*. Phys. Rev. C **56** 1472 (1997)
- [Ols59] H. Olsen and L. C. Maximon: *Photon and Electron Polarization in High-Energy Bremsstrahlung and Pair Production with Screening*. Phys. Rev. **114** 887 (1959)
- [Ped05] P. Pedroni, W. Briscoe and A. Thomas: *Helicity dependence of single and double pion photoproduction processes and the GDH integral on the neutron*. Proposal for an experiment MAMI/A2/9-05 (2005)
- [PDG06] Particle Data Group, *Particle Physics Booklet*. Available at <http://pdg.lbl.gov> (2006)
- [Ram98] F. Rambo et al.: *Enhancement of the linear polarization of coherent bremsstrahlung by collimation of the photon beam*. Phys. Rev. C **58** 489 (1998)
- [Rei96] A. Reiter et al.: *A microscope for the Glasgow photon tagging spectrometer in Mainz*. Eur. Phys. J. A **30** 461 (1996)
- [Röb91] M. E. Röbig: *Eichung des TAPS-Detektorsystems mit Höhenstrahlung*. Master Thesis, Universität Gießen (1991)
- [Rob05] W. Roberts and T. Oed: *Polarization observables for two-pion production off the nucleon*. Phys. Rev. C **71** 055201 (2005)
- [Roc02] L. Roca, E. Oset and M. J. Vicente Vacas: *The  $\sigma$  meson in a nuclear medium through two pion photoproduction*. Phys. Lett. B **541** 77 (2002)

- [Roc05] L. Roca: *Helicity asymmetries in double pion photoproduction on the proton*. Nucl. Phys. A **748** 192 (2005)
- [ROOwww] <http://root.cern.ch>
- [Sar08] A. V. Sarantsev, M. Fuchs, M. Kotulla, U. Thoma et al.: *New results on the Roper resonance and the  $P_{11}$  partial wave*. Phys. Lett. B **659** 94 (2008)
- [Sch01] A. Schmidt: *Photoproduktion neutraler Pionen am Proton mit linear polarisierten Photonen im Bereich der Schwelle*. PhD Thesis, Universität Mainz (2001)
- [Sch03] S. Scherer: *Introduction to Chiral Perturbation Theory*. Adv. Nucl. Phys. **27** 277 (2003)
- [Sch07] S. Schumann: PhD Thesis, Universität Mainz (2008)
- [Str05] S. Strauch et al.: *Beam-Helicity Asymmetries in Double-Charged Pion Photoproduction on the Proton*. Phys. Rev. Lett. **95** 162003 (2005)
- [Tagwww] <http://wwwa2.kph.uni-mainz.de/A2/> → Experiments → Standard Instruments → Tagger Calibration
- [TAPwww] <http://pcweb.physik.uni-giessen.de/taps/publications/publi.html>
- [Tar07] C. Tarbert: PhD Thesis, University of Edinburgh (2007)
- [Tar08] C. Tarbert et al.: *Incoherent pion photoproduction on  $^{12}\text{C}$* . To be published in Phys. Rev. Lett. (2008)
- [Tho05] U. Thoma, H. van Pee and A. Sarantsev: *Measurement of Double polarization Observables in  $2\pi^0$  Photoproduction with the Crystal Barrel Detector at ELSA*. Proposal for an experiment ELSA/6-05 (2005)
- [Tho05b] A. Thomas: *Status of the Crystal Ball Targets for the 2<sup>nd</sup> round at MAMI C*. Talk at the 7th A2 meeting in Los Angeles (2005)
- [Tho08] U. Thoma, M. Fuchs et al.:  *$N^*$  and  $\Delta^*$  decays into  $N\pi^0\pi^0$* . Phys. Lett. B **659** 87 (2008)
- [Unv08] M. Unverzagt: PhD Thesis, Universität Mainz (2008)
- [Wat05] D. P. Watts et al.: *Recoil nucleon polarimetry observables in meson photoproduction at MAMI*. Proposal for an experiment MAMI/A2/5-05 (2005)
- [Wil91] W. S. C. Williams: *Nuclear and Particle Physics*. Oxford Science Publications (1991)
- [Wol00] M. Wolf et al.: *Photoproduction of neutral pion pairs from the proton*. Eur. Phys. J. A **9** 5 (2000)

During the 2004/2005 round of experiment, the following people were members of the A2 collaboration:

**B.Boillat, M. Kotulla<sup>1</sup>, B. Krusche, F. Zehr**

*Department Physik, Universität Basel, Switzerland*

<sup>1</sup> now at Gießen

**R. Gregor, S. Lugert, V. Metag**

*II. Physikalisches Institut, University of Gießen, Germany*

**P. Aguar, J. Ahrens, H.-J. Arends, R. Beck<sup>2</sup>, E.Heid, O. Jahn, M. Lang<sup>2</sup>, M. Martinez, A. Nikolaiev<sup>2</sup>, M. Rost, S. Schumann<sup>2</sup>, A. Thomas, M. Unverzagt, Th. Walcher**

*Institut für Kernphysik, University of Mainz, Germany*

<sup>2</sup> now at Helmholtz Institut für Strahlen- und Kernphysik, University Bonn, Germany

**J. R. M. Annand, R. Codling, E. Downie, D. I. Glazier,<sup>3</sup>  
K. Livingston, I. J. D. MacGregor, J. C. McGeorge, R. O. Owens, G. Rosner**

*Department of Physics and Astronomy, University of Glasgow, UK*

<sup>3</sup> now at Edinburgh

**V. Bekrenev**

*Petersburg Nuclear Physics Institute, Gatchina, Russia*

**A. Braghieri, P. Pedroni, T. Rostomyan**

*INFN Sezione di Pavia, Italy*

**D. Branford, K. Föhl, C. M. Tarbert, D. P. Watts**

*School of Physics, University of Edinburgh, UK*

**W. J. Briscoe**

*Center for Nuclear Studies, The George Washington University, Washington, DC, USA*

**J. Brudvik, B. M. K. Nefkens, S. N. Prakhov, J. W. Price,  
A. Starostin**

*University of California at Los Angeles, CA, USA*

**S. Cherepnaya, V. Kashevarov**

*Lebedev Physical Institute, Moscow, Russia*

**P. Grabmayr**

*Physikalisches Institut Universität Tübingen, Germany*

**D. Hornidge**

*Mount Allison University, Sackville, NB, Canada*

**A. Knezevic, M.Korolija, D. Mekterovic, I. Supek**

*Rudjer Boskovic Institute, Zagreb, Croatia*

**R. Kondratiev, V. Lisin, A. Polonski**

*Institute for Nuclear Research, Moscow, Russia*

**D. M. Manley**

*Kent State University, OH, USA*

**S. Schadmand**

*Institut für Kernphysik, Forschungszentrum Jülich, Germany*

**D. Sober**

*The Catholic University of America, Washington, DC, USA*